9 789462 956353

ELECTRON DENSITY STUDIES ON MAGNETIC SYSTEMS

MAURITS BOEIJE

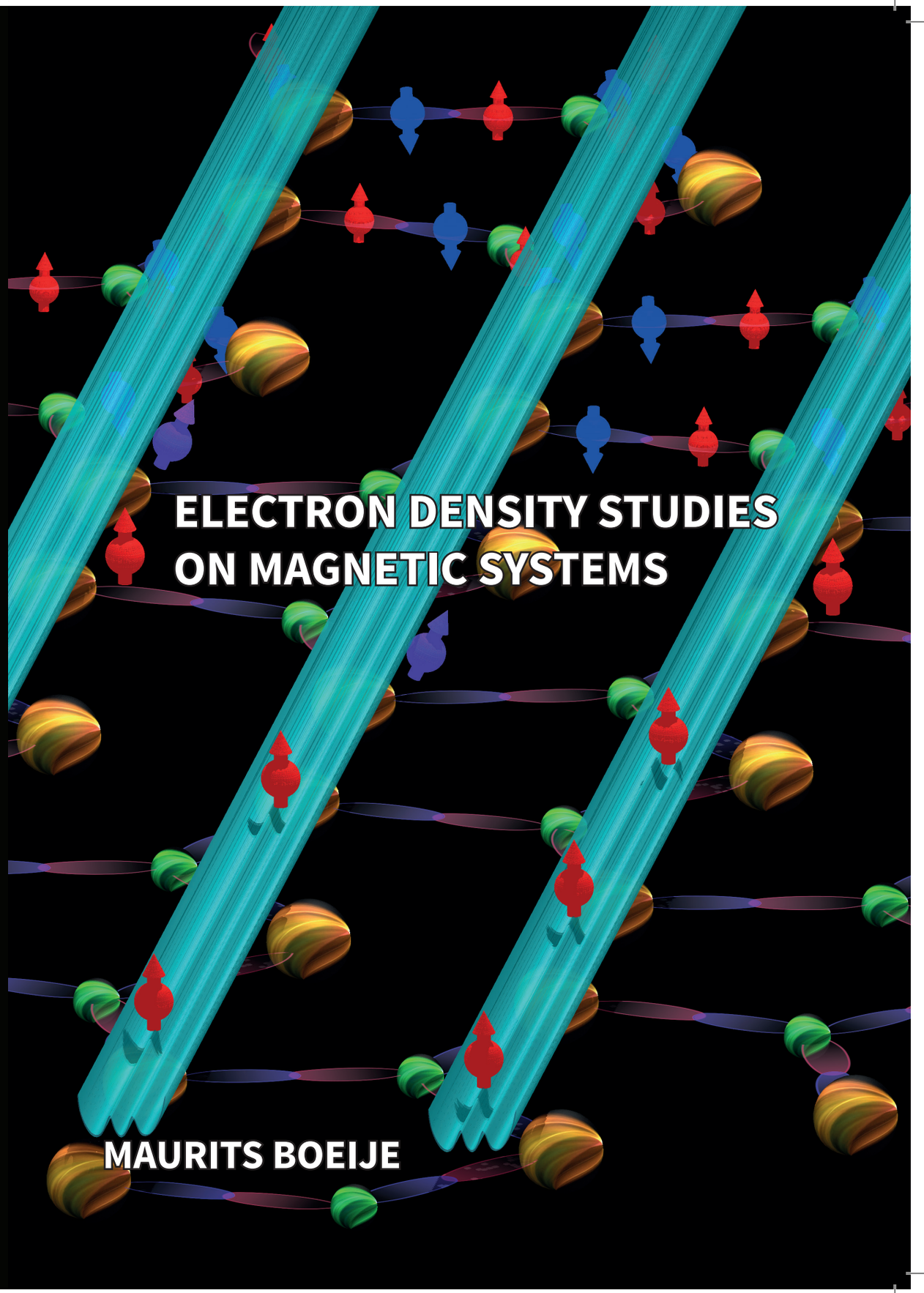

ELECTRON DENSITY STUDIES ON MAGNETIC SYSTEMS

MAURITS BOEIJE

Electron density studies on magnetic systems

Electron density studies on magnetic systems

Proefschrift

ter verkrijging van de graad van doctor
aan de Technische Universiteit Delft,
op gezag van de Rector Magnificus prof. ir. K.C.A.M. Luyben,
voorzitter van het College voor Promoties,
in het openbaar te verdedigen op maandag 3 juli 2017 om 12:30 uur

door

Maurits Boeije

Master of Science in Chemistry,
Radboud Universiteit, Nijmegen
geboren te Oostburg, Nederland.

Dit proefschrift is goedgekeurd door de

promotor: prof. dr. E.H. Brück
copromotor: dr. ir. N.H. van Dijk

Samenstelling promotiecommissie:

Rector Magnificus,	voorzitter
Prof. dr. E.H. Brück,	Technische Universiteit Delft
Dr. ir. N.H. van Dijk,	Technische Universiteit Delft
Onafhankelijke leden:	
Prof. dr. L.F. Cohen,	Imperial College London
Dr. ir. G.A. de Wijs,	Radboud Universiteit Nijmegen
Prof. dr. P. Dorenbos,	Technische Universiteit Delft
Prof. dr. F.M. Mulder,	Technische Universiteit Delft
Prof. dr. ir. T.H. van der Meer,	Universiteit Twente

The work presented in this PhD thesis is financially supported by the Foundation of Fundamental Research on Matter (FOM) via the Industrial Partnership Program IPP I28 and co-financed by BASF New Business.

Printed by: BOXPress

Front: Artist impression of the magnetoelastic transition in Fe_2P-based materials. Electrons are shown (red, blue and purple) on a hexagonal lattice of atoms (green and orange) that are represented by their core electron cloud. On the bottom of the image, the material is metallic; the electrons are aligned ferromagnetically and are present in bands (blue). Above the Curie temperature, on the top of the image, the electrons become localized and pair up, reducing the magnetic moment and increasing the bond strength.

ISBN 978-94-6295-635-3

An electronic version of this dissertation is available at
http://repository.tudelft.nl/.

Het leven draait niet om het halen van doelen.
Het leven draait om hard werken en doen waar je goed in bent.
Dan zal je op een dag terugkijken op je prestaties
en gelukkig zijn.

Contents

1 Introduction

1.1. Motivation

Refrigeration technology has had a great impact on everyday life since it became widely available in the twentieth century. It increased the living standard by allowing food to be stored for a longer time and decreased illness due to food spoilage[1]. Apart from these positive effects, refrigeration based on vapor compression posed new risks to human health due to the used refrigeration gases. The used gases are generally toxic, detrimental for the ozone layer or are greenhouse gases[2]. This development sparked an interest in refrigeration techniques that do not use the gas-to-liquid phase transition, but focus on the solid-to-solid phase transition. One of the phenomena that can be used in solids is the magnetocaloric effect. Efficiency studies show that a cooling cycle using magnetocaloric materials is also more efficient compared to vapor-compression techniques[3]. With a growing global demand for refrigeration[4,5], the increased efficiency can further decrease the rate by which greenhouse gases are emitted. To maximize the magnetocaloric effect, one has to find and optimize new material systems.

1.2. Magnetocaloric effect

Magnetic refrigeration is based on the magnetocaloric effect (MCE), that is characterized by the isothermal entropy change and adiabatic temperature change resulting from a change in applied magnetic field. The entropy change can be realized in ferromagnetic[6] or paramagnetic[7] materials and is most pronounced at the magnetic transition temperature. In general, the transition is of second order showing a discontinuous change of the heat capacity due to the magnetic transition.

By expressing the entropy S in terms of the heat capacity C

$$S = \int_0^T \frac{C}{T} dT, \tag{1.1}$$

one can construct a schematic drawing that clearly illustrates the magnetocaloric effect for materials having a second-order phase transition, shown in Figure 1.1. When the

1

material is in the paramagnetic state, the application of an external magnetic field shifts the critical point and the material can become ferromagnetic, lowering the heat capacity.

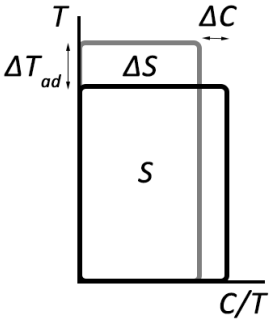

Figure 1.1: Schematic diagram of a second-order phase transition where there is an adiabatic temperature change ΔT_{ad} due to a change in heat capacity ΔC. In the paramagnetic state, the heat capacity is large and the entropy S is given by the surface of the black box. Due to the application of a magnetic field, the material becomes ferromagnetic, with a lower associated heat capacity. The total entropy can initially be kept constant, in accordance with an adiabatic process. The resulting temperature change can subsequently interact with the environment, lowering the entropy of the material.

There are three main contributions to the entropy and heat capacity: structural, magnetic and electronic. A change in magnetization gives rise to a change in heat capacity and thus gives rise to the MCE. This is most pronounced for rare earth-based materials that have a high magnetization associated with the localized $4f$ orbitals. For example, $ErAl_2$ shows a ΔT_{ad} of 6 K for a field change of $0 - 2$ T[8]. The low transition temperatures of rare earth-based materials are usually between 5 and 100 K and make these materials unsuitable for room-temperature applications. The only candidate is Gd with a transition temperature of 292 K, but the cost and limited availability of this material make it impractical to use in large-scale applications.

Instead, cheap and abundant $3d$-based intermetallic compounds with a high magnetization and a T_C around room temperature are preferred for room temperature applications. Because the structural heat capacity saturates to the Dulong-Petit limit (C = 3R) at the Debye temperature (generally between 400 and 500 K), the MCE for these materials is generally small. Instead of using materials showing a second-order phase transition, materials with a first-order phase transition (giant MCE) are used. Especially Fe_2P-based materials are interesting because of their high magnetization, high entropy change and magnetoelastic transition.

For these compounds, there is a coupled magnetic and crystallographic transition, without changing the crystal symmetry. In addition to a ΔC of about 1%[9], there is a simultaneous $enthalpy$ change at the transition, or latent heat, given by $\Delta H = T\Delta S$. This can triple the ΔT_{ad} to about 4.2 K, measured in a field change from $0 - 1.5$ T for FeMn(P,As)[10]. For these materials, the discontinuous change in entropy associated with first-order phase transitions allows tapping into all three entropy reservoirs (lattice, magnetic, and electronic contributions) of the material[11].

In general, the isothermal entropy change and adiabatic temperature change are given by

$$\Delta S_{it} = \int_{B_i}^{B_f} \left(\frac{\partial M}{\partial T}\right)_B dB, \tag{1.2}$$

$$\Delta T_{ad} = -\int_{B_i}^{B_f} \frac{T}{C_p}\left(\frac{\partial M}{\partial T}\right) dB, \tag{1.3}$$

where B_i and B_f are the initial and final applied magnetic fields. Finding the microscopic origin of the coupling between magnetism and the crystal structure is not trivial and is up to now only observed in Mn(As,Sb)[12], La(Fe,Si)$_{13}$ and its hydrides[13], (Mn,Fe)$_2$(P,X) where X = As[14], Ge[15], Si[16] , MnCoGe[17], Gd$_5$(Ge,Si)$_4$[18], FeRh[19] and Heusler alloys[20]. In order to find new promising systems, the origin of this coupling must be understood. This can yield boundary conditions that can guide the quest for new systems.

1.3. Thesis outline

By using diffraction techniques, the magnetoelastic coupling in Fe$_2$P-based magnetocaloric materials as well as in a new material system has been investigated. The fundamental knowledge obtained by the derived and calculated electron density helps to establish the boundary conditions needed for finding new and effective magnetocaloric materials.
First, the role that the (symmetry of the) crystal structure plays in these compounds is discussed in chapter 2. Here the relation between the crystal structure, electronic structure and magnetic properties is introduced. The experimental methods and instruments used to synthesize and characterize the structural and magnetic properties are described in chapter 3.

The next four chapters discuss three different material classes. The first material, discussed in chapter 4, is based on Mn$_3$Ga. For this material a simultaneous crystallographic and magnetization change was reported. The microscopic origin is elucidated by X-ray and neutron diffraction techniques and the applicability of the MCE of this transition is discussed. The second material is discussed in chapter 5 and chapter 6 and is based on Fe$_2$P. In chapter 5, high-resolution X-ray powder diffraction was used to study the electron density in the ferro- and paramagnetic states. Experimental evidence was found to support the theory of mixed magnetism and shows the importance of the presence of different lattice sites occupied by magnetic atoms. The crystallographic properties are discussed in chapter 6 and show that the magnetoelastic coupling in materials showing first-order and second- order phase transitions is essentially the same. YFe$_5$ is discussed in chapter 7, it is chosen for the high concentration of magnetic atoms and has two different lattice sites for magnetic atoms. Although it is expected to crystallize in a CaCu$_5$ type crystal structure, single phase samples could not be attained. To understand the phase stability of these compounds, an empirical model based on the Miedema parameters is introduced. This last study shows how the nature of the elements can facilitate/hinder

the formation of interesting phases and can provide boundary conditions to select new promising materials.

References

[1] L. A. Craig, B. Goodwin and T. Grennes. 'The Effect of Mechanical Refrigeration on Nutrition in the United States.' Social Science History volume 28, pp. 325–336 (2004).

[2] A. McCulloch, P. M. Midgley and P. Ashford. 'Releases of refrigerant gases (CFC-12, HCFC-22 and HFC-134a) to the atmosphere.' Atmospheric Environment volume 37, pp. 889 – 902 (2003).

[3] C. Zimm, A. Jastrab, A. Sternberg et al. Description and Performance of a Near-Room Temperature Magnetic Refrigerator, Springer US, pp. 1759–1766 (1998).

[4] N. Wilson. 'Magnetic Cooling: Camfridge achievements and industry challenges, address at Thermag VII, Turin.' (2016).

[5] D. Coulomb, J.-L. Dupont and A. Pichard. 'The Role of Refrigeration in the Global Economy.' IIR Notes volume 29 (2015).

[6] P. Weiss and A. Piccard. 'Le phénomène magnétocalorique.' J. Phys. volume 5, pp. 103–109 (1917).

[7] W. F. Giauque and D. P. MacDougall. 'Attainment of Temperatures Below 1° Absolute by Demagnetization of $Gd_2(SO_4)_3 \cdot H_2O$.' Phys. Rev. volume 43, pp. 768–768 (1933).

[8] P. J. von Ranke, V. K. Pecharsky and K. A. Gschneidner Jr. 'Influence of the crystalline electrical field on the magnetocaloric effect of $DyAl_2$, $ErAl_2$, and $DyNi_2$.' Phys. Rev. B volume 58, pp. 12110–12116 (1998).

[9] P. Roy, E. Brück and R. A. de Groot. 'Latent heat of the first-order magnetic transition of $MnFeSi_{0.33}P_{0.66}$.' Phys. Rev. B volume 93, p. 165101 (2016).

[10] E. Brück, M. Ilyn, A. M. Tishin and O. Tegus. 'Magnetocaloric effects in $MnFeP_{1-x}As_x$-based compounds.' Journal of Magnetism and Magnetic Materials volume 290–291, Part 1, pp. 8 – 13 (2005).

[11] M. F. J. Boeije, P. Roy, F. Guillou et al. 'Efficient Room-Temperature Cooling with Magnets.' Chem. Mater. volume 28, p. 4901–4905 (2016).

[12] H. Wada and Y. Tanabe. 'Giant magnetocaloric effect of $MnAs_{1-x}Sb_x$.' Appl. Phys. Let. volume 79, pp. 3302–3304 (2001).

[13] A. Fujita, S. Fujieda, Y. Hasegawa and K. Fukamichi. 'Itinerant-electron metamagnetic transition and large magnetocaloric effects in $LaFe_{13-x}Si_x$ compounds and their hydrides.' Phys. Rev. B volume 67, p. 104416 (2003).

[14] E. Brück, M. Ilyn, A. M. Tishin and O. Tegus. 'Magnetocaloric effects in $MnFeP_{1-x}As_x$-based compounds.' J. Magn. Magn. Mater. volume 290-291, pp. 8–13 (2005).

[15] N. T. Trung, Z. Q. Ou, T. J. Gortenmulder et al. 'Tunable thermal hysteresis in MnFe(P,Ge) compounds.' Appl. Phys. Lett. volume 94, p. 102513 (2009).

[16] O. Tegus, E. Brück, K. H. J. Buschow and F. R. de Boer. 'Transition-metal-based magnetic refrigerants for room-temperature applications.' Nature volume 415, pp. 150–152 (2002).

[17] N. T. Trung, L. Zhang, L. Caron et al. 'Giant magnetocaloric effects by tailoring the phase transitions.' Appl. Phys. Lett. volume 96, p. 172504 (2010).

[18] K. A. Gschneidner Jr. and V. K. Pecharsky. 'Giant magnetocaloric effect in $Gd_5Si_2Ge_2$.' Phys. Rev. Lett. volume 78, pp. 4494–4497 (1997).

[19] S. A. Nikitin, G. Myalikgulyev, A. M. Tishin et al. 'The magnetocaloric effect in $Fe_{49}Rh_{51}$ compound.' Physics Letters A volume 148, pp. 363 – 366 (1990).

[20] J. Liu, T. Gottschall, K. P. Skokov et al. 'Giant magnetocaloric effect driven by structural transitions.' Nature Mat. volume 11, p. 620–626 (2012).

2

Theoretical background

2.1. Crystal chemistry

In solids, there are four main cohesive interactions: metallic, covalent, ionic and van der Waals interactions. For the three strongest, the degree to which the interaction is present in a compound can be estimated by using the concept of electronegativity (EN). This was first introduced by Linus Pauling as being the difference in energy between the average bond strength of X-X and H-H compared to X-H, where X is the element of interest and H is used as reference [1]. These values can be found in the appendix.

These interactions are one of the main driving forces for the arrangement of atoms on a lattice. This principle can also be reversed: the interaction between atoms can be gauged by looking at the crystal structure. Compounds with equal and high EN, attain the lowest energy by pairing electrons with neighbors, giving rise to covalent bonds. This is the case for C, where in diamond all four valence electrons are bound and all C atoms have four nearest neighbors. This gives rise to a low number of nearest neighbors and specific bond angles. In contrast, compounds with equal and low EN, attain the lowest energy when the electrons are delocalized. For fcc Fe, the electrons are shared between 12 nearest neighbors in a close-packed atomic arrangement. Compounds with more than one atomic species and different EN values ionize. This gives rise to a packing where all anions are paired with cations, according to their stoichiometry, to maximize the Coulomb interaction. The most interesting compounds, from high-T_c superconductors like (Ba,K)Fe_2As_2 [2] to magnetocaloric materials like Fe_2P [3], show a mix of these interactions, as is made clear in chapter 5. In this thesis the focus will be on intermetallics. This class of materials shows a large variety of different possible (close-packed) atomic arrangements. In order to understand this class of materials, one needs to understand and classify the different crystal structures that can be adopted.

2.1.1. Crystal structures of intermetallic compounds

Intermetallic compounds can form in various compositional ranges. Unlike covalent and ionic solids, where the stoichiometry is fixed by the number of bonds or the charge, the observed stoichiometries in intermetallic compounds is distinctly different. The complexity of intermetallic compounds can be illustrated when subjecting covalent or ionic solids to high pressure. Because this induces a close packing of the atoms, the material becomes metallic. In the case of the archetypical salt NaCl, additional phases like Na_3Cl, Na_2Cl, Na_3Cl_2 are stable with excess Na, and $NaCl_3$, $NaCl_7$ are stable in excess Cl[4]. These stiochiometries, that defy chemical intuition, are very common for intermetallic compounds and need to be described using a different classification. This is done by using a prototype compound that describes the atomic arrangement.

For a hexagonal close-packed (hcp) crystal structure, the packing of Mg is used as prototype. Several modifications can be distinguished that lead to different prototypes. The most common modifications are shown in Figure 2.1. The type of transformations are listed in Table 2.1. For example, an ordered substitution of ¼ of the atoms in Mg will lead to the Mg_3Cd prototype, discussed in chapter 4. Multiple substitutions lead to the $MgZn_2$ Laves phase, while a redistribution leads to the $CaCu_5$ prototype, discussed in chapter 7. This classification will be used throughout this thesis.

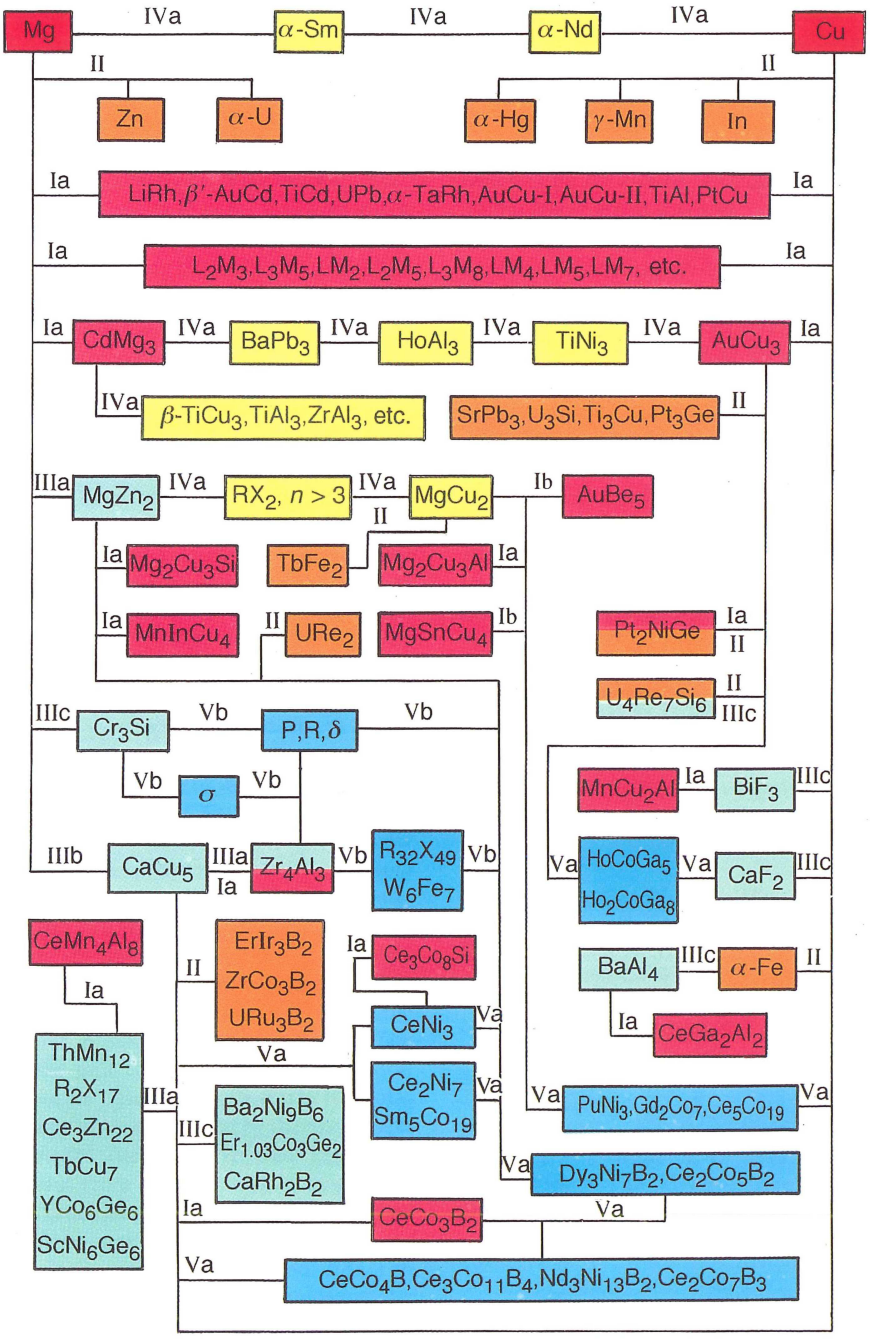

Figure 2.1: Relationships between structure types of intermetallic compounds[5]. The color code corresponds to the types of transformation indicated with roman numerals.

Table 2.1: Relationships between structure types of intermetallic compounds showing common features and ways of transformation[5].

Common features of structure types	Ways of transforming	Examples of structure types Parent → transformed structure
Equal positions for all atoms	Ia Ordered substitution (superstructure formation)	$Cu \rightarrow AuCu_3$, $ThMn_{12} \rightarrow CeMn_4Al_8$
	Ib Redistribution of the different component atoms	$MgCu_2 \rightarrow AuBe_5$, $MgSnCu_4$
Approximately equal positions for all atoms	II External deformation[b] Internal deformation	$Cu \rightarrow \alpha$-Mn $MgCu_2 \rightarrow TbFe_2$
Equal positions for only part of the atoms	IIIa Multiple substitution	$CaCu_5 \rightarrow ThMn_{12}$, Zr_4Al_3
	IIIb Redistribution of the atoms or substitution of an atomic group	$Th_2Ni_{17} \rightarrow Th_2Zn_{17}$
	IIIc Inclusion or elimination and redistribution of included atoms	$Cu \rightarrow \gamma$'-Fe_4N[1], $Mg \rightarrow CdI_2$[a], FeS_2[a]
All structure details (fragments) are equal	IVa Homeotectics (stackings of closely packed networks)[c]	$CdMg_3 \rightarrow BaPb_3$, $MgZn_2 \rightarrow MgCu_2$
	IVb Certain modes of stacking of slabs (polyhedra), homogeneous homologous series [d]	$AlB_2 \rightarrow \alpha$-$ThSi_2$[a], Zr_5Si_4[a] $\rightarrow Sm_5Ge_4$[a]
Details (fragments) are only partially equal	V Inhomogeneous homologous series, interchanges different in two or more details	
	Va One-dimensional	$(AuCu_3, CaF_2) \rightarrow HoCoGa_5$, Ho_2CoGa_8
	Vb Two-dimensional	$Zr_4Al_3 \rightarrow \sigma$ phase, P phase, μ phase
	Vc Three-dimensional	$(AlB_2, \alpha\text{-Fe}) \rightarrow Ce_{24}Co_{11}$[a]

[a] These structure types do not belong to the family of close packing. They are shown for illustration of the transitions IIIc, IVb and Vc.

[b] External deformation is connected with changing of the c/a ratio.

[c] The term homeotectic was suggested by Laves and Witte and is related to structures that have similar composition and equal CN but different ways of mutual placement of the fragments

[d] Homology suggests the possibility of the construction of structures with similar sets of fragments but with different quantitative ratios.

2.2. Phase stability

The stability of the crystal structures mentioned in the previous section will now be described using thermodynamic properties. Especially for elastic or structural phase transitions commonly found in giant magnetocaloric materials, analysis of the Gibbs free energy has been proven to be most useful. The Gibbs free energy is given by

$$G = H - TS \tag{2.1}$$

where H is the enthalpy and S is the entropy.

2.2.1. The role of entropy

The entropy can be expressed as

$$S = k_B ln W \tag{2.2}$$

where k_B is the Boltzmann constant. Using this formulation, the entropy is dependent on the number of possible configurations W. In a highly symmetric system, a given atom can be distributed between a number (g) of symmetry-related positions. Removal of a symmetry element then produces n sets of g/n equivalent positions, reducing or eliminating the choice, and causing a decrease in S. This is beautifully illustrated for WO_3[a]. WO_3 undergoes five transitions from low to high temperature: monoclinic $\rightarrow$ triclinic $\rightarrow$ monoclinic $\rightarrow$ orthorhombic $\rightarrow$ tetragonal $\rightarrow$ hexagonal[6]. Apart from the first transition, this is exactly what is expected. In chapter 4, Mn_3Ga is discussed that shows two successive phase transitions as a function of temperature.

2.2.2. The role of enthalpy: the Miedema model

The enthalpy of formation was modelled by Miedema et al.[7] to predict phase stability of intermetallic compounds using a semi-empirical model. To evaluate the formation enthalpy ΔH, two contact interactions at the interface of bulk metals are considered. The general assumption of this model is that these interactions dominate at the atomic level. When two metals are brought into contact with each other, the difference in work function will cause a charge to flow, resulting in a dipole layer. This dipolar interaction corresponds to a negative contribution to the enthalpy of formation and is given for atom A in a matrix of B

$$\Delta H_{dip} = -P V_A^{2/3} (\Delta\Phi)^2 / < n_{WS}^{1/3} >, \tag{2.3}$$

where $V_A^{2/3}$ is the contact-surface area, $< n_{WS}^{1/3} >$ is the average electron density at the boundary of the Wigner-Seitz cell, $\Delta\Phi$ is the difference in work function of A and B and P is a constant. The second contribution to the interface energy is based on an electron density mismatch. In order to remove any discontinuities in the electron density, energy is needed to excite electrons to higher energy states. This positive term to the enthalpy of formation is given by

$$\Delta H_{sol} = Q V_A^{2/3} (\Delta n_{WS}^{1/3})^2 \tag{2.4}$$

[a] This was pointed out to me by Stephen Blundell at the European Summer school on Magnetism (2015).

where Q is a constant. The interfacial enthalpy of A surrounded by B yields

$$\Delta H_{AB} = \frac{V_A^{2/3}}{< n_{WS}^{1/3} >}(-P(\Delta\phi^*)^2 + Q(\Delta n_{WS}^{1/3})^2), \tag{2.5}$$

where P and Q are dependent on the atomic species. The total entropy change can be determined by taking the concentration c into account:

$$\Delta H = c_A c_B (f_B^A \Delta H_{AB} + f_A^B \Delta H_{BA}) \tag{2.6}$$

where f_B^A represents the degree to which A is surrounded by B, given by

$$f_B^A = c_B^s (1 + \gamma (c_A^s c_B^s)^2). \tag{2.7}$$

The factor γ takes the values of 8, 5 and 0 for intermetallics, metallic glasses and solid solutions respectively and c_A^s is the surface concentration of A, given by

$$c_B^s = \frac{c_B V_B^{2/3}}{c_A V_A^{2/3} + c_B V_B^{2/3}}. \tag{2.8}$$

For the formation of stable alloys, $\Delta H < 0$ and rewriting Equation 2.5 leads to

$$\Delta\Phi \propto Q/P\Delta n_{WS} - \Delta H \tag{2.9}$$

If $\Delta\Phi$ is plotted versus Δn_{WS}, like shown in chapter 7, one can separate combinations of elements that prefer to mix and ones that do not form stable alloys. All values have been tabulated for elements in the metallic state[7] and can be found in the appendix.

2.3. Phase transitions

As a single composition can exhibit various symmetries, we can now focus on the transitions between them. In general, phase transition processes can be divided into two classes: first-order phase transitions and second-order phase transitions. First-order phase transitions show a discontinuous change in the order parameter and second-order phase transitions show a continuous change (the second derivative being discontinuous). A phase can be described by the free energy, that is dependent on thermodynamical variables such as temperature, pressure and magnetic field. To do this, the potential is considered as a function of the crystal structure and can be characterized by the density function $\rho(x, y, z)$ [8,9]. The parameter of interest (order parameter) is therefore the electron density in the crystal. To describe the density in terms of the point group G_0 at the transition, it can be written down in terms of basis functions $\Psi_i^{(n)}$ of the irreducible representations

$$\rho = \sum_n \sum_i c_i^{(n)} \Psi_i^{(n)} \tag{2.10}$$

where n is the number of the irreducible representation and i is the number of the function at its basis. To describe any changes as a function of the crystal structure, ρ is rewritten by isolating the identity representation

$$\rho = \rho_0 + \Delta\rho = \rho_0 + \sum_n{}' \sum_i c_i^{(n)} \Psi_i^{(n)}. \tag{2.11}$$

The prime means that the identity representation is excluded from the summation. At the transition, either $\Delta\rho$ changes or $\Delta\rho = 0$, which requires all $c_i^{(n)} = 0$. The latter corresponds to a second-order transition, where all the $c_i^{(n)}$ reduce to zero continuously and take infinitely low values near the transition point. In this case, the crystal transforms from a high symmetric point group G_0 to a low symmetric point group G_1. Despite the fact that the symmetry changes discontinuously, the physical properties remain constant at the transition temperature. An example can be found in chapter 4. If the $c_i^{(n)}$ coefficients change discontinuously, the transition is of first order. In the case where G_1 is not a subgroup of G_0, it is impossible to continuously transform one into the other and the transition has to be first order. Point group relations are described in Figure 2.2.

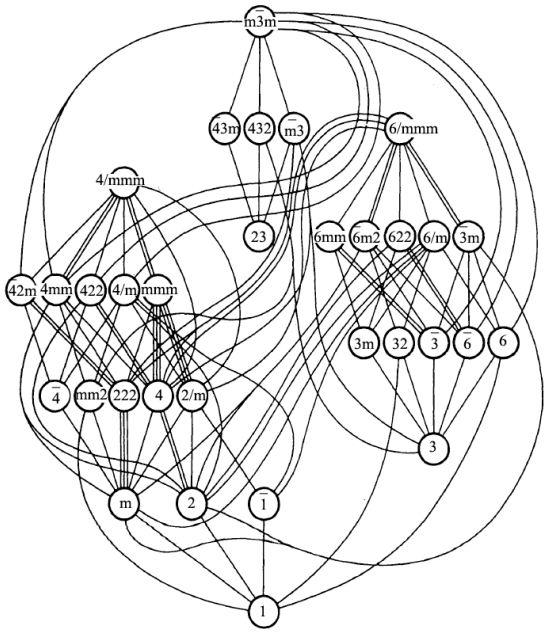

Figure 2.2: Subgroup relations where the number of atoms in the unit cell is constant (no supercell formation). The straight lines indicate one-dimensional representations, the curves indicate multi-dimensional representations[8].

To discriminate between first- and second-order phase transitions, the analysis can be taken further by considering the thermodynamic Gibbs free energy $G(\eta, P, H, T)$. In the vicinity of the transition, the potential can be described in terms of a polynomial expansion as function of the general order parameter η:

$$G = G_0 + a_1\eta + a_2\eta^2 + a_3\eta^3 + a_4\eta^4 + a_5\eta^5 + a_6\eta^6 + ... \tag{2.12}$$

where G_0 is the equilibrium value of the thermodynamic potential at the critical temperature. When considering a structural phase transition, η corresponds to $c_i^{(n)}$, in magnetic phase transitions η corresponds to the magnetization M. The evaluation of these so-called Landau coefficients yields $a_i = 0$ for specific values of i[8,9]. This discussion will prove useful in discriminating between first- and second-order magnetic phase transitions. To describe a magnetic system, the change in free energy can be described by

$$\Delta G = \frac{\alpha}{2}M^2 + \frac{\beta}{4}M^4 + \frac{\gamma}{6}M^6 - \mu_0 HM. \tag{2.13}$$

where $\mu_0 H$ is the applied field and $\gamma > 0$. At the transition, the potential can be evaluated considering $\partial G/\partial M = 0$:

$$\alpha + \beta M^2 + \gamma M^4 = \mu_0 H/M. \tag{2.14}$$

The parameter $\alpha = \alpha_0(T - T_0)$ with $\alpha_0 > 0$ ensures that $M \neq 0$ for $T < T_0$ and $M = 0$ for $T \geq T_0$. The other coefficients are considered to be temperature independent. The equation can be solved easily in the absence of a magnetic field. The coefficients can be determined experimentally using an Arrott plot [10,11], where $\mu_0 H/M$ is plotted as a function of M^2. When $\beta < 0$, there are three minima and the free energy diagram looks like Figure 2.3. This corresponds to a first-order transition. For $\beta > 0$ only two minima are found, corresponding to a second-order transition. The behavior of materials showing various values for β is investigated in chapter 6.

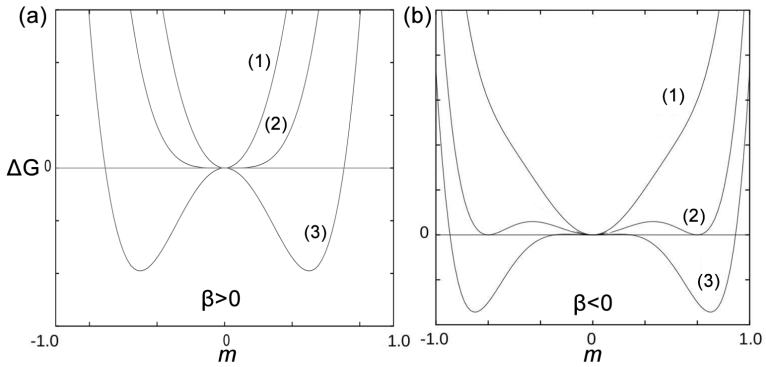

Figure 2.3: Free energy difference $\Delta\Phi$ as a function of the normalized magnetization $m = M/M_s$ where M_s is the saturation magnetization. In (a), $\beta > 0$ and describes a second order phase transition, in (b) $\beta < 0$ that describes a first-order phase transition. (1) High temperature, with only the paramagnetic phase being stable; (2) the ferromagnetic phase is metastable but still separated from the paramagnetic phase by a free-energy barrier; (3) the free-energy barrier is gone and only the ferromagnetic state is stable.

The presence of a nucleation barrier is illustrated for ferromagnetic materials showing a first-order magnetic transition. At high temperatures, the material will be in the paramagnetic state. Below a critical temperature T_C, the ferromagnetic state will have a lower energy, but will not be formed initially. The kinetic barrier will retard the nucleation of the ferromagnetic state. Once the barrier is overcome, the ferromagnetic state will be readily formed and the magnetization will experience a jump. Since the entropy is the derivative of the free energy with respect to the temperature, it will also show a jump.

2.3.1. Magnetoelastic coupling in hexagonal systems

In magnetic material systems there is a coupling between magnetism and unit cell parameters. In case of a volume change, this coupling gives rise to the magnetovolume effect, where there is a volume contraction when the system becomes paramagnetic. This magnetoelastic coupling can be characterized by the Landau theory of phase transitions by adding elastic terms and a bilinear magnetoelastic coupling to the free energy

$$\Delta G = \frac{\alpha}{2}M^2 + \frac{\beta}{4}M^4 + \frac{\gamma}{6}M^6 - \mu_0 HM + \frac{1}{2}\sum_{i,k} C_{ik}e_i e_k + \sum_i \xi_i e_i M \tag{2.15}$$

where C_{ij} are elastic constants, e_i is the elastic strain and ξ_i is the magnetic coupling constant. The strain and magnetoelastic coupling can be expanded for a hexagonal system [12]. The (symmetric) elasticity tensor has the following form:

$$C_{ij} = \begin{pmatrix} C_{11} & C_{12} & C_{13} & 0 & 0 & 0 \\ C_{12} & C_{11} & C_{13} & 0 & 0 & 0 \\ C_{13} & C_{13} & C_{33} & 0 & 0 & 0 \\ 0 & 0 & 0 & C_{44} & 0 & 0 \\ 0 & 0 & 0 & 0 & C_{44} & 0 \\ 0 & 0 & 0 & 0 & 0 & C_{66} = \frac{1}{2}(C_{11} - C_{12}) \end{pmatrix}$$

Because $e_1 = e_2$, $e_4 = e_5 = e_6 = 0$, the change in Gibbs free energy becomes

$$\Delta G = 2(C_{11} + C_{12})e_1^2 + 4C_{13}e_1 e_3 + C_{33}e_3^2 + 2\xi_1 e_1 M + \xi_3 e_3 M \tag{2.16}$$

and can be evaluated at the phase transition

$$\frac{\partial \Delta G}{\partial M} = (\alpha + 2\xi_1 e_1 + \xi_3 e_3)M + \beta M^3 + \gamma M^5 - \mu_0 H = 0 \tag{2.17}$$

$$\frac{\partial \Delta G}{\partial e_1} = 4(C_{11} + 2C_{12})e_1 + 4C_{13}e_3 + 2\xi_1 M = 0 \tag{2.18}$$

$$\frac{\partial \Delta G}{\partial e_3} = 4C_{13}e_1 + 2C_{33}e_3 + \xi_3 M = 0. \tag{2.19}$$

This yields three coupled equations. The bilinear magnetoelastic coupling in the first equation effectively adds two terms to α. Assuming $\mu_0 H = 0$, this equation has a trivial solution ($M = 0$) and non-trivial solutions, given by:

$$\alpha + 2\xi_1 e_1 + \xi_3 e_3 + \beta M^2 + \gamma M^4 = 0. \tag{2.20}$$

This changes $\alpha = \alpha_0(T - T_0)$ in Equation 2.14 and shifts T_C to higher temperatures. Similarly, linear quadratic terms will affect β. The remaining coupled equations result in

$$\frac{e_1}{M} = \frac{\xi_1 C_{33} - \xi_3 - C_{13}}{2C_{13}^2 - C_{33}(C_{11} + C_{12})} \tag{2.21}$$

$$\frac{e_3}{M} = \frac{\xi_3(C_{11} + C_{12}) - 2\xi_1 C_{13}}{2C_{13}^2 - C_{33}(C_{11} + C_{12})}. \tag{2.22}$$

By measuring e as a function of M, the magnetoelastic coupling constants can be experimentally determined, and can be found in chapter 6.

2.4. Magnetic properties

In this section, two models describing the properties of magnetic materials are discussed. They are applicable to itinerant systems, that are of particular interest for magnetocaloric applications. Itinerant magnetic systems are especially suited for this purpose, due to the high concentration of magnetic atoms resulting in a potentially high magnetization. Within the group of materials with itinerant electrons, two kinds of magnetism can be distinguished. The first is characterized by a very weak band splitting where the spin-up and spin-down states are very close to the Fermi level[13], resulting in a low magnetization and low transition temperature. The second is characterized by a strong band splitting, resulting in a high magnetization and high transition temperatures.

2.4.1. Saturation magnetization

The saturation magnetization determines the maximum magnetic entropy change and therefore strongly influences the magnitude of the magnetocaloric effect. The origin of the saturation magnetization in itinerant magnets is of quantum mechanical nature and is intuitively difficult to understand. One approach is to use the chemical concept of bonding[14]. This will be explained using Fe as an example.

At room temperature, Fe assumes a body-centered cubic (bcc) arrangement. In this arrangement, a central Fe atom is surrounded by 8 nearest neighbors at 2.5 Å and 6 next nearest neighbors at 2.9 Å. The atomic electronic configuration is $[Ar]3d^6 4s^2$, so at the Γ point three filled t_{2g} orbitals and two empty e_g orbitals are present. In a band picture the high symmetry lines in the Brillouin zone are plotted as a function of energy. By summing these states over all orientations the density of states is obtained. The t_{2g} orbitals have a better overlap, giving rise to broader bands compared to the e_g orbitals. The total of three peaks in the DOS is characteristic for a bcc metal.

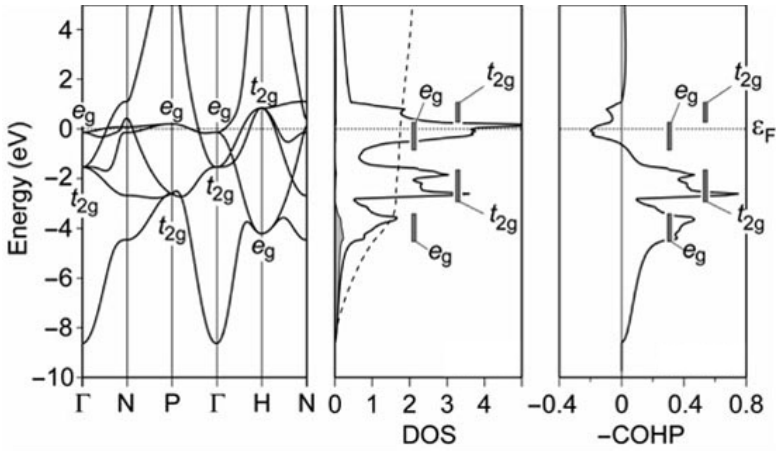

Figure 2.4: Band structure, DOS and Fe-Fe COHP of bcc iron, calculated without spin polarization. The dashed line in the DOS curve corresponds to the projected DOS of the Fe $4s$ orbital and its integration[14].

Like in molecular bonding, for each two orbitals that are mixed, a bonding and an anti-bonding orbital are formed. This is illustrated by the Crystal Orbital Hamilton Population (COHP), where the DOS is separated into bonding (+) and anti-bonding (-) bands shown in Figure 2.4. In the case of Fe, there is occupation of anti-bonding states, destabilizing the crystal structure. One way of stabilizing the material is to adopt another crystal structure, but this does not happen. Instead the electrons shift in energy, splitting into a spin-up and spin-down band. In chapter 5, we will show an example where a change in bonding results in a change band splitting, resulting in a change of magnetic moment.

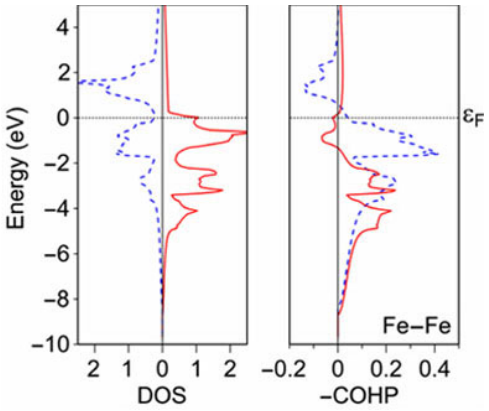

Figure 2.5: DOS and COHP of bcc iron, calculated with spin polarization[14]. Spin-up and spin-down are indicated by the red and blue (dotted) lines.

A spin polarized calculation yields the spin-up (red, solid line) and spin-down (blue, dotted line) occupation (Figure 2.5). The shape of both densities of states is more or less the same, but they are shifted with respect to each other. The Fe-Fe bonding is now maximized by removing electrons from the anti-bonding band.

2.4.2. Transition temperature

For weakly magnetic systems, the Stoner model is used to describe the transition temperature. For systems like $ZrZn_2$, the transition temperature is determined by exciting spin-up electrons into the spin-down band by increasing temperature. The T_C is given by

$$T_C^2 = T_F^2(I_s N(\epsilon_F) - 1) \tag{2.23}$$

where $T_F = \epsilon_F / k_B$ is the Fermi degeneracy temperature corrected for the effective electron mass and I_s is the Stoner exchange parameter averaged over the one-electron states.

In strong magnetic systems the Stoner model breaks down and leads to an overestimation of the Curie temperature. For these systems, the magnetic moments persist above the Curie temperature but lose long range order. Therefore, spin fluctuations are used to describe such a system, replacing the magnetic moment by the spin density. Then, using a Landau expansion, the free energy can be modeled[15].

Using this model, one can define a spin fluctuation temperature T_{SF}

$$T_{SF} = \frac{M_0^2}{10 k_B \chi_0} \tag{2.24}$$

where M_0 is the total magnetic moment of the unit cell in μ_B at 0 K and χ_0 is the exchange enhanced susceptibility at equilibrium

$$\chi_0^{-1} = \left(\frac{1}{4\mu_b^2}\right)\left(\frac{1}{N^+(\epsilon_F)} + \frac{1}{N^-(\epsilon_F)}\right) - 2I_s \tag{2.25}$$

where I_s is the Stoner exchange parameter. For materials where the critical temperature is dominated by spin fluctuations, T_C is approximated by T_{SF}. At the other extreme, there is the Stoner theory, taking into account single particle excitations only, a description which may be valid for systems where T_{SF} is large compared with T_C. This leads to the Mohn-Wohlfarth model

$$\frac{T_C^2}{T_C^{S2}} + \frac{T_C}{T_{SF}} - 1 = 0 \tag{2.26}$$

The validity of this model was investigated by plotting T_C/T_{SF} as a function of T_C^S/T_{SF} for various materials in Figure 2.6. For Fe, Co and Ni, which have T_C values of 770, 1115 and 354°C (1043, 1388 and 627 K) and magnetic moments of 2.2, 1.7 and 0.6 μ_B respectively, the calculated values agree within an error or 3-5%. For Fe, the high magnetic moment leads to a high T_C. For Co, the increased density of states contributes to the high T_C. For Ni, the lower T_C can be attributed to the reduced magnetic moment. The model has been applied in chapter 6.

Although this model is not state of the art, it can approximate the Curie temperature quite well as long as there is no phase transition affecting the magnetism of the material. Extending this model by using a Heisenberg model and Monte Carlo simulations does not significantly improve the predictions[17]. In addition, methods that use a finite temperature DFT approach are still far from usable[18]. In case of phase transitions, other DFT methods that model the ferro- and paramagnetic phases individually have been used successfully[19].

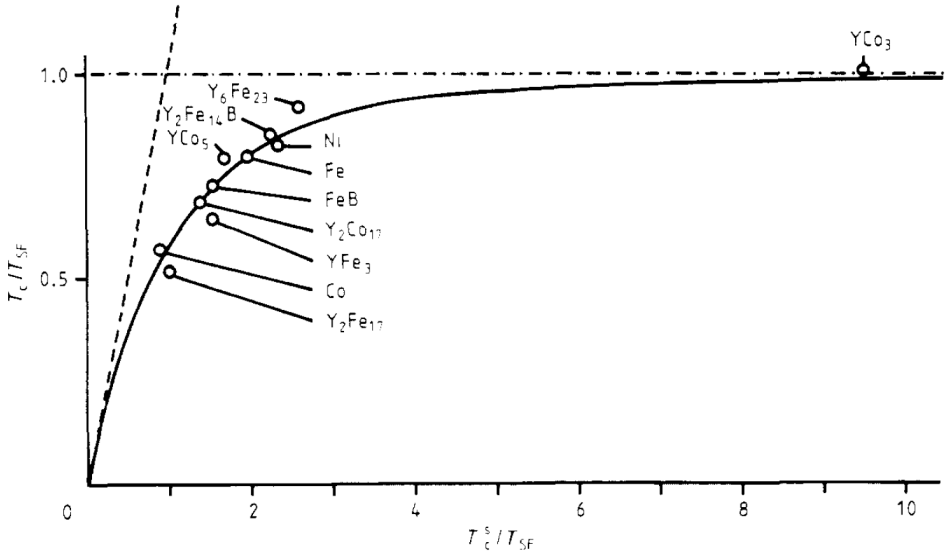

Figure 2.6: The solutions of Equation 2.26 (full curve) and the actual values for 12 different systems (open circles). The broken line is the limit for pure Stoner behavior whereas the asymptotic limit for pure fluctuation behavior is given by the chain line. The theory accurately describes the Curie temperatures of Fe, Ni and Co [16].

References

[1] L. Pauling. 'The nature of the chemical bond. IV The energy of single bonds and the relative electronegativity of atoms.' J. Am. Chem. Soc. volume 54, p. 3570–3582 (1932).

[2] H. Q. Yuan, J. Singleton, F. F. Balakirev et al. 'Nearly isotropic superconductivity in (Ba,K)Fe_2As_2.' Nature volume 457, pp. 565–568 (2009).

[3] O. Tegus, E. Brück, K. H. J. Buschow and F. R. de Boer. 'Transition-metal-based magnetic refrigerants for room-temperature applications.' Nature volume 415 (2002).

[4] W. Zhang, A. R. Oganov, A. F. Goncharov et al. 'Unexpected stable stoichiometries of sodium chlorides.' Science volume 342, pp. 1502–1505 (2013).

[5] J. H. Westbrook and R. L. Fleischer. Intermetallic compounds I. John Wiley and sons ltd. (2000).

[6] H. A. Wriedt. 'The O-W (oxygen-tungsten) system.' Bull. Alloy Phase Diagr. volume 10, pp. 368–384 (1989).

[7] A. R. Miedema, P. F. de Châtel and F. R. de Boer. 'Cohesion in alloys — fundamentals of a semi-empirical model.' Physica B+C volume 100, pp. 1 – 28 (1980).

[8] B. K. Vainshtein, V. M. Fridkin and V. L. Indenbom. Modern Crystallography II. Springer-Verlag (2000).

[9] L. Landau. 'On the theory of phase transitions.' Zh. Eksp. Teor. Fiz. volume 7, pp. 19–32 (1937).

[10] A. Arrott. 'Criterion for Ferromagnetism from Observations of Magnetic Isotherms.' Phys. Rev. volume 108, pp. 1394–1396 (1957).

[11] W. I. Khan and D. Melville. 'Landau theory of magnetic phase diagrams and first order magnetization processes.' J. Magn. Magn. Mater. volume 36, pp. 265–270 (1983).

[12] J. F. Nye. Physical properties of crystals. Oxford university press (1957).

[13] P. F. D. Chatel and F. R. D. Boer. 'The theory of very weak itinerant ferromagnetism applied to Ni_3Ga and Ni_3Al.' Physica volume 48, pp. 331 – 344 (1970).

[14] G. A. Landrum and R. Dronskowski. 'The orbital origins of magnetism: from atoms to molecules to ferromagnetic alloys.' Angew. Chem. Int. Ed. volume 39, pp. 1560–1585 (2000).

[15] P. Mohn. Magnetism in the solid state. Springer-Verlag (2003).

[16] P. Mohn and E. P. Wohlfarth. 'The Curie temperature of the ferromagnetic transition metals and their compounds.' J. Phys. F: Met. Phys. volume 17, pp. 2421–2430 (1987).

[17] N. M. Rosengaard and B. Johansson. 'Finite-temperature study of itinerant ferromagnetism in Fe, Co, and Ni.' Phys. Rev. B volume 55, pp. 14975–14986 (1997).

[18] S. Pittalis, C. R. Proetto, A. Floris et al. 'Exact Conditions in Finite-Temperature Density-Functional Theory.' Phys. Rev. Lett. volume 107, p. 163001 (2011).

[19] P. Roy, E. Brück and R. A. de Groot. 'Latent heat of the first-order magnetic transition of $MnFeSi_{0.33}P_{0.66}$.' Phys. Rev. B volume 93, p. 165101 (2016).

3

Experimental methods and instruments

3.1. Introduction

This chapter describes the sample preparation methods and the used instruments. Samples were prepared using an arc-melting furnace[1] and a melt-spinning device[2] followed by an annealing step. The crystallographic phases were characterized by X-ray and neutron diffraction. Magnetic properties were measured using various magnetometers. X-ray absorption experiments were performed at a dedicated setup in the European synchrotron facility at Grenoble, France.
Section 3.2 is dedicated to a new setup of an arc melting furnace, constructed to replace and improve an older instrument. It was constructed to ensure high quality samples, by minimizing contamination by oxidation[3]. Not only does oxidation alter the material properties, in some cases it can increase the melting temperature considerably. In that case, a high electrical power is needed to produce these samples, which promotes evaporation. High-quality samples are important because some systems are very sensitive to impurities. For instance, the superconductivity[4] or exotic magnetic states[5] are strongly affected by impurities and defects[6]. Relevant elemental properties like melting points and formation energies of oxides are listed in chapter 8.

3.2. Arc melting furnace

3.2.1. Main chamber

The furnace is composed of a main chamber, copper crucible and torch (Figure 3.1). The bottom plate of the main chamber is set on a hydraulic lift and has three connections. The first (14) is the crucible connection that has a KF25 stainless steel co-seal. An O-ring with centering ring was not used because it promotes leakage due to the water pressure in combination with the high vacuum. The second connection is an electrical feedthrough (18) which is directly connected to the crucible, minimizing any electrical

resistance. The third connection is the vacuum outlet for the argon flow, and is located behind 18 in the figure.

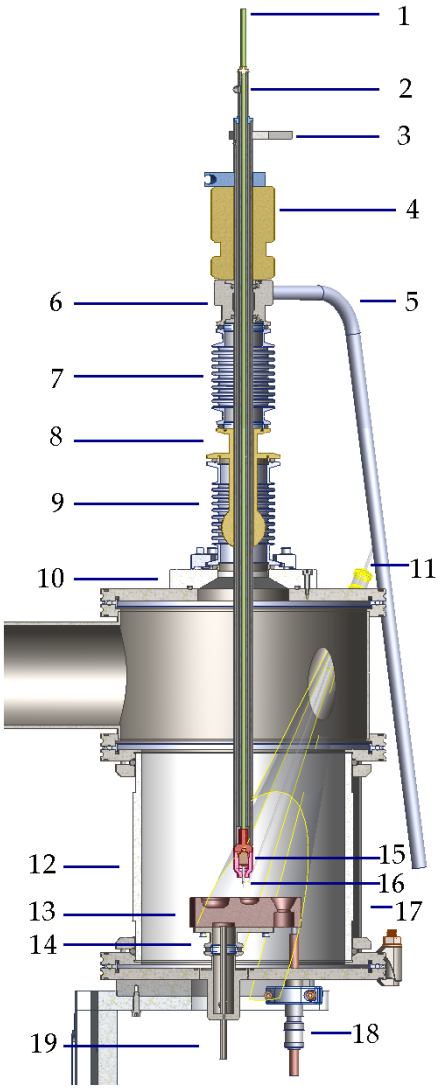

Figure 3.1: Schematic drawing of the setup. 1. Ar inlet 2. Torch cooling 3. Power connection (-) 4. Height manipulator 5. Handle 6. Vacuum seal 7. Z-bellow 8. Bellow insert 9. XY bellow 10. Paque insulation 11. Wobble stick 12. Glass cylinder 13. Crucible 14. Crucible connection 15. Alumina cap 16. Tungsten electrode 17. Paque insulation 18. Power connection (+) 19. Crucible cooling

The main chamber is composed of a glass cylinder (12) that has been cut to precisely fit in the metal seal, which incorporates an O-ring. The glass rests on a soft aluminum layer that allows a vacuum level of at least 10^{-6} mbar. The metal seals on the top and

bottom are kept together by paque strips (17) which are placed along the edge. The top part of the arc furnace is stationary and has been electrically isolated by a paque layer (10). The bellow insert (8) prevents the torch from making contact with the upper part, that can cause stray currents to affect the turbopump and the gauges. A wobble stick (11) is used as a sample manipulator to easily turn the samples. The torch is controlled manually by two handles (5), one on each side. The torch is sealed at (6) by two O-rings, that are pressed into a notch and held by a metal ring that is screwed into the stainless steel piece. The torch is composed of three layers, separating the two water flow directions and the argon gas.

3.2.2. Vacuum system

The vacuum is controlled by a membrane pump (nXDS6i from Edwards) and a turbopump (nEXT240D from Edwards) and is monitored by a pirani-type vacuum gauge (AGP100), a wide-range gauge (WRG-S) and a piezogauge (ASG2). The pirani gauge can measure the pre-vacuum from ambient pressure to 10^{-3} mbar, the wide-range gauge can measure from ambient down to 10^{-9} mbar and the piezogauge can measure down to 1 mbar and is used to control the argon pressure. Two needle valves (which have a sensitivity of 0.1 L/min) control the argon flow, that is sustained by a separate small laboratory pump. A separate pump was used to create an argon flow, thereby preventing any gases formed in the melting process to enter the membrane pump. In addition, the argon flow is filtered by steel wool, that is used because of the low cost. The system is controlled by a programmable logic controller (PLC, type HTB1C0DM9LP) that has an integrated touchscreen. The pumps, valves and gauges are directly connected to the PLC.

3.2.3. Electrical system

A DC power supply (IMS TIG 161) with a low voltage (< 20 V) and an adjustable current between 10 and 160 A is used as generator. The maximum current is around 100 A for the standard 2.4 mm electrode (Binzel, E3 tungsten alloy) but is higher for thicker electrodes. The voltage of the IMS TIG 161 generator is given by $\Delta V(V) = 0.04I(A) + 10$ and the power is given by $P = \Delta V I$. A current of 90 A can be sustained for any period of time, but 100 A can only be sustained for 0.6 minutes and 160 A can be sustained for 0.2 minutes without the machine overheating. Good electrical conductivity between the generator, the torch and the crucible is very important for the stability of the arc and the heating of the sample. The torch should be attached to the (-) side and the crucible to the (+) side. This way the electrons will travel from the crucible to the torch and loose their energy in the sample, heating it up. The other way around the electrode will heat up and melt above 25 A. Switching the connections could be a solution if the power is too high and one needs to gently heat the sample. To ensure a stable arc, the connection between (18) and the crucible needs to have a large contact surface and a tight connection.

3.2.4. Cooling system

The cooling system consists of four valves and one flow meter. The first two valves are external and have to be operated manually. The water system will always run when the external switches are turned on and this enables cooling of the turbopump. The other two valves are solenoid valves (type EV210B from Danfoss) and allow water into the crucible and torch. The flow meter is capable of measuring a range between 0.5 and 30 L/min. The connections are push-in fittings from Festo; they allow easy removing of the tubes. The water flow inside the crucible was simulated using the Ansys Academic R14.5 software and is shown in Figure 3.2. Details on operating the instrument can be found in the manual.

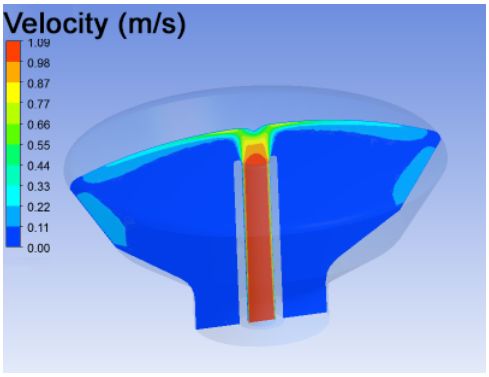

Figure 3.2: Simulation of the velocity of the water flow shown in a cross section of the copper crucible. The water (3.5 10^5 Pa) enters the crucible from the center, disperses at a notch on the inner wall and exits from the side. This design ensures an equal distribution of water across the inner surface.

3.3. Melt spinning

To study metastable phases, the melt spinning technique was used. Intermetallic compounds in the solid state exist either as a solid solution, where any composition is stable, or have a fixed stoichiometry. In the liquid state at sufficiently high temperatures, solutions can be made with any composition, and by rapidly quenching the liquid to room temperature it is possible to retain the starting composition. This is shown in Figure 3.3. Using this technique, synthesis of metastable phases is attainable and can increase the compositional range of a particular phase. This is the basis for melt spinning, where quenching is achieved by spraying a liquid onto a rotating copper wheel, achieving cooling rates in the order of 10^4 - 10^7 K/s[7]. The wheel is rotating at a speed of 60 m/s. The resulting ribbons can be crystalline or amorphous, depending on the elements present.

There are two additional advantages to this technique. First of all, arc melting can always leave some inhomogeneities in the sample due to the nonuniform temperature when melting. The induction furnace used in melt spinning makes sure that the samples are homogeneous. Secondly, hard materials are difficult to process and powderization of samples is not always trivial. The resulting ribbons require short annealing times and

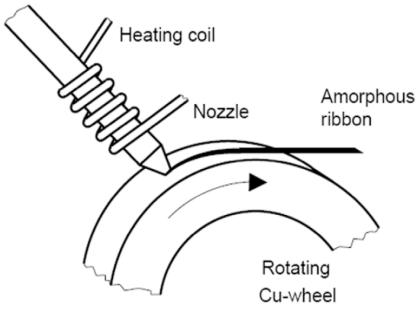

Figure 3.3: Schematic view of the melt spinning technique. A heating coil liquifies a sample, that is sprayed through a nozzle onto a rotating copper wheel, creating (amorphous) ribbons[8].

are perfectly suited for characterization by X-ray diffraction. This is due to the high density and the fact that no force has been applied to the sample in order to achieve powderization. The melt spinner is a commercial product instrument by Edmund Bühler GmbH.

3.4. Annealing

The samples obtained by arc melting or melt spinning were annealed in a tube furnace. To protect the samples from oxidation, they were first sealed into quartz ampoules in an Ar atmosphere of 200 mbar. The melt spun ribbons used in chapter 4 were annealed at 650°C for 2 h and quenched to room temperature. The samples from chapter 6 were annealed at 900°C for 2 days and quenched to room temperature.

3.5. Diffraction experiments

Diffraction is scattering of radiation from a periodic lattice, giving rise to interference. The interference pattern, or diffraction pattern, can be used to determine the crystal lattice. Each diffraction peak is determined by the scattering by one or multiple lattice planes, given by indices (hkl). In these planes, the electrons (for X-rays) or nuclei and magnetic moments (for neutrons) of atoms n are the source of the scattering. The sum of all the waves scattered by these atoms is called the structure factor F[9]:

$$F_{hkl} = \sum_{n=0}^{n=N} f_n exp(2\pi i(hx_n + ky_n + lz_n)). \tag{3.1}$$

When the scattering objects are not localized in one point, the sum in the structure factor can be replaced by an integral over the volume V:

$$F_{hkl} = \iiint_V \rho_{xyz} exp(2\pi i(h\frac{x}{a} + k\frac{y}{b} + l\frac{z}{c}))\, da\, db\, dc. \tag{3.2}$$

where x, y and z are the fractional coordinates of a unit cell with cell axes a, b and c. Now the electron density can be written as a Fourier series

$$\rho_{xyz} = \frac{1}{V} \sum_h \sum_k \sum_l exp(2\pi i(h\frac{x}{a} + k\frac{y}{b} + l\frac{z}{c})). \tag{3.3}$$

The structure factors were obtained by Rietveld refinement[10] using the FullProf software[11].

3.5.1. Electron density plots

By using the structure factors as coefficients in a Fourier synthesis (performed by VESTA[12] using a .fos file as input), the electron density can be reconstructed. The resolution of the electron density is given by the number of structure factors used. Due to the phase problem, only the real part of the structure factor is measured, because the intensity of a reflection is given by $I = |F^2|$. The imaginary part (due to the phase) is calculated using the crystallographic model and is determined by the atomic positions. The magnitude of the structure factor is partly determined by the atomic form factor f, which is a scalar derived from an isotropic electron density distribution. Because the electron density distribution in real solids is generally anisotropic, the atomic form factor should depend on hkl. This is reflected in the fact that the observed and calculated intensities for different reflections always show some deviations. By using the observed intensities to describe the real part of the structure factor, the anisotropic nature of the atomic form factor (which does not contribute to the imaginary part) can be taken into account. To measure changes in electron density as a function of temperature, the electron density at two different temperatures can be reconstructed and the difference can be plotted. In this way, all common features are removed and the electron density difference can be visualized. This is complicated by the fact that thermal motion of atoms changes the diffracted intensity. High temperature increases the thermal diffuse scattering and decrease the intensity at the diffraction peaks. However, the total scattered intensity should remain constant (neglecting any absorption). This means that the sum of the structure factors over all lattice planes should be a constant. This constant was used as a scale factor in the electron density plots, considering that the integral over the electron density is equal to the number of electrons in the unit cell.

3.5.2. X-ray powder diffraction

Room temperature X-ray diffraction (XRD) measurements were performed on a PANalytical X'Pert PRO diffractometer. The temperature-dependent X-ray diffraction experiments were performed in 0.5 mm capillaries at the BM1A beamline at the ESRF using a wavelength of 0.68884 Å and a PILATUS2M area detector. Temperature control was achieved using a liquid nitrogen cryostream.

3.5.3. Neutron powder diffraction

Neutron diffraction measurements were performed on the new neutron powder diffractometer PEARL of the TU Delft[13]. Data were collected at 78 and 405 K using the (533) reflection of the germanium monochromator (λ = 1.665Å). The sample was loaded under

argon in a 6 mm diameter air-tight vanadium container (0.15 mm thickness). Cooling was achieved using a stream of liquid nitrogen and a heat gun was used for heating. The sample was measured for 10 min per temperature step. The data treatment consisted of a correction for the detection efficiency.

3.6. Magnetization measurements

Magnetization measurements were carried out in a superconducting quantum interference device (SQUID) magnetometer (Quantum Design MPMS 5XL). Samples were put in a gelatin capsule, which was mounted in a transparent plastic straw. Temperature dependent measurements were performed with a sweep rate of 2 K/min. High-temperature magnetization measurements were performed in a VersaLab vibrating sample magnetometer (VSM) with an oven function. This instrument can heat a sample from 350 to 1000 K. The sample was in contact with a resistive heater and fixed by thermal paste.

3.7. X-ray Absorption Spectroscopy

Apart from scattering experiments, absorption experiments can also provide valuable information about the electronic structure of a material. By tuning the energy of the X-rays to an absorption edge, the attenuated beam can be measured[14]. In general, the intensity is measured as a function of energy. X-ray absorption fine structure spectroscopy (XAFS) uses high-energy photons to excite electrons from a core level to an excited state. The energy of the various core levels ($1s$, $2s$ etc.) is known and at a synchrotron facility the energy can be tuned to an absorption edge. Because core levels are not influenced by the chemical environment of the material, the excited state is of particular interest. For compounds containing Fe, the interesting excitations are a dipolar coupling from $1s$ to $4p$ and a quadrupolar coupling between $1s$ and $4d$ orbitals.

The XAFS spectrum can be divided into two regions: XANES (X-ray Absorption Near Edge Structure) and EXAFS (Extended X-ray Absorption Fine Structure). The XANES region is determined by the absorption edge and depends on the final energy state, which is highly influenced by the oxidation state. The EXAFS region is found at higher energies and here the excited electrons have additional kinetic energy. This causes oscillations due to scattering. By analyzing the oscillations, the local environment (electron density around the absorbing atom) can be probed. Because in the Fe_2P structure Fe and Mn preferentially occupy different lattice sites, the electron density around the two lattice sites can selectively be probed.

The experiments were performed on powders with particle sizes between 20 and 40 μm that were mixed with boron nitride to control the attenuation and pressed into pellets. The measurements were performed in transmission mode. Boron nitride secures the structural properties of the material without influencing the measurement. A nitrogen cryostream was used to cool and heat the samples with a temperature control within 2 K. For better statistics, two absorption spectra were recorded at each temperature.

All XAFS spectra were analyzed with the Athena and Artemis software packages[15]. In reducing the data, the same set of parameters was utilized for each absorption edge. For the Fourier transform at the Fe edge, k values between 2 and 13 $Å^{-1}$ were used;

for the Mn edge, k values between 2 and 12 Å^{-1} were used since higher k values were inaccessible due to an overlap with the Fe-edge. In fitting the data, an Einstein model was used to calculate the static disorder. To simulate the XAFS data, 6 scattering paths were used per temperature, based on the experimental lattice parameters. This accounts for 96% of the partial occupations of crystallographic sites and occupational disorder. The coordinates of the atoms were taken from neutron diffraction data. The energy shift between the experimental data and the fit was determined per measurement and the disorder and amplitude were fitted for the whole temperature range. A total of 5 parameters were used out of 13 independent points per measurement for the first shell of Fe. For Mn there are 11 independent points for the first shell. All fits were performed in k space.

References

[1] H. Davy. 'The Bakerian Lecture: An Account of Some New Analytical Researches on the Nature of Certain Bodies, Particularly the Alkalies, Phosphorus, Sulphur, Carbonaceous Matter, and the Acids Hitherto Undecompounded; With Some General Observations on Chemical Theory.' Phil. Trans. Roy. Soc. volume A 97, p. 71 (1809).

[2] D. Pavuna. 'Production of metallic glass ribbons by the chill-block melt-spinning technique in stabilized laboratory conditions.' J. Mater. Sci. volume 16, pp. 2419–2433 (1981).

[3] Z. Altounian, E. Batalla, J. O. Strom-Olsen and J. L. Walter. 'The influence of oxygen and other impurities on the crystallization of $NiZr_2$ and related metallic glasses.' J. Appl. Phys. volume 61, pp. 149–155 (1987).

[4] C. Pfleiderer. 'Superconducting phases of f-electron compounds.' Rev. Mod. Phys. volume 81, pp. 1551–1624 (2009).

[5] H. V. Lohneysen. 'Fermi-liquid instabilities at magnetic quantum phase transitions.' Rev. Mod. Phys. volume 79, pp. 1016–1069 (2007).

[6] K. A. Gschneidner Jr. 'Metals, alloys and compounds high purities do make a difference!' J. Alloy Compd. volume 193, pp. 1–6 (1993).

[7] R. W. Cahn. Physical metallurgy. North Holland (1983).

[8] N. T. Trung. 'First-order phase transitions and the giant magnetocaloric effect.' Doctoral thesis (2010).

[9] C. Hammond. The basics of crystallography and diffraction. Oxford University Press (2009).

[10] H. M. Rietveld. 'A profile refinement method for nuclear and magnetic structures.' J. Appl. Cryst. volume 2, p. 65 (1969).

[11] J. Rodríguez-Carvajal. Satellite Meeting on Powder Diffraction of the XV IUCr Congress volume 127 (1990).

[12] K. Momma and F. Izumi. 'VESTA 3 for three-dimensional visualization of crystal, volumetric and morphology data.' J. Appl. Crystallogr. volume 44, pp. 1272–1276 (2011).

[13] L. van Eijck, L. D. Cussen, G. J. Sykora et al. 'Design and performance of a novel neutron powder diffractometer: PEARL at TU Delft.' J. Appl. Cryst. volume 49, pp. 1398–1401 (2016).

[14] G. Bunker. Introduction to XAFS. Cambridge University Press (2010).

[15] B. Ravel and M. Newville. 'ATHENA, ARTEMIS, HEPHAESTUS: data analysis for X-ray absorption spectroscopy using IFEFFIT.' J. Synchrotron. Rad. volume 12, pp. 537–541 (2005).

4

Mg_3Cd-based materials

4.1. Introduction

Compounds based on Mn and Ga can form a large variety of phases. The high spin polarization and moderate transition temperatures qualify them as good candidates for magnetocaloric materials. The structural and magnetic properties of Mg_3Cd-type $(Mn_{1-x}Fe_x)_{3-\delta}Ga$ have been studied.

The Mg_3Cd-type crystal structure is composed of two layers, each containing three magnetic atoms (Mn, Fe or Ni) and one non-magnetic atom (Ga, In, Ge or Sn) in a hexagonal unit cell[1]. The magnetic atoms are arranged in a triangle in each layer, with a non-magnetic atom above/below the center of this triangle in the other layer, as shown in Figure 4.1. This phase is commonly referred to as the ϵ phase. The hexagonal phase is metastable and will form in a temperature range between a high-temperature cubic and a low-temperature tetragonal phase[2], and can be stabilized by quenching.

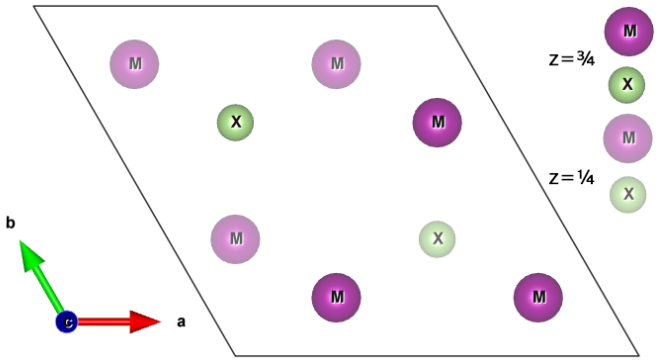

Figure 4.1: Unit cell of the Mg_3Cd type crystal structure. Three magnetic atoms (M) are arranged in a triangle in one layer and a non-magnetic atom (X) in the center of the triangle, in the alternate layer indicated by shading.

The first magnetic study on the ϵ phase in the Mn-Ga system showed a magnetic moment of about 3.0 μ_B for Mn[3]. The magnetic moments are arranged in a triangular antiferromagnetic configuration[4]. The triangular arrangement has been described using an Ising model with the spins confined to the basal plane[5]. It gives rise to a complex antiferromagnetic structure that can be described by a combination of three magnetic sublattices, oriented at an angle of 120°. This often leads to exotic properties such as spin ice, multicritical phenomena, and noncollinear ordering[6].

Most of the triangular spin systems investigated so far are insulators, while Mn_3Ga is an example of a metallic system. This makes this system very interesting. Additionally, there is a sudden change in magnetization that coincides with a distortion of the lattice at T_d. A hexagonal-to-orthorhombic reduction in symmetry has been reported to take place at the distortion temperature T_d, but no evidence has been presented to confirm this[7,8]. Using high-resolution X-ray diffraction, we will show that the symmetry is actually reduced to monoclinic. Such a behavior is highly uncommon, $Tb_3Ag_4Sn_4$ is the only other example of such a transition[9].

The outline of the remainder of the paper is as follows, first, the phase stability of the ϵ phase is investigated in the presence of Fe and Si substitutions. To explore if the crystallographic transition persists, the magnetic properties of $(Mn,Fe)_{3-\delta}Ga$ and $Mn_{3-\delta}(Ga,Si)$ are reported. Finally, the origin of the crystallographic distortion is investigated using both X-ray and neutron diffraction techniques.

4.2. Experimental

Mn chips (99,9%), Ga pieces (99,99%) and Fe granules (99,98%) were melted in the arc melting furnace described in section 3.2. An extra 2 wt.% Mn was added to account for evaporation losses; the evaporation varied between 1.75 and 2.25 wt.%, based on the change in mass. The obtained buttons were turned three times and subsequently melt spun to facilitate the phase formation. Combined evaporation losses from melt spinning and annealing result in a maximum deviation of 0.2 wt.% from the nominal stoichiometry. The melt-spun ribbons were ductile, which is an indication that the ribbons are amorphous.

To find the transition temperatures of the tetragonal, hexagonal and cubic phases, differential thermal analysis (DTA) was performed on a Perkin–Elmer MAS-5800 instrument with a heating/cooling rate of 10°C/min and a nitrogen flow rate of 50 ml/min. We observe transitions around 550, 600 and 700°C. These preliminary samples were sealed in quartz ampoules, filled with Ar, and quenched in water. It was found that below 600°C the tetragonal phase is stable and above 700°C the cubic phase is formed. Apart from these phases, no other phases were observed after annealing at 450, 650 and 750°C for 8 h. All subsequent samples were annealed under argon at 650°C for 2 h and quenched in water.

The diffraction experiments and magnetization measurements are described in section 3.5 and 3.6 respectively.

4.3. Results and discussion

4.3.1. Phase stability of $(Mn,Fe)_{2.9}(Ga,Si)$

According to the binary Mn-Ga and Fe-Ga phase diagrams[2], the ϵ phase is stable only with an excess of Ga. To verify whether this is also the case for melt-spun samples, a stoichiometric Mn_3Ga sample was made. The sample shows single ϵ phase and contains 74.8 ± 0.2 at.% Mn based on the experimental evaporation, EDX measurements show a concentration of 75 ± 2 at.% Mn. All other samples were made with a stoichiometry of 2.9:1 to facilitate the solid solution formation of Mn_3Ga and Fe_3Ga. The results on the phase stability of the samples is summarized in Figure 4.2. Above 25% Si substitution, the cubic $Mn_3(Si,Ga)$ phase is formed. The fraction of the α-Fe phase was found to be strongly dependent on the annealing time. For that reason, the 8 h annealing time of the preliminary samples was reduced to 2 h to reduce the formation of the α-Fe phase. In samples containing Si, between 10% and 25% α-Fe was formed. It is expected that the phase stability window of 600 to 700°C varies with composition. This complicates the phase formation of the ϵ phase and can lead to a non-uniform distribution of second phases.

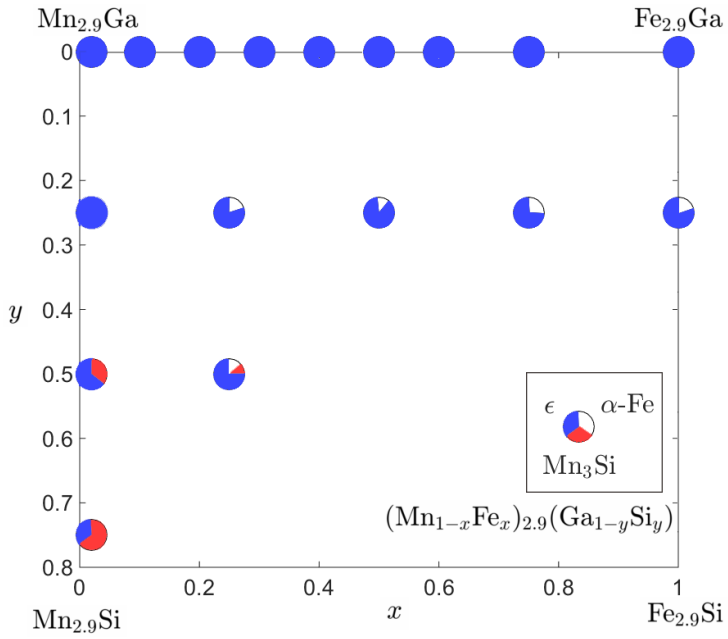

Figure 4.2: Quaternary phase diagram of $(Mn,Fe)_{2.9}X$. The ϵ phase is shown in blue, the cubic Mn_3Si phase is shown in red and the α-Fe phase is shown in white. All samples were annealed at 650°C for 2h and characterized by XRD at room temperature.

4.3.2. Magnetic properties of $(Mn_{1-x}Fe_x)_{2.9}Ga$

The crystallographic distortion of the hexagonal structure is characterized by an increase in magnetization below room temperature shown in Figure 4.3 for $x = 0$. For $x = 0.3$ the antiferromagnetic regime is shifted to lower temperatures and shows two magnetic transitions. For $x = 0.4$ there is a paramagnetic to ferromagnetic transition at 230 K and a ferro- to antiferromagnetic transition at 150 K, where the Mn moments start to align antiferromagnetically. Because the Mn moments cannot compensate each other due to the stoichiometry and the alignment with the applied field, the magnetization increases with decreasing temperature. The same behavior is observed for $x = 0.5$ but is absent for $x = 0.6$.

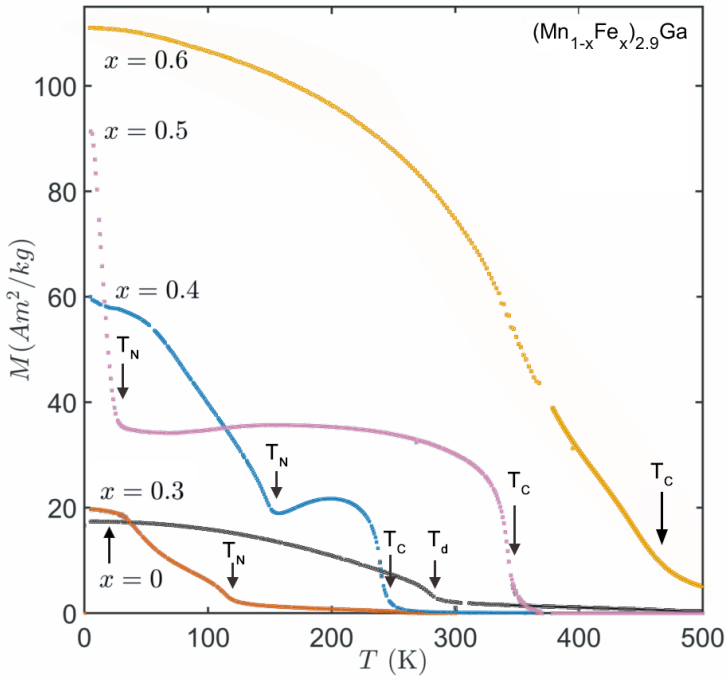

Figure 4.3: Magnetization as a function of temperature under an applied field of 1 T for $(Mn_{1-x}Fe_x)_{2.9}Ga$. For $x = 0$, the composition is $Mn_{2.95}Ga$.

Figure 4.4 shows the magnetization measurements for selected values of x. A very low magnetization is measured for $x = 0.1$, comparable to the magnetization found in Mn_3Ge and Mn_3Sn. In addition, the ferromagnetic component at low fields is absent for $0 < x < 0.3$ and the magnetization increases linearly with applied fields up to 15 T[10]. The antiferro- to ferromagnetic transition at $x = 0.3$ gives rise to a larger saturation magnetization. To determine the saturation magnetization for all samples, a Langevin function with added linear component was used to fit the data. Above the Néel temperature, the sample shows Curie-Weiss behavior ($\chi = M/H = C/(T + \theta_{CW})$, which is characterized by a linear response of M to the applied field H.

For high Mn concentrations, antiferromagnetic interactions dominate and decrease

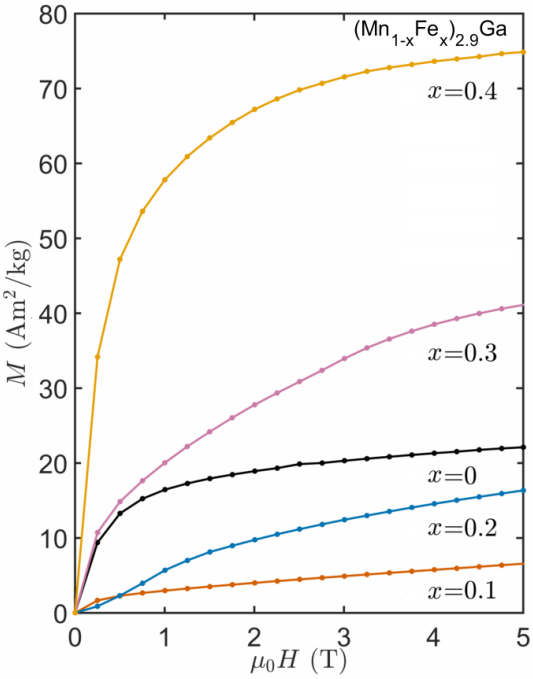

Figure 4.4: Magnetization curves of $(Mn_{1-x}Fe_x)_{2.9}Ga$ and fits (Langevin function with added linear component) as a function of applied field at 5 K.

Table 4.1: Magnetic transition temperatures T_N and T_C extrapolated to zero-field and saturation magnetization of $(Mn,Fe)_{2.9}Ga$

compound	T_N (K)	T_C (K)	M (Am^2/kg)	(μ_B / atom)
$Mn_{2.9}Ga$	470		20.0	0.27
$(Mn_{0.9}Fe_{0.1})_{2.9}Ga$	418		2.7	0.04
$(Mn_{0.8}Fe_{0.2})_{2.9}Ga$	320		10.7	0.15
$(Mn_{0.7}Fe_{0.3})_{2.9}Ga$	251	50	24.9	0.34
$(Mn_{0.6}Fe_{0.4})_{2.9}Ga$	156	230	76.5	1.05
$(Mn_{0.5}Fe_{0.5})_{2.9}Ga$	50	345	93.6	1.29
$(Mn_{0.4}Fe_{0.6})_{2.9}Ga$		420	111.8	1.54
$(Mn_{0.25}Fe_{0.75})_{2.9}Ga$		530	139.1	1.91
$Fe_{2.9}Ga$		720	145.7	2.02

linearly as a function of x. The same trend is observed for Fe. In the region where T_N and T_C are equal, there is a small deviation from the linear behavior, as shown in Figure 4.5. This is in line with the findings on $(Mn_{1-x}Fe_x)_3Ge$[11] and $(Mn_{1-x}Fe_x)_3Sn$[12].

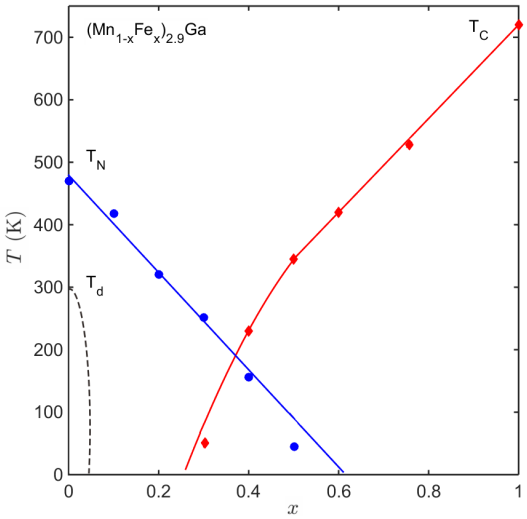

Figure 4.5: Critical temperatures of $(Mn_{1-x}Fe_x)_{2.9}Ga$ as a function of x. The antiferromagnetic interaction of $Mn_{2.9}Ga$ is weakened for increasing x as the ferromagnetism of $Fe_{2.9}Ga$ gradually sets in. The crossover with $T_N \approx T_C \approx 190$ K is around x=0.37.

Using the experimentally determined saturation magnetization, the magnetic behavior of $(Mn,Fe)_{2.9}Ga$ is shown in Figure 4.6. The line between $x = 0$ and $x = 1$ is shown as a guide to the eye. Three regions can be distinguished: I is characterized by the crystallographic distortion, II is dominated by antiferromagnetic interactions, III is dominated by ferromagnetic interactions. In region II, the magnetization is relatively low. This can be explained by considering a triangular antiferromagnetic arrangement by magnetic moments of unequal magnitude. In region III, the magnetic moments rotate in favor of a ferromagnetic arrangement. The fact that the saturation magnetization does not exceed the value at $x = 1$ indicates that Mn always couples antiferromagnetically, because the magnetic moment of Mn is larger compared to Fe. From the saturation magnetization of $Fe_{2.9}Ga$, the calculated magnetic moment per Fe atom is 2.0 μ_B. The magnetic properties are summarized in Table 4.1. The entropy change under an applied field change of 0-1 T for the sample with $x = 0$ is 0.1 J/K kg.

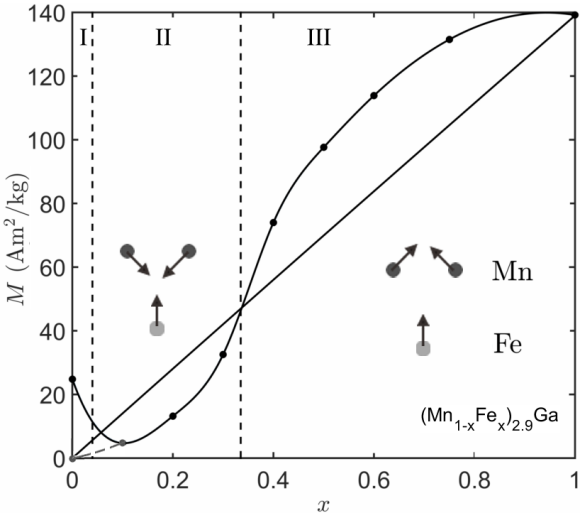

Figure 4.6: The experimentally determined saturation magnetization measured as a function of x at 5 K. The datapoints are connected by a cubic spline interpolant as a guide to the eye. In region I, the magnetization is nonzero below T_d and zero above T_d. In region II, below the diagonal line, T_d is absent and the AF Mn sublattice couples AF to the Fe sublattice. In region III, above the diagonal line, the AF Mn sublattice couples FM to the Fe sublattice.

4.3.3. Magnetic properties of $Mn_{2.95}$(Ga,Si)

When substituting Si for Ga, the crystallographic distortion temperature decreases. To keep the transition temperature around room temperature, a ratio of 2.95:1 was chosen. The unit cell of $Mn_{2.95}Ga_{1-y}Si_y$ reduces isotropically for $y \leqslant 0.25$ but expands at higher values of y, which suggests that Si first substitutes Ga but for higher Si concentrations it enters the lattice interstitially. At the same time, for $y > 0.25$, the cubic Mn_3(Ga,Si) phase is formed as a second phase. This second phase is also antiferromagnetic and complicates the analysis of the magnetic properties. The ferromagnetic contribution at low temperatures however persists and the transition broadens. The structural properties are summarized in Table 4.2.

Table 4.2: Distortion temperatures, magnetization at 5 K in a field of 1 T (Am^2/kg), lattice parameters a and c and the volume fraction of cubic 2^{nd} phases f_{second} of $(Mn_{1-x}Fe_x)_{2.95}$(Ga,Si).

compound	T_d (K)	a (Å)	c (Å)	f_{second} (%)
$Mn_{2.95}Ga$	230	5.405	4.350	<1
$Mn_{2.95}Ga_{0.75}Si_{0.25}$	220	5.350	4.313	<1
$Mn_{2.95}Ga_{0.5}Si_{0.5}$	190	5.358	4.320	35
$Mn_{2.95}Ga_{0.25}Si_{0.75}$	150	5.370	4.330	65

4.3.4. Magnetoelastic transition of $Mn_{2.9}Ga$

To study the origin of the crystallographic distortion, high-resolution X-ray diffraction measurements were performed as a function of temperature. In order to study a sample that has both a steep increase in magnetization and could be measured well below T_d using liquid nitrogen, the $Mn_{2.9}Ga$ sample was selected.

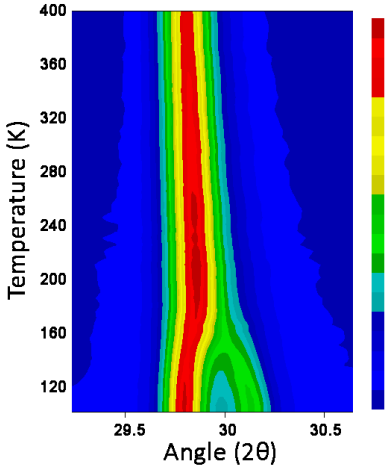

Figure 4.7: Powder X-ray diffraction intensity of the {220} peak of $Mn_{2.9}Ga$ as a function of temperature (K)

When cooling the sample down, the {220} peak gradually splits, indicating a second-order phase transition as shown in Figure 4.7. This is supported by DSC measurements that did not detect any latent heat. It seems that the unit cell gradually changes and the resulting symmetry is expected to be a subgroup of the $P6_3/mmc$ spacegroup. By reducing the symmetry to P1, one can change all unit cell parameters and find the parameter relevant for the phase transition. It was found that a deviation of the 120 degree angle results in the observed peak splitting, resulting in a hexagonal to monoclinic phase transition. The corresponding space group is $P2_1/m$, which is a subgroup of the orthorhombic space group Cmcm, a supercell of the original unit cell[13]. The distortion lifts the equivalence of the Mn atoms, they are no longer related by a threefold axis and occupy three crystallographic positions, as summarized in Table 4.3.

Table 4.3: Refined X-ray diffraction data of $Mn_{2.9}Ga$. The atomic coordinates of Mn1 / Mn2 / Mn3 are split for the monoclinic phase.

	100 K	200 K
S.G.	$P2_1/m$	$P6_3/mmc$
a (Å)	5.304(5)	5.349(7)
b (Å)	4.304(6)	5.349(7)
c (Å)	5.364(3)	4.309(1)
β	119.68(7)	120
Mn	(x,$\frac{1}{4}$,z) (2e)	(x,2x,$\frac{1}{4}$) (6h)
x	$\frac{1}{3}$ / $\frac{5}{6}$ / $\frac{5}{6}$	$\frac{1}{6}$
z	$\frac{1}{6}$ / $\frac{1}{6}$ / $\frac{2}{3}$	$\frac{1}{4}$
Ga	(x,$\frac{1}{4}$,z) (2e)	($\frac{1}{3}$,$\frac{2}{3}$,$\frac{3}{4}$) (2d)
x	$\frac{1}{3}$	$\frac{1}{3}$
z	$\frac{2}{3}$	$\frac{3}{4}$
B_{ov} (Å^2)	0.33	0.61
R_p	4.42	5.85
R_{wp}	3.92	6.51

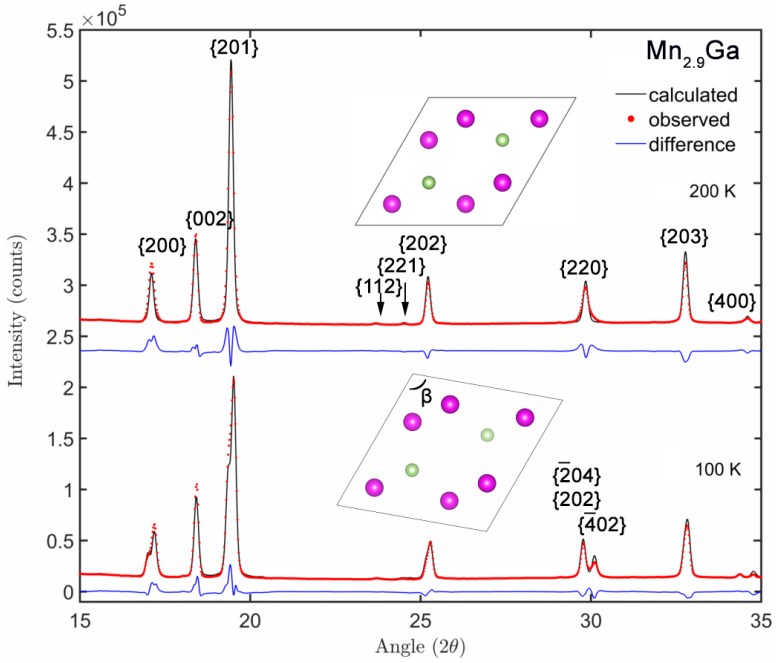

Figure 4.8: X-ray diffraction data of $Mn_{2.9}Ga$ at a temperature of 200 K (above the distortion temperature) and at 100 K (below the distortion temperature).

Table 4.4: Refined neutron diffraction data of Mn_3Ga. The atomic coordinates obtained by XRD were used as input. The magnetic moment vector is decomposed into three components along the crystallographic axes (M_a, M_b, M_c). The individual moments of Mn are 2.6 μ_B for 78 K and 2.2 μ_B for 405 K.

	78 K	405 K
a (Å)	5.420(9)	5.391(8)
b (Å)	4.333(8)	5.391(8)
c (Å)	5.313(3)	4.348(3)
β	119.18(7)	120
Mn1	(1.6 / 0 / -1.4)	(2.2 / 0 / 0)
Mn2	(0 / 0 / -2.6)	(0 / 2.2 / 0)
Mn3	(-2.6 / 0 / 0)	(-2.2 / -2.2 / 0)
B_{ov} (Å^2)	0.07	1.45
R_p	4.62	4.91
R_{wp}	6.65	6.28

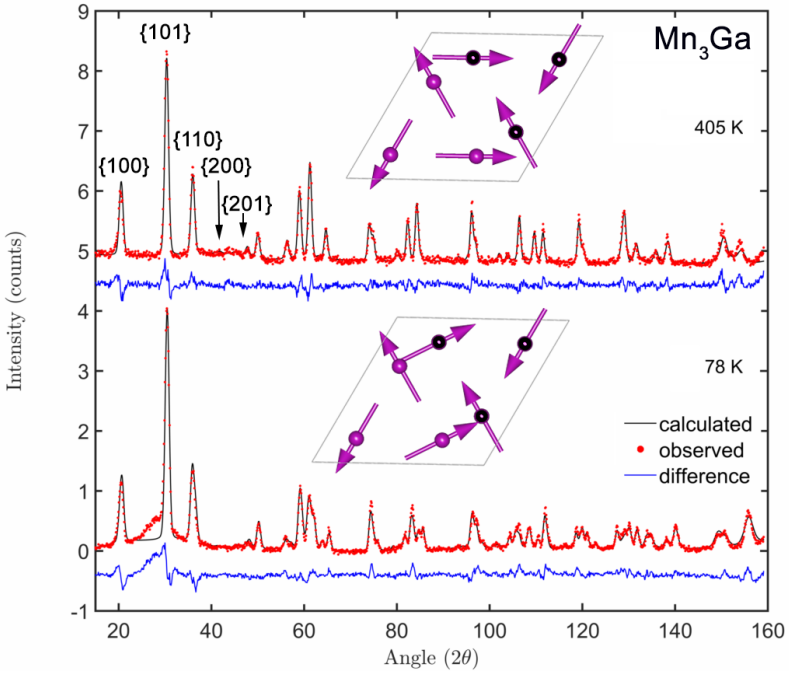

Figure 4.9: Neutron diffraction data of Mn_3Ga above and below the distortion temperature. The black and purple atoms lie in different planes. The moment orientations are obtained from Rietveld refinement.

By refining the unit cell dimensions, a good fit was obtained with the experimental powder diffraction pattern, shown in Figure 7.8. Due to the distortion, both the in-plane angle as well as the cell lengths change, while the out-of-plane cell length is hardly affected. Refinement of the atomic positions of Mn did not improve the fit. The distortion of the triangular lattice of the Mn atoms will affect the magnetic properties. Therefore, neutron diffraction experiments were performed on Mn_3Ga below and above T_d. Above the distortion temperature, the obtained triangular antiferromagnetic arrangement confirms earlier findings[4]. Below the distortion temperature, the degeneracy of the Mn atoms is lifted and the magnetic moments were refined individually. The atomic positions obtained from the XRD refinement were used as input. An increased background was measured at low temperatures around the {101} peak, which was attributed to the sample environment. The results are shown in Figure 4.9.

Above the distortion temperature, the magnetic moments of Mn lie along the crystallographic directions, resulting in a zero net moment. The same holds for the other layer, which has inverse chirality. The chiral solution, where both layers have the same chirality, gives a higher intensity at the {100} peak and was discarded. Below the distortion temperature, the net moment cannot point out of plane, as this would be visible in the {200} and {201} peaks. The rotation of one local moment can reproduce the observed intensity, keeping the magnitude of the moments constant, as shown in Figure 4.9. This rotation partially cancels the moment in the [00-1] direction, leaving a net moment in the [101] direction. The result of the refinements of the neutron diffraction data are summarized in Table 4.4.

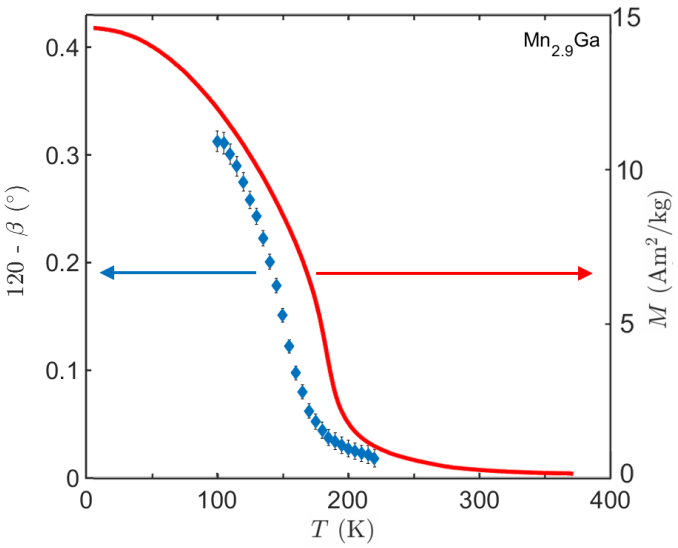

Figure 4.10: Distortion of the β angle (left) and magnetization (right) of $Mn_{2.9}Ga$ measured at 1 T, as a function of temperature. The magnetization and the distortion are correlated, but don't coincide due to the broadening by the applied field and the temperature control.

By measuring the magnetization of the sample as a function of temperature, we can see that the magnetization and monoclinic angle are indeed correlated, as can be seen in Figure 4.10. The temperature difference can be attributed to the shift due to the applied magnetic field and the temperature control. There is clearly a correlation between the deviation of the 120 degree angle and the rotation of the magnetic moment of the Mn atoms. It is now also clear how the stoichiometry affects the magnetization. In the ferromagnetic state, three magnetic domains are expected to form where the in-plane moments generate a net domain magnetization along three principal directions. If one would apply an in-plane magnetic field or shear force on a single crystal, the material would acquire a ferromagnetic component in-plane with a maximum magnetization of about 70 Am^2/kg. This is a domain reorientation and is expected to be a reversible process. Generally, phase transitions involving a change in symmetry are of first-order. However, in this case, the monoclinic symmetry can be described as a subgroup of the hexagonal symmetry, which allow a continuous change of the 120 degree angle.

4.4. Conclusions

$(Mn_{1-x}Fe_x)_{2.9}Ga$ is shown to form an ϵ single phase after quenching from a temperature between 600 and 700°C. Stoichiometric Mn_3Ga is shown to form using melt spinning, indicating that off-stoichiometry is not an intrinsic property of the material, but is rather an experimental complication. When Si is introduced, the temperature window of phase stability is expected to vary and second and third phases are observed. Magnetization measurements show a low magnetization for Mn rich samples, consistent with an antiferromagnetic arrangement of three magnetic sublattices. When substituting one Fe atom for Mn, a ferromagnetic component is introduced while lowering the Néel temperature. At $x = 0.37$ the Fe and Mn sublattices couple ferromagnetically and the material becomes ferromagnetic. We attribute the crystallographic distortion in $Mn_{3-\delta}Ga$ to a rotation of the three antiferromagnetic sublattices below room temperature. This reduces the symmetry from hexagonal to monoclinic via a second-order phase transition. The distortion results in a rotation of one of the magnetic moments in-plane. This effect is linked to the magnetic lattice site, because replacing Ga with Si retains the distortion. This study shows that there is a coupling between the magnetic structure and crystal structure in this material. With the application of a magnetic field, a reversible magnetization change can be realized around room temperature.

References

[1] K. Kanematsu and H. Takahashi. 'Magnetization and X-Ray studies on $(Fe_{1-x}Ni_x)_3Ge$ and $(Fe_{1-x}Ni_x)_{3.4}Ge$.' J. Phys. Soc. Jpn. volume 53, pp. 2376–2380 (1984).

[2] K. Minakuchi, R. Y. Umetsu, I. Kiyohito and K. Ryosuke. 'Phase equilibria in the Mn-rich portion of Mn–Ga binary system.' J. Alloys Compd. volume 537, pp. 332–337 (2012).

[3] I. Tsuboya and M. Sugihara. 'The magnetic properties of ϵ phase in Mn-Ga system.' J. Phys. Soc. Jpn. volume 143, p. 143 (1963).

[4] E. Krén and G. Kádár. 'Neutron diffraction study of Mn_3Ga.' Solid State Commun. volume 8, pp. 1653–1655 (1970).

[5] D. H. Lee, J. D. Joannapoulos and J. W. Negele. 'Discrete-Symmetry Breaking and Novel Critical Phenomena in an Antiferromagnetic Planar (XY) Model in Two Dimensions.' Phys. Rev. Lett. volume 52, pp. 433–436 (1984).

[6] A. P. Ramirez. 'Strongly geometrically frustrated magnets.' Annu. Rev. Mater. Sci. volume 24, p. 453 (1994).

[7] H. Niida, T. Hori and Y. Nakagawa. 'Magnetic properties and crystal distortion of hexagonal Mn_3Ga.' J. Phys. Soc. Jpn. volume 52, pp. 1512–1514 (1982).

[8] H. Kurt, K. Rode, H. Tokuc et al. 'Exchange-biased magnetic tunnel junctions with antiferromagnetic ϵ-Mn_3Ga.' Appl. Phys. Lett. volume 101, p. 232402 (2012).

[9] D. H. Ryan, J. M. Cadogan, C. J. Voyer et al. 'Using neutron diffraction and mossbauer spectroscopy to study magnetic ordering in the $R_3T_4Sn_4$ family of compounds.' Mod. Phys. Lett. B volume 24, pp. 1–28 (2010).

[10] H. Niida, T. Hori, Y. Yamaguchi and Y. Nakagawa. 'Crystal distortion and weak ferromagnetism of $Mn_{3+d}Ga_{1-x}Ge_x$ alloys.' J. of Appl. Phys. volume 73, p. 5692 (1993).

[11] T. Hori, Y. Yamaguchi and Y. Nagakawa. 'Antiferromagnetic to ferromagnetic transition of hexagonal $(Mn_{1-x}Fe_x)_3Ge$.' J. Magn. Magn. Mater. pp. 2045–2046 (1992).

[12] T. Hori, H. Niida, Y. Yamaguchi et al. 'Antiferromagnetic to ferromagnetic transition of DO_{19} type $(Mn_{1-x}Fe_x)_3Sn_{1-\delta}$.' J. Magn. Magn. Mater. pp. 159–160 (1990).

[13] M. I. Aroyo, A. Kirov, C. Capillas et al. 'Bilbao Crystallographic Server II: Representations of crystallographic point groups and space groups.' Acta Cryst. volume A62, pp. 115–128 (2006).

5

Origin of the first-order phase transition in Fe_2P-based materials

5.1. Introduction

Materials such as Mn(As,Sb)[1], La(Fe,Si)$_{13}$ and its hydrides[2], (Mn,Fe)$_2$(P,X) where X = As[3], Ge[4], Si[5] , MnCoGe[6] or Gd$_5$(Ge,Si)$_4$[7] show a first-order magnetic transition, resulting in entropy changes in low field that are one order of magnitude larger than for second-order transitions. Of these, the most promising magnetocaloric materials are the Fe_2P-based[8] and La(Fe,Si)$_{13}$-based[2] compounds. They show a large isothermal entropy change and adiabatic temperature change in low magnetic fields in combination with a small thermal hysteresis. In addition, they both exhibit a magneto-elastic transition, in which the atomic arrangement changes in a much more subtle way compared to the full crystallographic phase transition encountered in other first-order materials.

Density Functional Theory (DFT) calculations predict a distinct change in electronic structure and magnetic moments across the magneto-elastic transition in Fe_2P-based materials[9–11], shown in Figure 5.1. In particular, Fe atoms on the 3f site, shown in Figure 5.2 display a partially quenched magnetic moment in the paramagnetic state. A recent DFT study on La(Fe,Si)$_{13}$-based compounds also indicates, for the paramagnetic state "the possibility of stable quenched Fe-moments"[12]. We therefore propose that competition between bond formation and moment formation lies at the basis of this first-order magnetoelastic transition as it involves the same 3d electrons.

In order to experimentally verify that this mechanism is relevant in MCE materials, one may probe changes in electron density around the Fe atoms. The $MnFe_{0.95}P_{0.582}Si_{0.34}B_{0.078}$[13] compound was chosen for its sharp first-order transition and an Fe/Mn ratio close to 1:1, which allows one to distinguish the high and low moment sites. For La(Fe,Si)$_{13}$, experimental verification is more difficult as all moments are Fe moments. We use X-ray Absorption Fine Structure (XAFS) and high-resolution X-Ray Diffraction (XRD) to investigate the electron density. Extended X-ray Absorption Fine Structure (EXAFS), is sensitive to the local electronic environment around

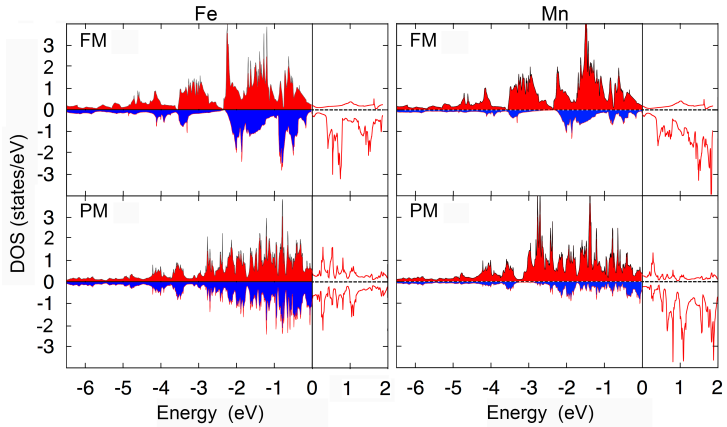

Figure 5.1: Partial density of states of Fe and Mn in the ferromagnetic (FM) and the paramagnetic (PM) state of $MnFeP_{0.67}Si_{0.33}$ obtained by DFT calculations. The energy scale is plotted with respect to the Fermi energy. In the ferromagnetic state there is a majority of spin-up electrons (red) compared to the spin-down electrons (blue), which contribute to the itinerant magnetism. Both in the PM and FM states there is a large majority of spin up electrons (red). The corresponding magnetic moments are 1.45 μ_B (FM), 0.67 μ_B (PM) for Fe and 2.93 μ_B (FM), 2.87 μ_B (PM) for Mn.

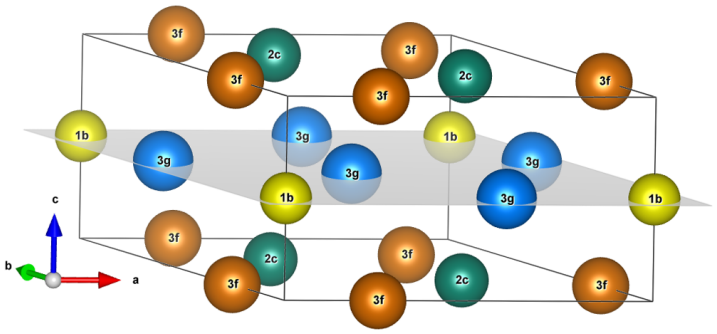

Figure 5.2: Unit cell of the hexagonal Fe_2P structure (space group $P\bar{6}2m$) showing the Wyckoff positions and the layered structure. The $1b$ and $2c$ positions are occupied by the nonmetal P and Si atoms and the $3f$ and $3g$ positions are occupied by metal Fe and Mn atoms.

a particular type of atom. By applying a Fourier transform to the EXAFS signal, 1D radial electron density plots can be obtained. By measuring below and above the critical temperature, changes in this radial distribution of the electron density are detected. To characterize these changes also in 3D, we created charge density maps from high-resolution XRD measurements above and below the critical temperature. Additionally, we performed new DFT calculations for a compound with a stoichiometry close to the experimental value.

5.2. Experimental

Preparation of the sample is described in a previous paper [13]. Details on the X-ray absorption and powder diffraction experiments can be found in chapter 3. The density functional theory calculations on $MnFeP_{0.67}Si_{0.33}$ were done using Vienna ab-initio simulation package (VASP) [14] using generalized gradient approximation by Perdew, Burke and Enrzerhof (GGA-PBE) [15]. Frozen core charges were represented with pseudopotentials of the Vanderbilt form [16] utilizing the projector augmented wave (PAW) [17] framework. For all the atoms, PAW data sets were used with frozen $1s$, $2s$, $2p$ and $3s$ core state for Mn and for Fe an additional $3p$ state was frozen. For Si and P $1s$, $2s$ and $2p$ core state was kept frozen. The Brillouin-zone integration was done using a Gamma centered k-point mesh of $6 \times 6 \times 6$ k points in the irreducible part of the Brillouin zone. The cutoff energy of the augmentation function was taken as 400 eV and, for smearing, the Methfessel-Paxton scheme was used with a smearing width of 0.1 eV. The calculations were relaxed using force and energy convergence criteria of 0.001 eV/Å and 10^{-7} eV respectively. The lattice parameters and the atomic positions within the unit cell of $MnFeP_{0.67}Si_{0.33}$ in ferromagnetic and paramagnetic states were independently relaxed until the convergence criteria were achieved. The obtained values for ferromagnetic and paramagnetic lattice parameters were a_{FM} = 6.13 Å, c_{FM} = 3.27 Å and a_{PM} = 5.94 Å, c_{PM} = 3.42 Å. The c/a ratios of both phases are in agreement with the experimentally determined ratios. For the FM phase, these ratios are 0.536 (XRD) and 0.533 (DFT) and for the PM state these are 0.564 (XRD) and 0.576 (DFT). For the charge density plots, the unit cell parameters and atomic positions obtained by Rietveld refinement of the XRD data were used. To model the paramagnetic state, a $2 \times 2 \times 2$ supercell was created with alternative direction of magnetic moments within the XY plane. This was energetically more stable compared to previous calculations [11,18]. The magnetic moments of weakly magnetic Fe atoms decrease from 1.45 μ_B in the FM state to 0.67 μ_B in the PM state, where the strongly magnetic Mn atoms retain the moment from 2.93 μ_B (FM) to 2.87 μ_B (PM) during the phase transition.

5.3. Results and discussion

The absorption spectra measured at different temperatures are shown in Figure 5.3 and have been split into XANES (X-Ray Absorption Near Edge Spectrum) and EXAFS (Extended X-Ray Absorption Fine Structure) parts.

The XANES part does not show a significant change across the ferromagnetic transition, so we expect no valence changes for Fe and Mn. The absorption edge most closely resembles the absorption edge of pure Fe and Mn metals. In the EXAFS region, there is a significant change in the Fe fine structure, in contrast to the Mn fine structure. The fine structure data in k space and its Fourier transform are shown in Figure 5.4.

For the Fe signal, the fit is in good agreement with the data, but around 8 $Å^{-1}$ there are some deviations. The signal around this region is probably due to contributions of the next nearest neighbors, which were not fitted. The fit of the Mn signal is slightly more off due to the higher standard deviation of this signal compared to the signal from Fe. There is a systematic shift in the main peak, which indicates that there is a systematic difference between the atomic positions measured with X-ray diffraction and the

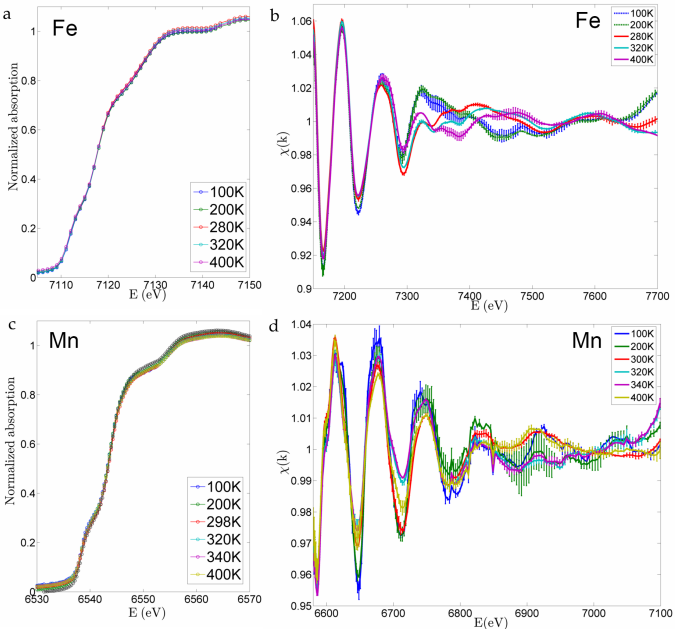

Figure 5.3: Normalized absorption of the Fe (a,b) and Mn (c,d) edges in $MnFe_{0.95}P_{0.582}Si_{0.34}B_{0.078}$. The XANES region is displayed on the left and the EXAFS region is displayed on the right.

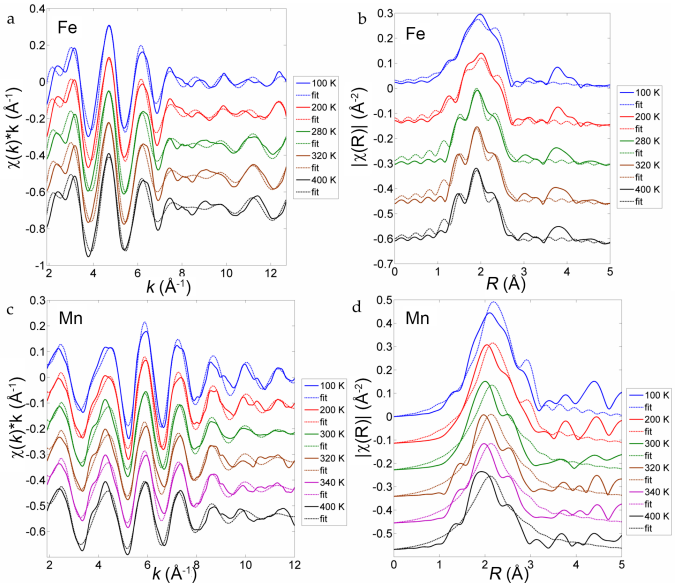

Figure 5.4: Fits of Fe (a,b) and Mn (c,d) of $MnFe_{0.95}P_{0.582}Si_{0.34}B_{0.078}$ in k and R space. The signals below 1.3 Å are artifacts of the Fourier transformation. The distances have an offset with respect to the physical distances due to the phase shift caused by the scattering of the photo-electron.

Table 5.1: Results of the fits to the Fe and Mn edge data. S_0^2 is the passive electron reduction factor. The E_0 values are relative to the edge inflection point. The * indicates parameters that are common to both data sets in the fit. The σ^2 is the thermal mean-square variation in atomic distance. The $\theta_{E,X-Fe}$ was set to a fixed value.

	Fe-edge	Mn-edge
S_0^2	0.457 ± 0.014	0.490 ± 0.012
E_0 (eV) 100 K	6.92 ± 0.81	1.75 ± 0.84
E_0 (eV) 400 K	7.77 ± 0.60	1.59 ± 0.94
$\theta_{E,X-P}$	477 ± 321	474 ± 442
$\theta_{E,X-Si}$	475 ± 185	340 ± 142
$\theta_{E,X-Fe}$	387 (fixed)	$291^* \pm 39$
$\theta_{E,X-Mn}$	$291^* \pm 39$	177 ± 23.7

data obtained with XAFS. It appears that the interatomic distances in the Mn layer are reduced compared to the X-ray data.

In Figure 5.5 the Fourier transform of the Fe EXAFS data, measured below and above T_C, are shown as a function of the distance from the central absorber atom. As X-rays solely interact with electrons, this represents the radial distribution of the electron density around Fe. Two electron density peaks around 2.3 and 2.7 Å are caused by atoms occupying the $1b/2c$ and $3f/3g$ positions. We know from neutron diffraction that the $1b$ and $2c$ sites are occupied by P and Si atoms, while Fe and Mn atoms occupy the $3f$ and $3g$ positions[19]. A small shift in peak position reflects the difference in interatomic distances for the FM and the PM phase. In addition to the main two peaks, another peak is visible located at smaller distances. This peak is located at distances of 1.8 and 1.6 Å above and below T_C, respectively. Therefore our simulations based on the atomic positions obtained from neutron diffraction clearly reproduce the $1b/2c$ and $3f/3g$ peaks, but are not able to reproduce the first peak. Note that the position of the Fe absorption edge is not affected, which excludes a change in Fe valence. The EXAFS results are a first indication that the Fe electron charge is indeed redistributed locally across the transition.

While the radially averaged electron density is probed by element-specific EXAFS, it can be probed in 3D by high-resolution X-ray diffraction. The diffractograms measured at different temperatures including the Rietveld refinement are shown in Figure 5.6. The refinement parameters are shown in Table 5.2. The inverse Fourier transform of the structure factors, as determined by Rietveld refinement[20], can be used to experimentally obtain a 3D electron density plot, analogous to that obtained from DFT calculations.

As we are interested in the changes in electron density related to the magnetoelastic phase transition, we subtract the electron densities of the ferromagnetic from the paramagnetic phase. The difference maps are shown in Figure 5.7, in particular for the electron density difference within the Fe layer. Figure 5.7(a) was generated by subtracting the measured electron density at 150 K from the measured electron density at 450 K. Figures 5.7(b) and 5.7(c) are both derived from first principle DFT calculations. In the case of Figure 5.7(b) the Fe atoms are allowed to relax to the experimentally determined equilibrium position, while for 5.7(c) the relative coordinates of the atoms were kept

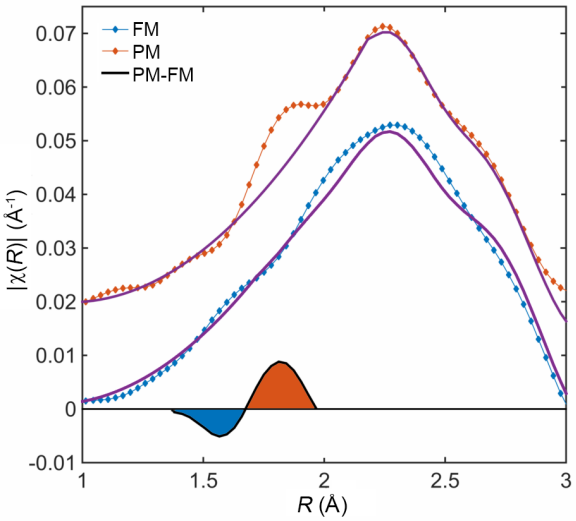

Figure 5.5: Radial plots of the electron density around the Fe atom as derived from EXAFS in the FM phase (measured at 100 K) and in the PM phase (measured at 400 K). The PM curves have been shifted vertically by 0.02 $Å^{-1}$ for clarity. The connected points represent the measured data and the solid lines are fits to the data based on the atomic positions using an isotropic model. The solid line represents the difference between the FM and PM phase.

fixed.

The calculated experimentally determined electron density difference plots show very similar features around Fe. The redistribution of electron density is asymmetric due to a shift of the atomic position of Fe across the transition. Both the experimental shift and the lattice parameters were used as input for the calculations in order to reliably compare the two density plots. Similar calculations are performed to generate Figure 5.7(c), however keeping the relative atomic positions constant[18]. It shows that electrons shift from a d_{xz} to a d_{z^2} orbital when crossing the magnetoelastic transition from the paramagnetic to the ferromagnetic state, respectively. In Figure 5.7(b) one lobe of the d_{z^2} orbital is obscured and the two lobes of the d_{xz} orbital on either side of the atom are smeared out.

The asymmetry that is observed in the direct subtraction can be reduced if one switches to radial coordinates. By taking the atomic coordinates of Fe and summing up all charges found at certain distance intervals we generate radial electron density plots from the experimental XRD data at 150 and 350 K. This radial electron-density plot reproduces the unidentified peak and peak position that were observed in Figure 5.5 at short distance and the difference plot shows the same behavior as found in the EXAFS results. XRD and EXAFS thus corroborate the earlier statement that was based on DFT calculations; in these materials moment formation competes with bonding.

In the PM phase, a covalent bond is formed between Fe and the P/Si atoms, leading to a decrease in the a/b and an increase in the c lattice parameters. This can be understood from a magnetic and a chemical viewpoint. The Fe atoms only carry a sizable magnetic

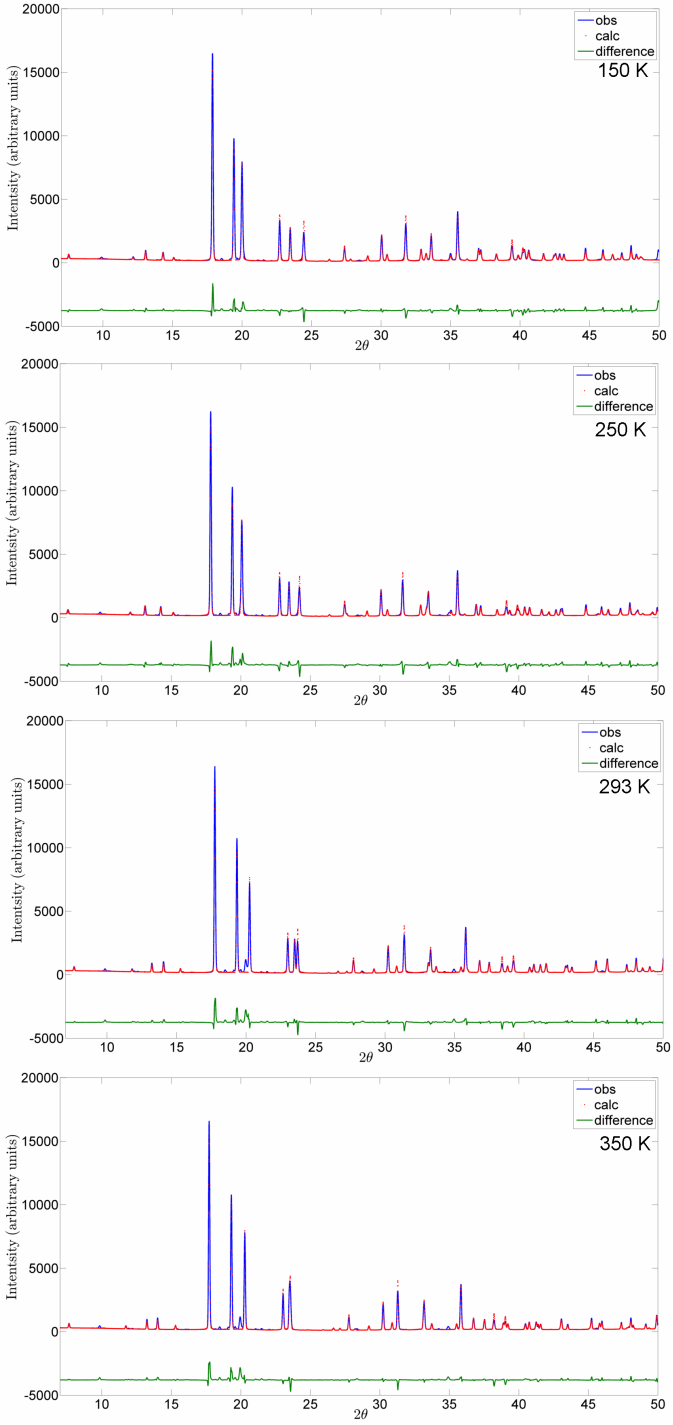

Figure 5.6: High-resolution X-ray diffraction of $MnFe_{0.95}P_{0.582}Si_{0.34}B_{0.078}$ at 150 (a), 250 (b), 293 (c) and 350 K (d). The fits (calc) and residuals (difference) are also given.

Table 5.2: List of XRD fitting parameters obtained from high-resolution synchrotron powder XRD. The following values are given: the positional parameter x for the $3f$, $3g$ positions, the a and c axis in Å with uncertainty, the R factors for each angle interval and χ^2 values.

	150 K	250 K	293 K	350 K
$3f$ x	0.25404(26)	0.25457(33)	0.25270(27)	0.25245(24)
$3g$ x	0.59721(37)	0.59647(42)	0.59260(35)	0.59215(31)
a (Å)	6.126(48)	6.105(41)	6.049(74)	6.039(59)
c (Å)	3.288(94)	3.319(19)	3.389(23)	3.409(47)
2θ	5-50 7-57	5-50 7-57	5-50 7-57	5-50 7-57
R_p	9.05 9.54	10.8 11.7	8.44 8.13	7.42 9.01
R_{wp}	12.7 13.1	15.6 17.0	12.0 12.0	10.7 13.4
χ^2	7.01 6.5	10.2 12.8	6.17 5.01	4.67 5.78

moment when the exchange interaction between the Mn layers is sufficiently strong. However, as the exchange interaction is overcome by magnetic fluctuations, we find that the ferromagnetic transition is associated with a remarkably strong reduction of the Fe magnetic moment. In other words, the ferromagnetic exchange field exerted by the Mn moments on the Fe positions stabilizes the Fe magnetic moments, while as soon as it vanishes, the Fe valence electrons rather bond with neighboring P/Si, which destabilizes the moments.

The experimental correspondence with the DFT calculations indicates that the metalloid atoms play a crucial role in providing metastable behavior in these compounds, namely that the electrons can switch between metallic and covalent character. Metalloids share properties of both metals and nonmetals. This was recognized early on by Linus Pauling in his influential work on the chemical bond by looking at the crystal structures of C, Si, Ge and Sn[21]. Carbon, being small, has a large overlap of its orbitals and prefers to make directional, localized bonds. For Si and Ge the overlap decreases and for Sn the overlap is so small that above room temperature, the diamond structure is transformed into a metallic phase. The metastability in bonding due to metalloids is the basis for many first-order magnetostructural transitions, and for this system it is found to be responsible for the magnetoelastic isostructural transition.

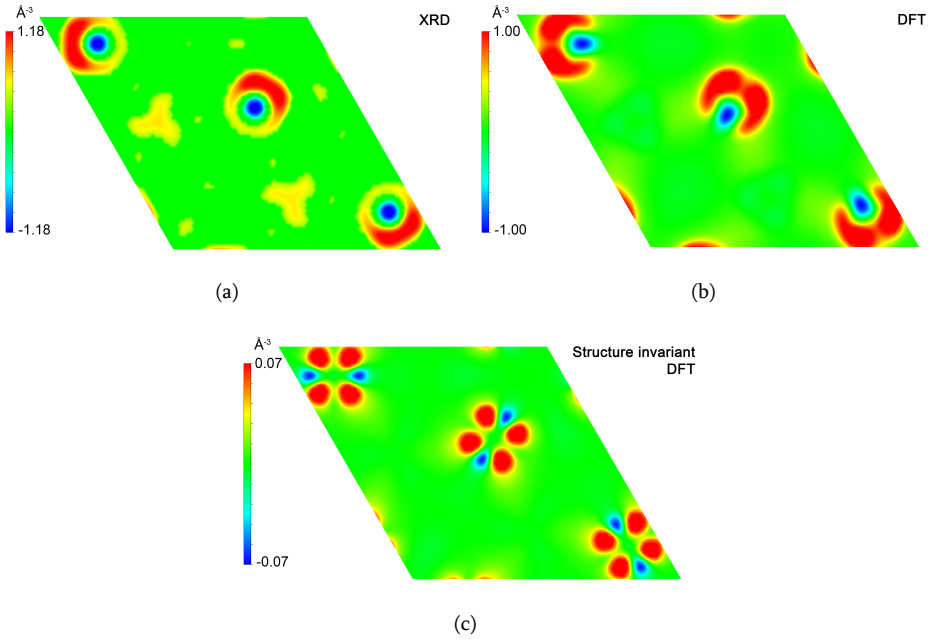

Figure 5.7: Charge difference map across the ferromagnetic transition from high-resolution X-ray powder diffraction at 350 and 150 K (a) and DFT calculations (b) and (c). The unit cells were uniformly scaled when subtracting the phases. Structure invariant indicates that the relative Fe coordinate was fixed. The difference between the FM state (blue) and the PM state (red) is shown.

5.4. Conclusions

In summary, we observe a redistribution in the electron density around the Fe atom when going from the FM to the PM phase by XAFS and XRD measurements. This results to a formation of covalent bonds that strongly reduce the magnetic moment of Fe. Therefore, $mixedmagnetism$ is demonstrated to be the underlying phenomenon responsible for the first-order magnetic phase transition and the excellent magnetocaloric properties found in Fe_2P-based compounds.

Besides the magnetic (order-disorder) and crystallographic changes, there is also a distinct electronic contribution to the entropy change, which allows tapping into all three entropy reservoirs (lattice, magnetic and electronic contributions) of the material. Apart from the early work on FeRh[22], the electronic contribution to the magnetocaloric effect is usually disregarded or considered to be negligible. The electronic contribution arises from the redistribution of electrons and a change in density of states at the Fermi level, of which Fe shows the largest contribution.

This effectively boosts the magnetocaloric effect, as the entropy change relies not only on Mn layer moment alignment, but also on the change in the electron density of states in the Fe layer. Its relevance becomes strikingly clear when one considers the temperature scales of each contribution. Applied magnetic fields of a few tesla correspond to a few kelvin, while the ordering of the magnetic moments is characterized by the $T_C \approx 300$ K. The structural contribution is characterized by the Debye temperature for lattice vibrations $\Theta_D \approx 420$ K for Fe_2P. The electronic contribution, however, can reach up to the Fermi temperature $T_F \approx 10{,}000$ K.

The reduction in the Fe moment on only one crystallographic site in MnFe(P,Si) and $La(Fe,Si)_{13}$ indicates that both materials behave similarly. Now that the origin of the giant magnetocaloric effect for these materials is established, we propose two minimal requirements for possible candidate materials with further improved magnetocaloric properties. These materials should contain a metalloid element and a late $3d$ transition metal that occupies two different crystallographic positions. These ingredients provide the necessary tools to design mixed magnets for cooling applications with improved efficiencies.

References

[1] H. Wada and Y. Tanabe. 'Giant magnetocaloric effect of $MnAs_{1-x}Sb_x$.' Appl. Phys. Let. volume 79, pp. 3302–3304 (2001).

[2] A. Fujita, S. Fujieda, Y. Hasegawa and K. Fukamichi. 'Itinerant-electron metamagnetic transition and large magnetocaloric effects in $LaFe_{13-x}Si_x$ compounds and their hydrides.' Phys. Rev. B volume 67, p. 104416 (2003).

[3] E. Brück, M. Ilyn, A. M. Tishin and O. Tegus. 'Magnetocaloric effects in $MnFeP_{1-x}As_x$-based compounds.' J. Magn. Magn. Mater. volume 290-291, pp. 8–13 (2005).

[4] N. T. Trung, Z. Q. Ou, T. J. Gortenmulder et al. 'Tunable thermal hysteresis in MnFe(P,Ge) compounds.' Appl. Phys. Lett. volume 94, p. 102513 (2009).

[5] O. Tegus, E. Brück, K. H. J. Buschow and F. R. de Boer. 'Transition-metal-based magnetic refrigerants for room-temperature applications.' Nature volume 415, pp. 150–152 (2002).

[6] N. T. Trung, L. Zhang, L. Caron et al. 'Giant magnetocaloric effects by tailoring the phase transitions.' Appl. Phys. Lett. volume 96, p. 172504 (2010).

[7] K. A. Gschneidner Jr. and V. K. Pecharsky. 'Giant magnetocaloric effect in $Gd_5Si_2Ge_2$.' Phys. Rev. Lett. volume 78, pp. 4494–4497 (1997).

[8] L. Lundgren, G. Tarmohamed, O. Beckman et al. 'First Order Magnetic Phase Transition in Fe_2P.' Phys. Scripta volume 17, pp. 39–48 (1978).

[9] H. Yamada and K. Terao. 'First-order transition of Fe_2P and anti-metamagnetic transition.' Phase Transitions volume 75, pp. 231–242 (2002).

[10] E. K. Delczeg-Czirjak, L. Delczeg, M. P. J. Punkkinen et al. 'Ab initio study of structural and magnetic properties of Si-doped Fe_2P.' Phys. Rev. B volume 82, p. 085103 (2010).

[11] N. H. Dung, Z. Q. Ou, L. Caron et al. 'Mixed Magnetism for Refrigeration and Energy Conversion.' Adv. Energy Mater. volume 1, pp. 1215–1219 (2011).

[12] M. E. Gruner, W. Keune, B. R. Cuenya et al. 'Element-Resolved Thermodynamics of Magnetocaloric $LaFe_{13-x}Si_x$.' Phys. Rev. Lett. volume 114, p. 057202 (2015).

[13] F. Guillou, G. Porcari, H. Yibole et al. 'Taming the first-order transition in giant magnetocaloric materials.' Adv. Mater. volume 27, pp. 2671–2675 (2014).

[14] G. Kresse and J. Hafner. 'Ab initio molecular dynamics for liquid metals.' Phys. Rev. B volume 47, p. 558 (1993).

[15] J. P. Perdew, K. Burke and M. Ernzerhof. 'Generalized Gradient Approximation Made Simple.' Phys. Rev. Lett. volume 77, p. 3865 (1996).

[16] D. Vanderbilt. 'Soft self-consistent pseudopotentials in a generalized eigenvalue formalism.' Phys. Rev. B volume 41, p. 7892 (1990).

[17] G. Kresse and J. Joubert. 'From ultrasoft pseudopotentials to the projector augmented-wave method.' Phys. Rev. B volume 59, p. 1758 (1999).

[18] The scale of Fig. 5.7(c) is one order of magnitude lower compared to the scale of Fig. 5.7(b). This difference can be attributed to the use of the experimental crystal parameters. .

[19] X. F. Miao, L. Caron, Z. Gercsi et al. 'Thermal-history dependent magnetoelastic transition in $(Mn,Fe)_2(P,Si)$.' Appl. Phys. Lett. volume 107, p. 042403 (2015).

[20] H. M. Rietveld. 'A profile refinement method for nuclear and magnetic structures.' J. of Appl. Crystallogr. volume 2, pp. 65–71 (1969).

[21] L. C. Pauling. In 'The nature of the chemical bond,' Cornell University Press (1960).

[22] M. P. Annaorazov, S. A. Nikitin, A. L. Tyurin et al. 'Anomalously high entropy change in FeRh alloy.' J. Appl. Phys. volume 79, pp. 1689–1695 (1996).

6

Comparison between first and second-order phase transition in Fe_2P-based materials

6.1. Introduction

In the last two decades, research into magnetocaloric materials has intensified due to the discovery of so-called giant magnetocaloric materials[1]. These materials have a magnetocaloric effect that is enhanced by the presence of latent heat. For Fe_2P-based materials, the nature of the ferromagnetic transition is reflected by a discontinuous change in unit-cell parameters[2,3]. When the lattice parameters change discontinuously, the magnetic transition is of first order (FOMT) and is generally accompanied by latent heat and hysteresis. When there is no jump in lattice parameters, the magnetic transition is of second order (SOMT), without latent heat or hysteresis.

The transition can be modeled considering the change in Gibbs free energy across the magnetic phase transition, as described in the Landau model[4,5]:

$$\Delta G = \frac{\alpha}{2}M^2 + \frac{\beta}{4}M^4 + \frac{\gamma}{6}M^6 - \mu_0 H M \tag{6.1}$$

where the magnetization M is the order parameter and $\mu_0 H$ the applied magnetic field. Parameter $\alpha = \alpha_0(T - T_0)$ depends on temperature with respect to a characteristic temperature T_0 and α_0, β, γ are constants ($\alpha_0, \gamma > 0$). Minimization with respect to the magnetization M ($\partial \Delta G / \partial M = 0$) leads to the equation of state:

$$\alpha + \beta M^2 + \gamma M^4 = \frac{\mu_0 H}{M} \tag{6.2}$$

where β can be positive or negative, leading to a second-order or first-order magnetic transition, respectively. For $\beta = 0$ (critical point), the transition is on the verge of a first-order magnetic transition. Material properties in the vicinity of such a critical

point (CPT) are of great interest for applications. For near room temperature cooling, materials with a small negative value for β show a sizeable latent heat in combination with a low hysteresis. For heat conversion, materials with a small positive value for β show a steep magnetization increase without latent heat.

To study the difference between strongly first-order, second-order and near-critical behavior, we studied three samples with high-resolution powder X-ray diffraction (PXRD) as a function of temperature. The critical temperature and the character of the phase transition can easily be tuned by balancing the Mn/Fe and P/Si ratios[6]. The addition of B, N and C causes a tempering of the first-order transition and leads to a simultaneous increase in T_C[7–9].

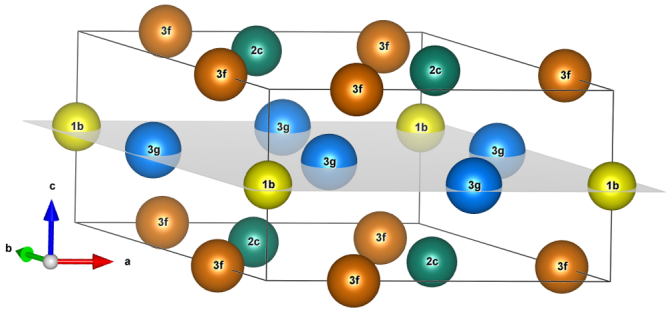

Figure 6.1: Unit cell of the hexagonal Fe_2P structure (space group $P\bar{6}2m$) showing the Wyckoff positions and the layered structure. The $1b$ and $2c$ positions are occupied by the nonmetal P and Si atoms and the $3f$ and $3g$ positions are occupied by metal Fe and Mn atoms.

As shown in Figure 6.1, Fe_2P has a hexagonal unit cell (space group $P\bar{6}2m$) containing two layers of atoms. Both layers contain magnetic and nonmagnetic atoms. For $(Mn,Fe)_2(P,Si)$ there is a site preference for Mn on the $3g$ position, Fe prefers the $3f$ position and Si prefers the $2c$ position[10]. While the nonmagnetic atoms occupy fixed relative positions, the magnetic atoms have a translational degree of freedom, which has not been systematically investigated so far.

In chapter 5, the origin of the giant magnetocaloric effect in Fe_2P-based materials was experimentally established. The basis for this effect lies in a special kind of two sublattice magnetism where both weak and strong magnetism is present and is distinctly different from conventional two-sublattice magnetism[11]. One of these sublattices is governed by strong magnetism ($3g$ site) and the size of the moments is relatively stable across the transition. The other sublattice is governed by weak magnetism ($3f$ site) and the moment is strongly reduced in magnitude. This phenomenon was named $mixedmagnetism$[12]. The strong reduction of the moment of one sublattice in the paramagnetic state was linked to the strengthening of a covalent bond between magnetic and metalloid atoms, which was made clear by investigating electron density difference plots. This study uses the electron density plots to characterize the difference in behavior between first- and second-order magnetic transitions.

6.2. Experimental

Preparation of the samples is described in a previous paper[8]. High-resolution powder X-ray diffraction (PXRD) was performed at the ESRF at beamline BM01A using a wavelength of 0.68884 Å. The temperature control was achieved using a N_2 Cryostream. The temperature range between 100 and 400 K was covered in temperature steps of 5 K. The samples were put in 0.5 mm capillaries and spun. Rietveld refinement was performed using the FullProf software[14]. The electron density was calculated by VESTA[15] and processed in Matlab.

6.3. Results

Three samples were measured as a function of temperature. The first sample with composition $MnFeP_{0.6}Si_{0.4}$ shows a FOMT, the second sample with composition $Mn_{1.7}Fe_{0.3}P_{0.4}Si_{0.6}$ shows a SOMT and the third sample with composition $MnFeP_{0.595}Si_{0.33}B_{0.075}$ shows a CPT. The temperature evolution of the {300}, {211} and {002} PXRD reflections upon heating is shown in Figure 6.2. The effect of temperature on the unit cell is directly visible. For the sample with a FOMT, the a and c-axes change discontinuously and there is a region of phase coexistence. For the sample with a SOMT, the unit cell changes continuously and no region of phase coexistence is detected. For the CPT sample, a rapid continuous change of the lattice parameters is present at T_C. The value of T_C is 275, 205 and 295 K for the FOMT, SOMT and CPT, respectively.

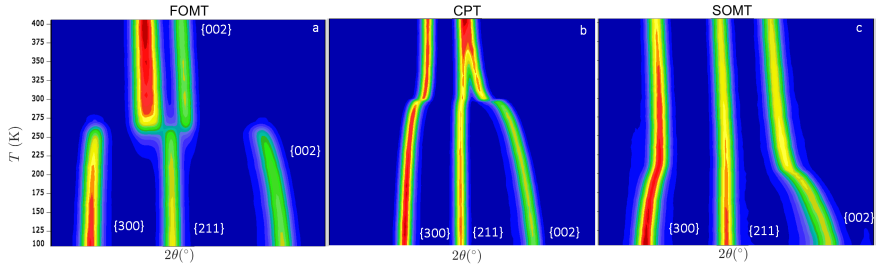

Figure 6.2: Intensity of scattering angle (2θ) as a function of temperature (T) for $MnFeP_{0.6}Si_{0.4}$ (a), $MnFeP_{0.595}Si_{0.33}B_{0.075}$ (b) and $Mn_{1.7}Fe_{0.3}P_{0.4}Si_{0.6}$ (c). The {300}, {211} and {002} peaks are shown as the material crosses the transition upon heating.

While inspection of the raw data gives qualitative information, quantitative information can be extracted using Rietveld refinement. The refinement is shown in Figure 6.3 and the parameters are listed in Table 6.1. To directly compare the materials, which have different unit-cell volumes and transition temperatures, the normalized data are plotted in Figure 6.4. Far below T_C, both the a and c axis show a similar temperature dependence. When the temperature is close to T_C, there is an abrupt change for the FOMT and a more gradual change for the SOMT sample. At the same time, the FOMT shows a much larger overall change in lattice parameters compared to the SOMT.

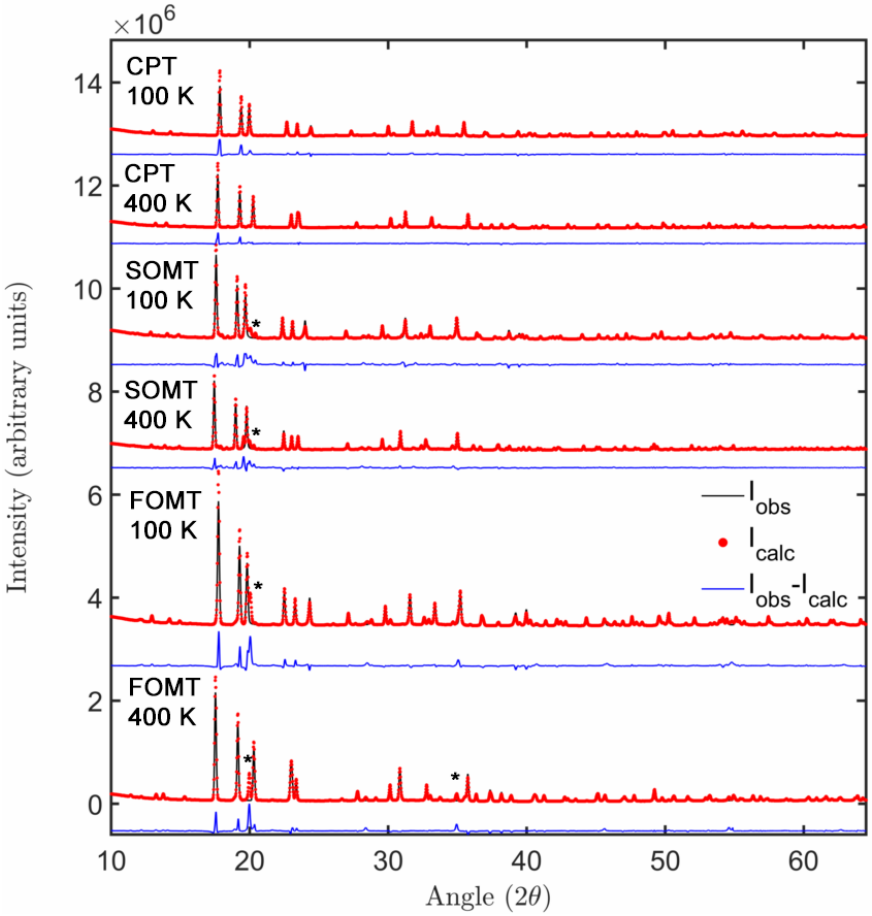

Figure 6.3: X-ray powder diffraction patterns and refinements of $MnFeP_{0.6}Si_{0.4}$ (FOMT), $MnFeP_{0.595}Si_{0.33}B_{0.075}$ (CPT) and $Mn_{1.7}Fe_{0.3}P_{0.4}Si_{0.6}$ (SOMT) measured at 100 K and 400 K. The asterisk denotes the $(Fe,Mn)_3Si$ second phase, which was not included in the refinement.

Table 6.1: Refined X-ray diffraction data at 400 K. The $3g$ positions are located at (x,0,$\frac{1}{2}$) and the $3f$ positions at (x,0,0).

	FOMT	CPT	SOMT
S.G.	P $\bar{6}$ 2 m	P $\bar{6}$ 2 m	P $\bar{6}$ 2 m
a (Å)	5.969(9)	5.984(7)	6.126(0)
c (Å)	3.458(7)	3.375(3)	3.384(1)
x_g	0.589(3)	0.592(9)	0.592(6)
x_f	0.248(8)	0.251(7)	0.252(8)
B_{3g} (Å^2)	1.089(5)	0.824(3)	1.119(0)
B_{3f} (Å^2)	0.930(9)	0.860(9)	1.055(1)
B_{2c} (Å^2)	1.066(6)	0.398(9)	0.807(0)
B_{1b} (Å^2)	1.083(3)	0.938(2)	1.444(3)
R_p	5.56	3.93	6.87
R_{wp}	5.76	4.04	5.26

Table 6.2: Relative change in cell parameters (%) across the transition with respect to the low temperature (ferromagnetic) phase ($\frac{\Delta n}{n_{FM}}$). For the SOMT sample, the properties at $T_C - 20K$ were used.

composition		a	c	c/a	V	x_f	x_g
$MnFeP_{0.6}Si_{0.4}$	FOMT	-2.64	4.98	10.7	-0.06	-2.41	-1.21
$MnFeP_{0.595}Si_{0.33}B_{0.075}$	CPT	-0.64	0.93	2.01	-0.05	-0.36	-0.62
$Mn_{1.7}Fe_{0.3}P_{0.4}Si_{0.6}$	SOMT	-0.21	0.43	0.73	-0.13	-0.20	-0.60

The total change across the transition for all three samples is summarized in Table 6.2. Although the lattice parameters change significantly, the change in cell volume is limited. This absence of a volume change is beneficial for applications, as it reduces hysteresis and cracking during cycling. Surprisingly, the internal parameters x_f and x_g show the same sign as the change in the a axis.

The temperature dependence of the internal coordinates x_f and x_g are shown in Figure 6.5. The uncertainty in the phase coexistence region of the FOMT sample is significantly larger due to the phase fraction. For that reason, the coordinate values have been omitted in this region.

From the atomic coordinates and lattice parameters, the interatomic distances can be calculated in the FM and PM states for all samples. The distances are given in Table 6.3.

Table 6.3: Interatomic distances in the FM and PM state (Å).

	FOMT		CPT		SOMT	
	FM	PM	FM	PM	FM	PM
$3f-1b$	2.271	2.287	2.253	2.259	2.281	2.288
$3f-2c$	2.305	2.270	2.289	2.280	2.330	2.323
$3g-1b$	2.480	2.494	2.445	2.444	2.492	2.490
$3g-2c$	2.480	2.453	2.470	2.470	2.501	2.505
$3f-3g$	2.643	2.650	2.644	2.641	2.673	2.674

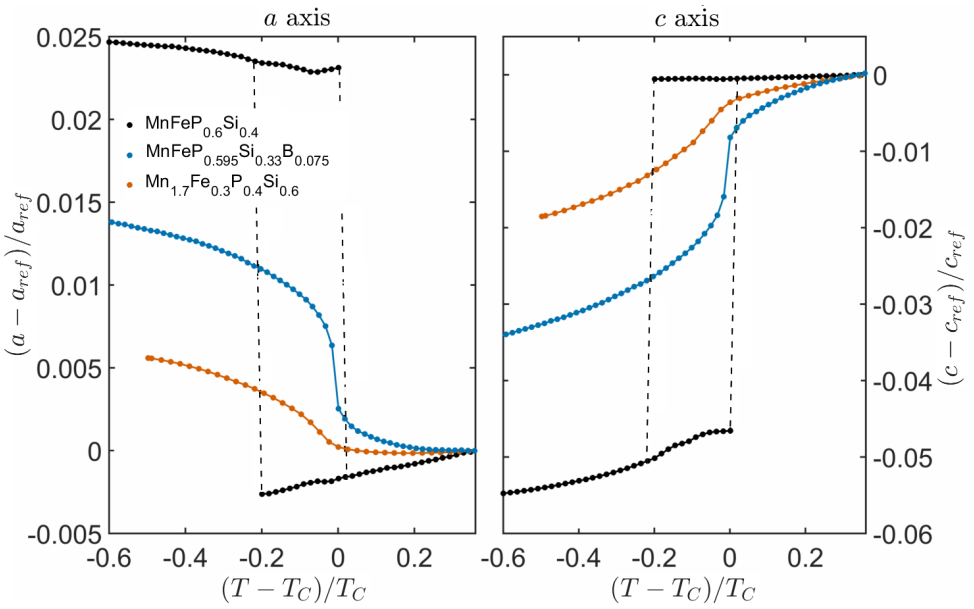

Figure 6.4: Reduced lattice parameters as a function of reduced temperature, where $x_{ref} = x(T_C + 100\ \text{K})$. T_C values are 275, 205 and 295 K for the FOMT, SOMT and CPT respectively.

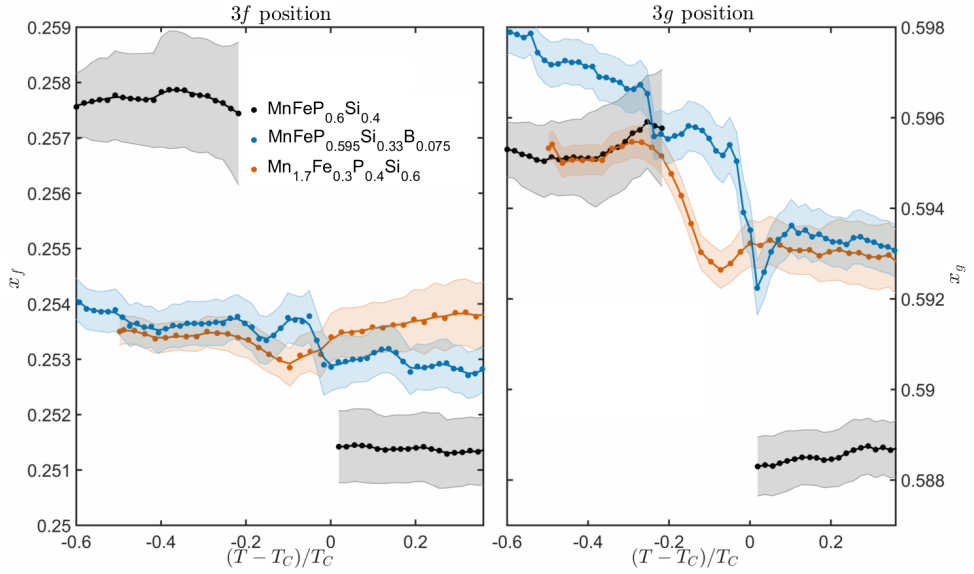

Figure 6.5: Internal coordinates x_f and x_g as a function of the reduced temperature. The data points in the phase coexistence region of the FOMT sample were not included because of the large uncertainty. The error bars are represented as a shaded region around the curve.

The diffraction patterns can also be used to investigate the electron density, using the structure factors obtained in the refinement. By taking the difference between the FM and PM states, an electron density difference plot can be constructed. This is only valid after normalization of the data. While the total electron density in the unit cell does not change with temperature, the diffracted intensity decreases with increasing temperature due to thermal diffuse scattering. The sum of all the structure factors should remain constant when multiplied by a temperature-dependent correction factor. This procedure was used to obtain the normalization constant.

For the sample with a FOMT, there is a temperature where the FM phase coexists with the PM phase. In this region, the electron density difference between these two phases can be obtained without applying a temperature-dependent normalization. The Fe atom was used as center. The electron density difference is plotted in Figure 6.6 as a 2D color map in the $a-b$ plane around Fe, both for the experimental data and for the data obtained by DFT calculations. Details on the method are described in chapter 5.

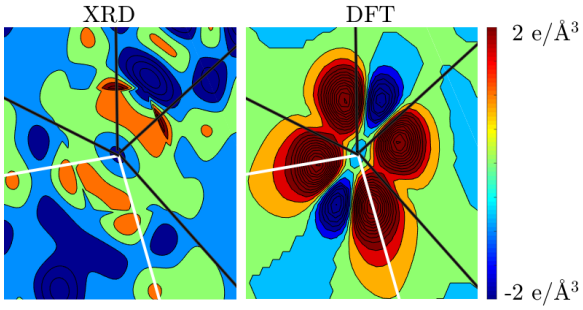

Figure 6.6: The electron density difference plots of the PM state minus the FM state for the FOMT sample (left) and a DFT calculation (right) with Fe at the center. The positive parts are associated with the PM state and the negative parts are associated with the FM state. The white lines are directed towards the Si atoms and the black lines are directed towards other Fe atoms.

For the other samples, there is no region of coexistence and the difference between the two phases can only be shown by subtracting the electron density above and below the transition. The results for all three samples in the $a-b$ plane are shown in Figure 6.7. The features around Fe are similar for all three samples, they show a 'dipole' feature caused by the atomic shift and a region of high density parallel to the [110] direction. Around Si the data do not show a consistent picture for the FOMT, CPT and SOMT samples. The electron density difference plots comparing the PM state far above the transition and just above the transition are shown in Figure 6.8. For these plots, the features around Fe are still visible for the SOMT sample, but are absent for the other samples.

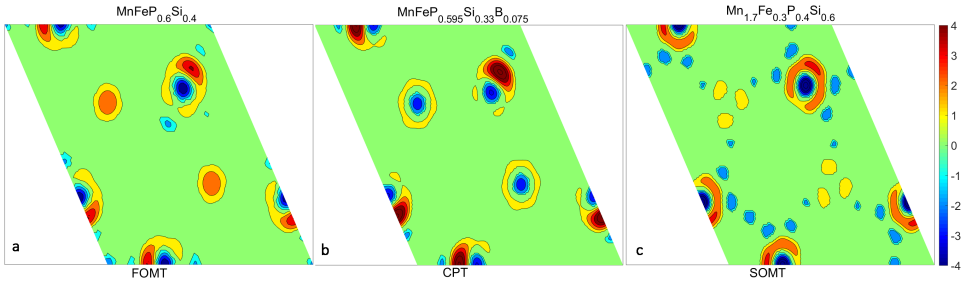

Figure 6.7: Electron density difference plots, between the PM phase far above the transition ($T = T_C$+100 K) and the FM phase just below the transition ($T = T_C$−20 K). The shift in atomic coordinates of the $3f$ position (preferentially occupied by Fe) is recognizable by the dipole feature. The positive (PM) electron density is oriented towards Si and the negative (FM) electron density along the diagonal. The main features are similar for all three samples. The scale is in $e/\text{Å}^3$.

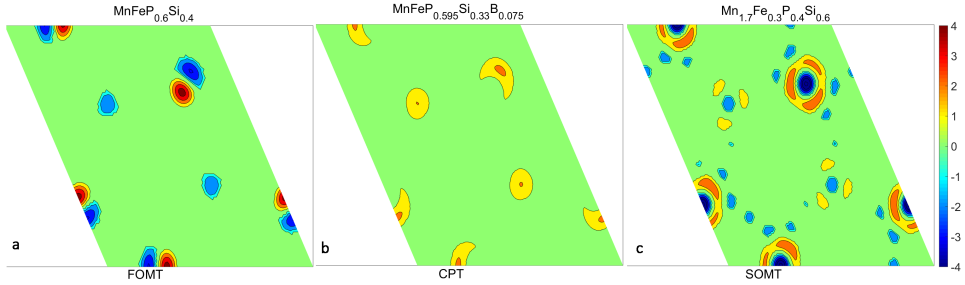

Figure 6.8: Electron density difference plots, between the PM phase far above the transition ($T = T_C$+100 K) and the PM phase just above the transition ($T = T_C$+20 K). The scale is in $e/\text{Å}^3$.

6.4. Discussion

The difference in behavior between the three samples becomes most apparent when we look at the change in lattice parameters. The change in lattice parameters for the FOMT sample is about 5× more pronounced compared to the CPT sample and about 10× compared to the SOMT sample. For these compositions, the changes in lattice parameters hardly affect the volume; the volume change is 1 to 2 orders of magnitude lower. Apparently, the substitution of P for B, which leads to a smaller unit cell, has a profound effect on the transition. However, the size of the unit cell is not the only factor that decreases the magnitude of the effect, for the SOMT sample has the largest unit cell.

The change in lattice parameters with respect to the linear expansion observed in the PM state corresponds to the elastic strain originating from the ferromagnetic order. When the elastic energy and a bilinear magnetoelastic coupling are included, the change in Gibbs free energy becomes:

$$\Delta G = \frac{\alpha}{2}M^2 + \frac{\beta}{4}M^4 + \frac{\gamma}{6}M^6 - \mu_0 HM + 1/2\sum_{i,j} C_{ij}e_i e_j + \sum_i \xi_i e_i M \tag{6.3}$$

where C_{ij} are elastic constants, e_i is the elastic strain and ξ_i is the magnetoelastic coupling constant. Since the hexagonal symmetry of the system is not broken by the ferromagnetic order, only the tensile strains within the basal plane $e_i = \Delta a/a$ and along the sixfold axis $e_3 = \Delta c/c$ will develop:

$$\frac{e_1}{M} = \frac{\xi_1 C_{33} - \xi_3 - C_{13}}{2C_{13}^2 - C_{33}(C_{11} + C_{12})} \tag{6.4}$$

$$\frac{e_3}{M} = \frac{\xi_3(C_{11} + C_{12}) - 2\xi_1 C_{13}}{2C_{13}^2 - C_{33}(C_{11} + C_{12})} \tag{6.5}$$

As can be seen in Table 6.2, all three materials have been chosen to have a low volume change across the transition. In this case we find $e_v = 2e_1 + e_3 \approx 0$. We therefore define $e \equiv e_1 \approx -\frac{1}{2}e_3$. The change in c/a ratio is characteristic for the transformation strain and amounts to $\Delta(c/a)/(c/a) = e_3 - e_1 \approx -3e$. In this case the magnetoelastic coupling constants can be deduced from the dependence of the transformation strain on the order parameter M:

$$\xi_1 \approx (2C_{13} - C_{11} - C_{12})\frac{\partial e}{\partial M} \tag{6.6}$$

$$\xi_3 \approx (C_{13} - C_{33})\frac{\partial e}{\partial M} \tag{6.7}$$

In Figure 6.9 the scaled transformation strains e_1 and $-\frac{1}{2}e_3$ are plotted as a function of the normalized magnetization M. The linear dependence between the transformation strain and the magnetization confirms the presence of a bilinear magnetoelastic coupling around T_C, and indicates that higher order terms are not required to describe

Table 6.4: Calculated elastic constants for $MnFeSi_{0.33}P_{0.66}$ in the FM state [16] and magnetoelastic coupling constants $\xi(10^3$ N/Am)) calculated from the elastic constants (GPa) and $\frac{\partial e}{\partial M}$ (m/A).

	$\frac{\partial e}{\partial M}$	ξ_1	ξ_2
FOMT	11.7	1.17	-1.95
CPT	1.54	0.15	-0.25
SOMT	0.98	0.10	-0.14

the system. From the experimental slopes and the calculated elastic constants [16], the magnetoelastic coupling parameters listed in Table 6.4 are deduced. The elastic constants $C_{11}, C_{12}, C_{13}, C_{33}, C_{44}$ and C_{66} are 308.3, 79.5, 114.0, 227.8, 119.5 and 114.4 GPa, respectively [16].

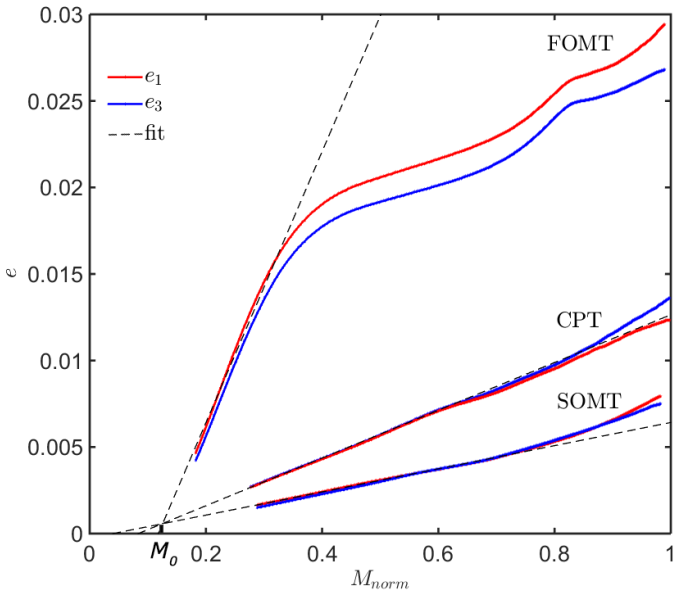

Figure 6.9: Strain $e \equiv e_1 \approx -\frac{1}{2}e_3$ as a function of the normalized magnetization at T = 100 K. Linear fits around T_C show that the coupling constants ξ are largest for the FOMT sample, followed by the CPT and SOMT samples. M_0 is the induced magnetization above T_C by the magnetic field of 1 T.

All linear fits intersect at M_0 due to the tail above T_C, induced by the applied field of 1 T. It also gives a small deviation in the lattice parameters compared to the linear expansion, shifting the data up. A clear trend is visible: the coupling is strong for the FOMT sample and decreases as the transition becomes second order.

Given the change in lattice parameters across the transition, we can investigate the influence of the relative position of the atoms on the $3g$ (Mn) and $3f$ (Fe) site, respectively. Because the ferromagnetism of the low temperature phase restrains the total symmetry of the system because of the broken time-inversion symmetry, going to a paramagnetic state could increase the total symmetry. In this case this could manifest

itself due to the appearance of an inversion center in the crystallographic unit cell. The relative positions of Mn and Fe could assume a value ($x = 0.5$) where the total symmetry is increased due to an inversion center. However, the actual values for x are not close to this symmetry point and the symmetry cannot be increased this way. Instead, it is more insightful to focus on the changing interatomic distances.
For Mn, the change in the unit cell is large for the FOMT sample and would result in a 3% change in Mn-1b distances. However, when the shift in the internal coordinate is taken into account, we see that the distance only changes by about 1%. The change in x_g-parameter therefore partially compensates for the change in unit cell parameters. However, when we look at the SOMT and CPT samples, it is found that the lattice parameter change is compensated by the internal parameter of Mn so that both Mn-X distance changes are effectively zero. This has been illustrated in Figure 6.10.

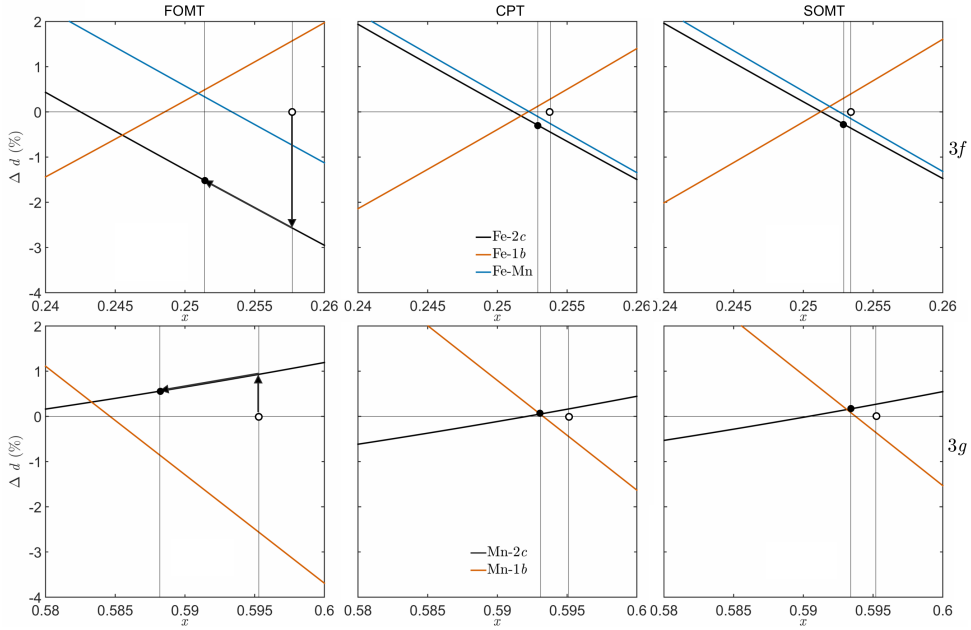

Figure 6.10: Change in interatomic distances Δd induced by the lattice parameters as a function of internal x-coordinate of Fe and Mn for the FOMT, CPT and SOMT samples. The arrows illustrate the changes for both M-2c distances in the FOMT sample: across the transition, the distance decreases (vertical line) due to the change in lattice parameters. In addition, the relative position of Fe changes (diagonal line), the combined distance change is between the original position (open circle) and final position (closed circle).

For the layer preferentially occupied by Fe, this is not the case. For the SOMT sample, there is also a compensation point at $x_f = 0.25$, but Fe only shows a partial shift to this position. This results in a reduced, but finite change in distance. The Fe-occupied layer must play an active role in the transition, as was predicted earlier[12]. The fact that this behavior is observed for all samples, indicates that the mechanism behind the transition is also similar.

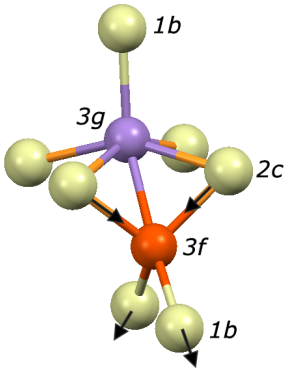

Figure 6.11: Tetrahedral and square-based pyramidal coordination polyhedra around the $3f$ and $3g$ sites, respectively. Across the transition, all samples show a change in the tetrahedron, moving the $2c$ position closer and elongating the distance to $1b$. For the FOMT sample the changes are large enough to affect the $3g$ distances. No appreciable change in coordination takes place.

To illustrate the changes, it is useful to consider the atomic environment around the magnetic $3f$ and $3g$ sites. The $3f$ site has a tetrahedral coordination with two $2c$ and $1b$ sites at unequal distances (see Table 6.3). The $3g$ site has a square-based pyramidal coordination with four $2c$ sites and one $1b$ site. From Figure 6.10 it is clear that the distances in the tetrahedral polyhedron change across the transition, while the distances in the square-based pyramidal polyhedron hardly change.

This magnetoelastic transition can therefore be viewed as an isostructural phase transition. The first crystal structure ($hex1$) has "large" interatomic distances in the $a-b$ plane, the second ($hex2$) has "small" interatomic distances. While the structural properties of both phases can easily be probed, the magnetic properties of both phases cannot be easily probed. For the low temperature phase the magnetization is known, while for high temperatures T_C is known. The calculations in chapter 5 show that the moments size for $hex2$ is significantly lower compared to $hex1$. The value of T_C can be estimated using the spin fluctuation temperature T_{SF}, as proposed by Mohn and Wohlfarth [17,18]

$$T_C \propto T_{SF} = \frac{M_0^2}{10 k_B \chi_0}. \tag{6.8}$$

where M_0 is the average magnetic moment per atom in μ_B at 0 K and χ_0 is the exchange enhanced susceptibility at equilibrium which includes the exchange parameter I

$$\chi_0^{-1} = \left(\frac{1}{4\mu_b^2}\right)\left(\frac{1}{N^+(\epsilon_F)} + \frac{1}{N^-(\epsilon_F)}\right) - 2I_s \tag{6.9}$$

Using Equation 6.8, the reduction of the moment in one sublattice leads to a decrease of the T_C by a factor of 2-3, based on previous calculations [19,20]. The fact that the T_C values for all samples are in the same range, leads us to believe that the reduced moment in the paramagnetic phase is present in all samples.

So far, the discussion has focused on the similarities between the samples, which all transform from $hex1$ to $hex2$. It is also important to investigate the difference be-

tween the FOMT and SOMT samples. For that reason, we focus on the electron density difference plots just above and below the phase transition, as shown in Figure 6.7 and Figure 6.8. Apart from the dipole feature on the $3f$ site, there is also a redistribution of electron density around this site. All three samples show this, although with different contrast. When crossing the transition, this feature disappears for the FOMT and CPT samples, but not for the SOMT sample. This suggests that for the SOMT sample, the electronic redistribution is not complete in this temperature interval. We believe that short-range order is an important effect that is found to extend far into the paramagnetic state. It causes a more gradual continuous change in the electronic structure[21].

6.5. Conclusions

In summary, the structural and electronic properties of $(Fe,Mn)_2(P,Si,B)$ samples with a FOMT, CPT and SOMT have been studied. Both the lattice parameters and the internal coordinates of Mn and Fe change across the transition. For Fe in the tetrahedral coordination the two interatomic distances with the $2c$ position decrease and the two distances with the two $1b$ position increase, while the Fe-Mn distance remains constant. For Mn in the square based pyramidal coordination, all interatomic distances remain constant. For the FOMT sample the changes cannot be accommodated and the sample subsequently shows a large thermal hysteresis. The changes in the tetrahedral arrangement around Fe are similar for all samples and the transitions can be viewed as an isostructural transition resulting in different magnetic properties. Both the changes in interatomic distances and the electron density plots clearly show that the mechanism is the same for all samples. In addition, the T_C of the samples is much lower compared to the estimated T_C, based on the low temperature phase. It is not yet clear what factors govern the sharpness of the transition, but based on the electron density difference plots it is clear for the SOMT sample the observed changes are smaller and continuously extending over a wide temperature range in the paramagnetic state, probably due to short-range order.

References

[1] O. Tegus, E. Brück, K. H. J. Buschow and F. R. de Boer. 'Transition-metal-based magnetic refrigerants for room-temperature applications.' Nature volume 415, pp. 150–152 (2002).

[2] S. Rundqvist and F. Jellinek. 'The structures of Ni_6Si_2B and Fe_2P and some related phases.' Acta Chem. Scand. volume 13, pp. 425–432 (1959).

[3] L. Lundgren, G. Tarmohammed, O. Beckman et al. 'First order magnetic phase transition in Fe_2P.' Phys. Scr. volume 17, pp. 39–48 (1978).

[4] L. D. Landau. 'On the theory of phase transitions. I.' Zh. Eksp. Teor. Fiz. volume 7, pp. 19–32 (1937).

[5] H. Wada and Y. Tanabe. 'Giant magnetocaloric effect of $MnAs_{1-x}Sb_x$.' Appl. Phys. Let. volume 79, pp. 3302–3304 (2001).

[6] N. H. Dung, L. Zhang, Z. Q. Ou and E. Brück. 'From first-order magneto-elastic to magneto-structural transition in $(Mn,Fe)_{1.95}P_{0.50}Si_{0.50}$ compounds.' Appl. Phys. Lett. volume 99, p. 092511 (2011).

[7] N. V. Thang, X. F. Miao, N. H. van Dijk and E. Brück. 'Structural and magnetocaloric properties of $(Mn,Fe)_2(P,Si)$ materials with added nitrogen.' J. Alloys Comp. volume 670, pp. 123–127 (2016).

[8] F. Guillou, G. Porcari, H. Yibole et al. 'Taming the First-Order Transition in Giant Magnetocaloric Materials.' Adv. Mater. volume 27, p. 2671 (2014).

[9] X. F. Miao, N. V. Thang, L. Caron et al. 'Tuning the magnetoelastic transition in $(Mn,Fe)_2(P,Si)$ by B, C, and N doping.' Scripta Mat. volume 124, pp. 129–132 (2016).

[10] X. F. Miao, L. Caron, P. Roy et al. 'Tuning the phase transition in transition-metal-based magnetocaloric compounds.' Phys. Rev. B volume 89, p. 174429 (2014).

[11] R. Skomski. 'Finite-temperature behavior of anisotropic two-sublattice magnets.' J. Appl. Phys. volume 83, pp. 6724–6726 (1998).

[12] N. H. Dung, Z. Q. Ou, L. Caron et al. 'Mixed Magnetism for Refrigeration and Energy Conversion.' Adv. Energy Mater. volume 1, pp. 1215–1219 (2011).

[13] F. Guillou, G. Porcari, H. Yibole et al. 'Taming the first-order transition in giant magnetocaloric materials.' Adv. Mater. volume 27, pp. 2671–2675 (2014).

[14] J. Rodríguez-Carvajal. 'FULLPROF: A Program for Rietveld Refinement and Pattern Matching Analysis.' Satellite Meeting on Powder Diffraction of the XV IUCr Congress volume 127 (1990).

[15] K. Momma and F. Izumi. 'VESTA 3 for three-dimensional visualization of crystal, volumetric and morphology data.' J. Appl. Crystallogr. volume 44, pp. 1272–1276 (2011).

[16] P. Roy, E. Torun and R. A. de Groot. 'Effect of doping and elastic properties in $(Mn,Fe)_2(Si,P)$.' Phys. Rev, B volume 93 (2016).

[17] P. Mohn and E. P. Wohlfarth. 'The Curie temperature of the ferromagnetic transition metals and their compounds.' J. Phys. F: Met. Phys. volume 17 (1987).

[18] P. Mohn. Magnetism in the solid state. Springer-Verlag (2003).

[19] M. F. J. Boeije, P. Roy, F. Guillou et al. 'Efficient Room-Temperature Cooling with Magnets.' Chem. Mater. volume 28, p. 4901–4905 (2016).

[20] P. Roy, E. Brück and R. A. de Groot. 'Latent heat of the first-order magnetic transition of $MnFeSi_{0.33}P_{0.66}$.' Phys. Rev. B volume 93 (2016).

[21] X. F. Miao, L. Caron, J. Cedervall et al. 'Short-range magnetic correlations and spin dynamics in the paramagnetic regime of $(Mn,Fe)_2(P,Si)$.' Phys. Rev. B volume 94, p. 014426 (2016).

7

Phase stability of $CaCu_5$-based materials

7.1. Introduction

The phase stability of crystal structures is of immense practical importance[1], as the crystallographic phase largely determines the material properties. Materials that crystallize in the $CaCu_5$-type crystal structure, shown in Figure 7.1, are important as permanent magnets[2] and are heavily used in metal hydride batteries[3]. This has given rise to a huge number of publications on compounds having this crystal structure, which is reflected in 1600 entries in the Pearson Crystal Database[4]. This data can give insight in the stability of the phase. Generally, the combined data extracted from crystallographic databases is used to predict the crystal structure, for a given composition[5]. Here we try to answer a more experimentally relevant question: given a certain crystal structure, what compositions are stable? This is highly relevant for technologically important YFe_5 [6–8]. This composition does not result in the formation of the $CaCu_5$ phase, but instead forms Y_2Fe_{17} and Y_6Fe_{23}.

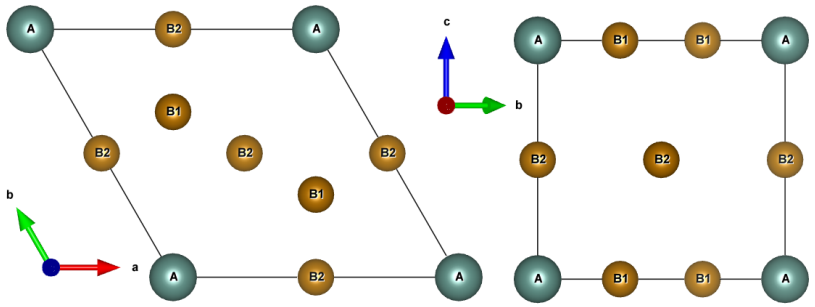

Figure 7.1: The hexagonal unit cell of the $CaCu_5$ type crystal structure with general formula AB_5.

For intermetallic compounds, the Miedema model can be used to describe the stability based on the enthalpy of the phase compared to the enthalpy of the constituent elements[9]. This semi-empirical approach has proven to show good agreement with experiment[10] and first-principle calculations[11]. In this model, the enthalpy of formation is calculated by considering a cohesive contribution and a destabilizing contribution based on the electron density. The cohesive contribution is based on the difference in work function of the elements $\Delta\Phi^*$, while the electron density difference, based on the average electron density at the boundary of the Wigner-Seitz cell $\Delta n_{WS}^{1/3}$, represents the destabilizing contribution. The interfacial enthalpy of A surrounded by B is given by

$$\Delta H_{AB} = \frac{V_A^{2/3}}{< n_{WS}^{1/3} >}(-P(\Delta\phi^*)^2 + Q(\Delta n_{WS}^{1/3})^2). \tag{7.1}$$

where $V_A^{2/3}$ is the contact surface area of A, $< n_{WS}^{1/3} >$ is the average electron density and P and Q are dependent on the atomic species. The total enthalpy of formation upon alloying can be determined by taking the concentration c into account:

$$\Delta H = c_A c_B (f_B^A \Delta H_{AB} + f_A^B \Delta H_{BA}) \tag{7.2}$$

where f_B^A represents the degree to which A is surrounded by B. The free enthalpy change is approximately equal to the Gibbs free energy change upon alloying. This approach was initially used to describe binary compounds, but was later extended to ternary compounds, by taking the sum of all contributions $\Delta H_{ABC} = \Delta H'_{AB} + \Delta H'_{AC} + \Delta H'_{BC}$[12,13] where $\Delta H'_{XY}$ takes the composition into account. In this discussion, the value of ΔH does not yield information on the adopted crystal structure.

Density functional theory (DFT) calculations do include the crystal structure and can provide the free enthalpy. However, the prediction of a stable compound is not straightforward and the value of the free enthalpy alone does not show the stability of a particular phase. The proper way to do this is to evaluate the global minima of the free enthalpy in a landscape of crystal structures and compositions[14]. Another approach is to analyze existing stable compositions using structure mapping[5,15–17]. This method can be applied to thousands of compositions in seconds, in contrast to the timescales encountered in using DFT methods. In this paper, we present a new approach that combines the semi-empirical parameters that produce accurate results in the Miedema model and the crystallographic data contained in the Pearson database[4]. This is realized by making phase stability plots using $\Delta\phi^*$ and $\Delta n_{WS}^{1/3}$. We extend these values from binary to pseudo-binary compounds by taking the weighted average of the element values. This allows to easily extend these parameters beyond the original scope and without using the experimentally determined P and Q parameters. The obtained stability plots allow for a quick inspection of the phase stability across element combinations. We will show that the application of such a model does not only give a good prediction on phase stability, it also gives valuable information on the factors that govern crystal structure formation in these compounds.

7.2. Methods

Computational methods

Three different datasets were extracted from the Pearson's Crystal Database (PCD)[4]. The first is used to assess the predictive power of the Miedema model and contains 3726 entries with unique compositions, by considering all metals without p-type valence electrons. The second is used for the stability of compounds with the $CaCu_5$-type crystal structure, and contains 413 compositions. This number is reduced to 387 when only considering compounds that have a generic formula AB_5. The last set contains $CaCu_5$-derived crystal structures and contains 863 unique compositions. For the stability maps, unstable compounds were generated, based on the assumption that all stable binary compounds have been found. For all entries, compositions containing hydrogen, radioactive elements and actinides were omitted. The position of a compound in the stability map is determined by properties of its atomic constituents. The Miedema parameters Φ^* [18] and $n_{WS}^{1/3}$ were used[9], including atomic radii[19]. The weighed properties were normalized $\Omega_w = (a\Omega_A + b\Omega_B)/(a+b)$ for compounds with formula A_aB_b[5]. An ellipse demarcates the separation between stable and unstable compounds. The procedure to determine the parameters describing the ellipse can be found in the appendix.

Within the DFT framework[20,21], the projector augmented wave method as implemented in the Vienna Ab initio Simulation Package (VASP)[22–25] was used to generate the total charge and charge densities for ten AB_5 compounds, that is YCu_5, YFe_5, YNi_5, YCo_5, YZn_5, YGa_5 and $BaCu_5$, $CaCu_5$, $MgCu_5$, $SrCu_5$. Exchange-correlation interactions were taken into account via the Perdew- Burke-Ernzerhof type generalized gradient approximation[26]. The $4s$ and $3d$ electrons were treated as valence electrons for Cu, Fe, Ni, Co, Zn. For Y the $4s$, $4p$, $5s$, $4d$, for Ga the $4s$, $4p$, for Mg the $2s$, for Ca the $3s$, $3p$, $4s$, for Sr the $4s$, $4p$, $5s$ and for Ba the $5s$, $5p$ and $6s$ electrons were treated as valence electrons. The lattice parameters and atomic positions for all compounds were relaxed using the conjugate gradient algorithm until a 0.01 meV/Å force convergence was reached. The plane-wave cutoff and the energy convergence criteria were set to 460 eV and 10^{-8} eV in a $11 \times 11 \times 11 (13 \times 13 \times 13)$ Gamma centered k-point mesh for the structural relaxation (charge density calculation).

The stability of $Y(Ni_{1-x}Fe_x)_5$ against YNi_5 and YFe_5 compounds have been investigated by the Exact Muffin-Tin Orbitals-Full Charge Density (EMTO-FCD) method[27]. The chemical disorder was treated via the coherent potential approximation (CPA)[28,29] and the electrostatic correction to the single-site CPA was described using the screened impurity model[30] with a screening parameter of 0.6. The one-electron equations were solved within the scalar relativistic and soft-core approximation. The Green's function was calculated for 24 complex energy points distributed exponentially in a semicircular contour. The s, p, d and f orbitals (l_{max}=3) were included in the EMTO basis set. The one-center expansion of the full charge density was truncated at l^h_{max}=8. To obtain the accuracy needed for the total energy calculation we used about 250 k points in the irreducible wedge of the Brillouin zone. At each Fe concentration x, the equilibrium total energy $E(x)$ was derived from an exponential Morse-type function[31] fitted to the total energies calculated at 0 K for five different atomic volumes. The local density approximation (LDA)[32] was used for the exchange-correlation functional which gives a 99% agreement for the theoretical lattice parameter compared to the experimental one for YNi_5. The mixing quantities ΔC, e.g. enthalpy of formation ΔH, Gibbs energy of formation ΔG and mixing entropy ΔS, are calculated as $\Delta C = C(x) - (1-x)C(YNi_5) - xC(YFe_5)$. The configurational entropy and the magnetic entropy is taken into account within the mean field approximation as $S_{conf} = -k_B[x\ln x+(1-x)\ln(1-x)]$ and $S_{mag} = -k_B[x\ln(M+1)]$, respectively[33].

Experimental methods

Fe granules (99,98%), Y granules (99.5%), Sn shot (99.99%) and Si spheres (99.9%) were melted in an custom-built arc melting furnace. The obtained buttons were turned three times and subsequently melt spun to facilitate the phase formation. Weight losses by evaporation are less than 0.5%. The samples were sealed in quartz ampoules, filled with Ar, annealed at 900°C for two days and quenched to room temperature. Room-temperature X-ray diffraction (XRD) measurements were performed on a PANalytical X'Pert PRO diffractometer using Co kα–radiation.

7.3. Results and discussion

7.3.1. Phase stability in binary compounds

The Miedema plots[9] were made using data obtained from the Pearson database. A total of 628 binary combinations were found with a solubility larger than 7%. Nonradioactive elements were selected from the s, p and d block of the periodic table. Elements from the p-block in the periodic system have not been included in this section. Because of the metalloid nature of these elements, an additional term (R) is needed to model the formation enthalpy. A total of 217 unstable compounds was generated based on the available element combinations. The combined data are plotted in Figure 7.2.

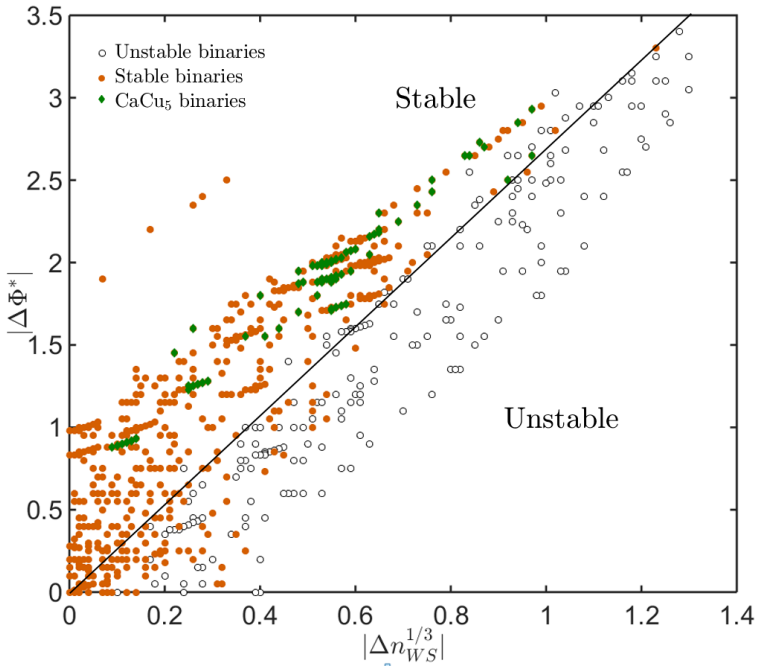

Figure 7.2: The difference in work function $|\Delta\Phi^*|$ as a function of the difference in electron density $|\Delta n_{WS}^{1/3}|$ for all binary compounds of d metals combined with s, f metals. Stable compounds (628 red dots) were extracted from the Pearson database, for cases where the solubility is larger than 7%. Unstable compounds were generated, omitting the stable compounds (217 black circles). Above the black line, stable compounds are present, while below the black line, mostly compounds that do not form are present. Element combinations that are able to form the $CaCu_5$ crystal structure are indicated with green diamonds and show a linear trend.

The plot shows a separation between stable and compounds and compounds that do no not form, illustrated by a demarcation line. The separation between stable and unstable compounds is clear where the individual elements have strong dissimilar electronic properties. When elements have similar electronic properties, the separation is less pronounced, especially for $\Delta n_{WS}^{1/3} < 0.2$. For these compounds, the entropy of formation is expected to have a relatively large contribution compared to the enthalpy of formation.

The (configurational) entropy can be kept constant by considering only one crystal

structure. For compounds that crystallizes in the $CaCu_5$ prototype structure, the configurational entropy is the same and a linear relationship is found between the work function and electron density. This leads us to argue that the Miedema parameters can give valuable insight into the phase stability of binary compounds.

Elements from the p-block in the periodic system have not been included. Because of the metalloid nature of these elements, additional considerations are needed to model the formation enthalpy.

7.3.2. Phase stability of $CaCu_5$ type compounds

Analogous to the original Miedema plot, the phase stability of a given crystal structure can be investigated. In order to do this, compositions that form the crystal structure in question are plotted together with compositions that do not form this crystal structure. Assuming that the most common phases of binary compounds have been documented, one can generate a list of unstable binary compositions. By analyzing the occurrence of the various elements in the database, one can reduce the number of unrealistic elemental combinations. This is shown in Figure 7.3.

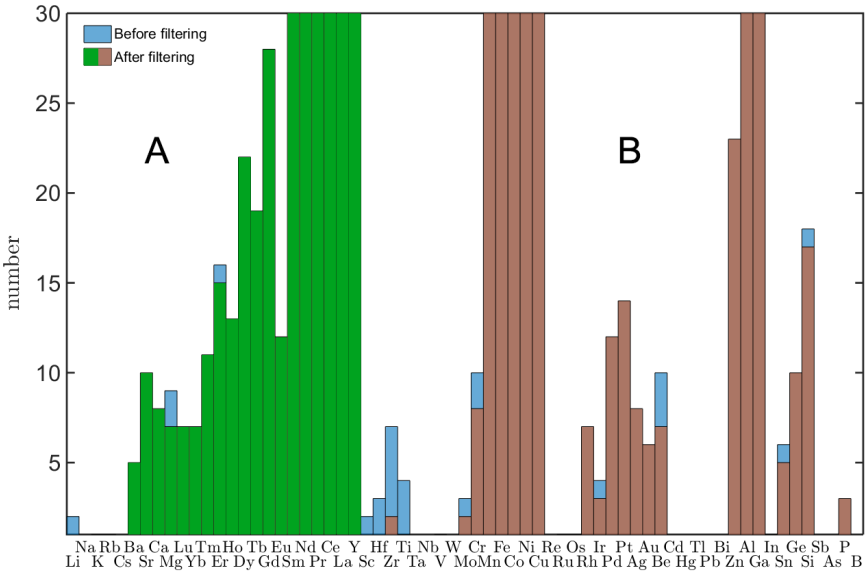

Figure 7.3: Histogram of the element combinations forming the $CaCu_5$ crystal structure. Each increment on the y-axis is equal to a unique composition. By filtering the raw data by only considering compounds with generic formula AB_5, a strict distinction between elements A and B can be made, indicated in two regions containing green and brown columns respectively. The x-axis is based on the Pettifor coordinate and traverses the periodic table first by group and then by period.

Elements from the s and f block occupy the A position, while elements from the d block occupy the two B positions. The p-block elements are also present for some compositions, but they form substitutional alloys and never fully occupy the B positions. The demarcation between A and B is made by Y. Early d-block elements have been filtered out because they have a different stoichiometry or act as dopants.

Using the histogram, all combinations between A and B can be generated and compared to the binary compounds found in the Pearson database. By calculating an average weighted value for the properties of A and B in $(A_{1-x}A'_x)(B_{1-y}B'_y)_5$, it is possible to also include pseudo-binary compounds. This approach has been used earlier[5] and uses an average-atom model[34]. Using such a strategy, Figure 7.4 was made, by presenting compounds with up to ten different elements. It contains 387 unique stable compounds and 693 unstable binary compounds.

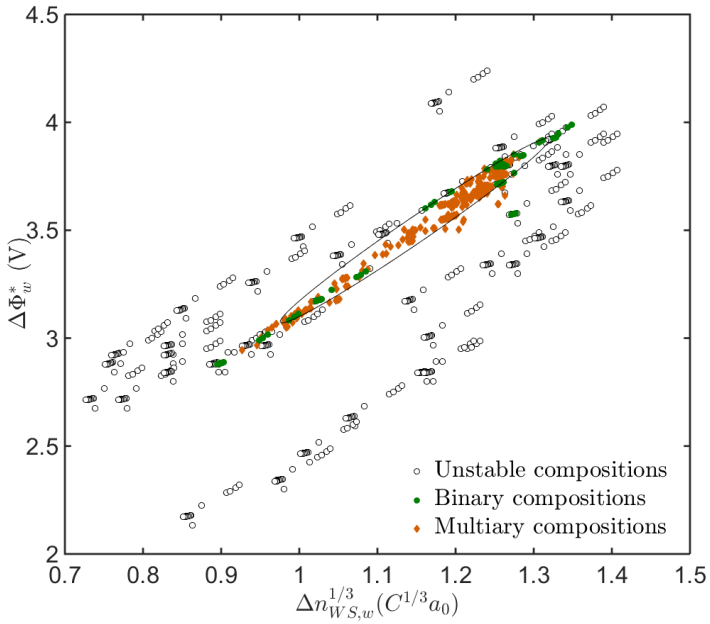

Figure 7.4: Phase stability plot of $\Delta\Phi^*_w$ and $\Delta n^{1/3}_{WS,w}$, which are weighted and normalized using the stoichiometry. Green dots and red diamonds represent stable compounds and black circles are calculated binary compositions. Binary compositions were complemented with multiary compounds (ternary, quaternary compounds, etc.). The stability region is demarcated by an ellipse. Compounds found outside the ellipse are based on Zn (left) and Pt/Ir (right), and Fe (below). Fe shows a deviation from the linear behavior and is found form a metastable phase. The total probability is 94%.

The phase stability plot is similar to plots used for crystal structure prediction. They both separate two or more regions in phase space. For crystal structure prediction these regions represent two or more stable crystal structures, while in this case it separates stable from unstable compositions. The main difference is that the demarcation lines in crystal structure prediction plots have an arbitrary shape. For the phase stability plots however, the demarcation line can be described by an ellipse showing a total probability of 94% based on the number of experimental / calculated datapoints inside / outside the ellipse. It has to be noted that the presence of p-block elements does not adversely affect these fractions, while they do adversely affect Figure 7.2.

Because the plots are based on electronic properties, the shape of the ellipse can give insight into the electronic properties related to the crystal structure. The linear relation-

ship in the plot is reflected in the rotation angle of the ellipse and gives information about the ratio between charge transfer and charge density mismatch. Apparently, this ratio is a crucial factor governing phase formation. The major and minor axes of the ellipse represent the tolerance in electron density mismatch and charge transfer, respectively. While the stability plot can also be constructed using the electronegativity and valence electron concentration to describe the electronic properties, the shape of the stability region does not allow the same reconstruction. In addition, the valence electron numbers are integers and are therefore less suited for this purpose.

The ratio between the atomic radii also plays a large role in a crystal structure. To illustrate the influence of the radii, a color code was added to the stability plot, corresponding to the weighted difference in atomic radius. For this prototype, the radius difference shows a correlation with $\Delta\Phi^*_w$ and $\Delta n^{1/3}_{WS,w}$, it increases when moving from the upper right corner to the lower left corner of Figure 7.5. This allows us to reduce the 3D plot to 2D by omitting the radius difference. This simplification is probably not valid when considering other prototypes.

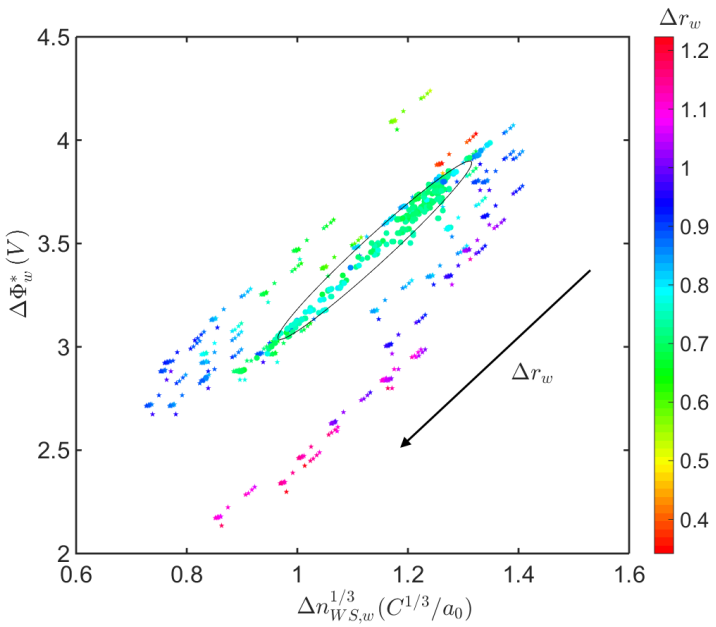

Figure 7.5: Phase stability plot of $\Delta\Phi^*_w$ and $\Delta n^{1/3}_{WS,w}$. The color code corresponds to the radius difference. Unstable compounds are indicated by a star and stable compounds with a dot. Compounds with a small radius mismatch are found in the upper right corner, compounds with a large radius mismatch are found in the lower left corner. The correlation between $\Delta\Phi^*_w$ and Δr_w contributes to the construction of simple 2D plots to assess the stability. Stable compounds are found to have a radius difference between 0.66 and 0.86. Without considering $\Delta n^{1/3}_{WS,w}$, no reliable distinction can be made between stable and unstable compounds.

The proposed model uses the electronic properties of elemental solids and tries to capture the interactions in alloys. To see how well the model describes these interactions, DFT calculations were performed. A compound close to the center line of the

ellipse was chosen as reference: YCu_5. The number of valence electrons was varied by substituting Cu by Fe, Co, Ni, Zn and Ga. The ionicity was varied by substituting Y by Mg, Ca, Sr and Ba. The 4 end members, YFe_5, YGa_5, $MgCu_5$, $BaCu_5$, are unstable while the other 6 compositions form a stable $CaCu_5$ phase. Although it should be noted that in addition the the $CaCu_5$ prototype[35], a different crystal structure is reported for YZn_5[36]. To compare the difference in work function, the charge q is calculated by integrating the electron density over half the (average) A-B distance. The charge difference is obtained relative to YCu_5. The average electron density at half the (average) A-B distance corresponds can directly be compared to $\Delta n^{1/3}_{WS,w}$. The comparison between the model and the DFT calculations is shown in Figure 7.6.

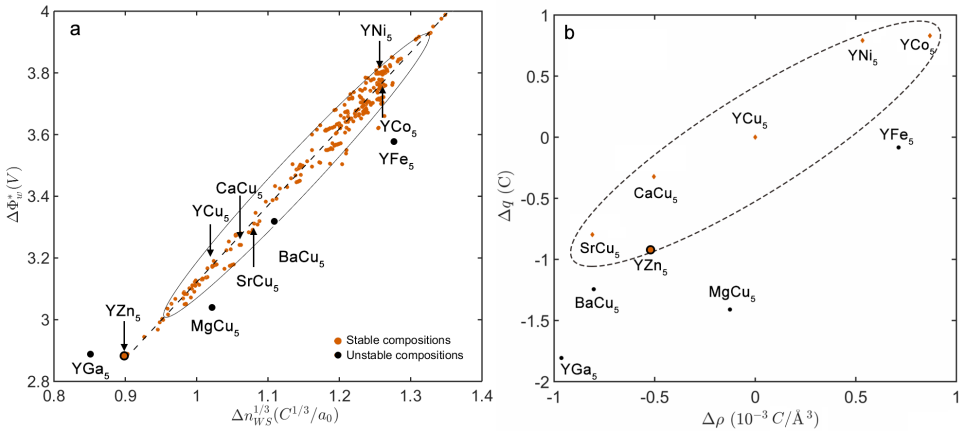

Figure 7.6: Electronic characteristics of $CaCu_5$-type compounds based on elemental properties (a) and determined from DFT calculations (b). Both the model in (a) and the DFT calculations in (b) show a linear behavior. The charge q is obtained by integrating the electron density over half the (average) A-B distance. ρ is the average charge density at the same Wigner-Seitz cell radius. Δq and $\Delta\rho$ are determined relative to YCu_5. While $BaCu_5$ is inside the stability region in (a), DFT calculations shows a large charge difference and supports the observation that $BaCu_5$ is unstable. Because there are two reported crystal structures of YZn_5[35,36], this compound is indicated with a filled circle. The dashed lines are guides to the eye.

The calculations show relative changes in the total charge and density at the boundary of the Wigner-Seitz cell compared to YCu_5. The plot shows large deviations for Fe and Mg based compounds, in line with the model. The relatively small deviation of $BaCu_5$ is enlarged in the DFT calculations, and shows that the model underestimates the charge transfer in Ba. YZn_5 follows the trend of the stable compounds, but is on the tolerance limits.

7.3.3. Stability of YFe_5

Because of the technological importance of the Fe-based compounds and the fact that there are some reports on Fe-based $CaCu_5$-type compounds, special attention is given to this group of materials. YFe_5 has been synthesized and the $CaCu_5$-type crystal structure was indeed found. By varying the composition from the ideal value of 16.7% Y, different fractions of the $CaCu_5$-type crystal structure were measured, together with Y_2Fe_{17} and Y_6Fe_{23}. The samples were arc melted and subsequently melt spun. For the as-cast sample containing 15 at.% Y, a volume fraction of 60% YFe_5 was measured, decreasing the Y_2Fe_{17} phase. This can indicate that an off-stoichiometry leads to stabilization or hint to a particular cooling profile. The optimum atomic fraction of Y is not found at 16.7%, but is shifted to about 14%, as shown in Figure 7.7.

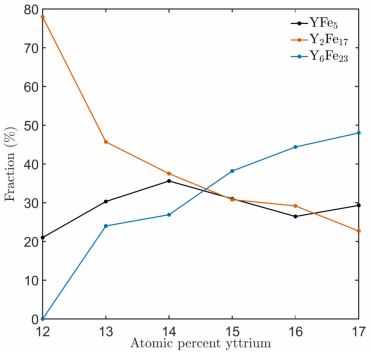

(a) Experimental phase volume fractions of Y-Fe compounds. After annealing, the YFe_5 phase was transformed to the Y_2Fe_{17} phase.

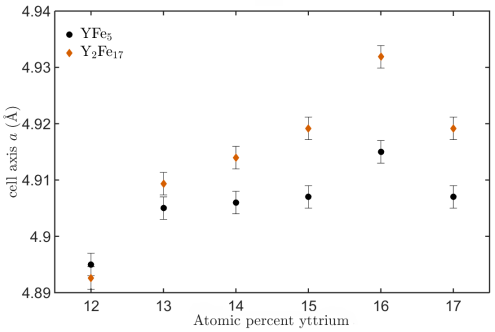

(b) Lattice parameter a of YFe_5 and the reduced lattice parameter $a/\sqrt{3}$ of Y_2Fe_{17}. Although Y_2Fe_{17} is a supercell of YFe_5, there is a small difference in reduced lattice parameters. The differences in c are within the statistical error.

Figure 7.7: Experimental properties of Y-Fe compounds with varying compositions, determined by powder X-ray diffraction.

After annealing, YFe_5 was completely transformed into the other two phases, indicating a metastable state. In fact, Fe-based compounds found outside the stability region are all metastable. The refined X-ray powder diffractogram of the sample with 16 at.% Y is shown in Figure 7.8. Because the unit cell of the Y_2Fe_{17} is related to the unit cell of the YFe_5 phase, it is difficult to distinguish between the two phases. There is, however, a significant difference in the intensity of the {101} peak. The relative intensity is decreased when the samples are annealed, indicating that the metastable YFe_5 phase is transformed. In addition, there is a small lattice mismatch between the YFe_5 and Y_2Fe_{17} phases, around 50°, as shown in Figure 7.7. As a result, the {200} reflection is found to be more narrow after annealing.

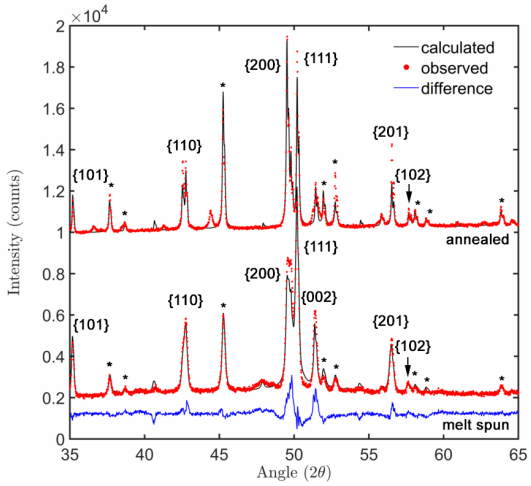

Figure 7.8: Powder X-ray diffractogram of melt-spun $Y_{15}Fe_{85}$. The $CaCu_5$-type crystal structure can be recognized by the equal intensities at the {101} and {110} reflections. The Y_6Fe_{23} reflections are indicated with an asterisk. After annealing, the relative intensity of the {101} reflection decreases as metastable YFe_5 is transformed. In this case, the phase is 30%. In addition, small deviations in the lattice parameters of the YFe_5 and the reduced unit cell of Y_2Fe_{17} are visible in the {200} reflection.

7.3.4. Pseudo-binary crystal structures

The model can be extended to ternary crystal structures that are modifications of the $CaCu_5$-type crystal structure. The various modifications that can take place are shown in Figure 7.9 and Table 2.1. The most common modification is an ordered substitution, where for $PrNi_2Al_3$ three B positions are occupied by elements possessing p-type valence electrons, while for $CeCo_3B_2$ only two B positions are replaced. Another modification is a superstructure formation, due to the substitution of a B atom for boron or silicon. There are five representatives of such a modification, each increasing the c-axis. A redistribution of atoms can also occur and this is the case for YCo_3Ga_2 and YNi_2Al_3 (substitution of B with Al or Ga). Finally, Si can distort the bond distances and angles, giving rise to $LaRu_3Si_2$ and to $ErRh_3Si_2$, where in the last case the symmetry is lowered to orthorhombic. This already indicates that the electrons show more localized behavior in these materials and that the Miedema model that assumes delocalized behavior will at one point break down.

Modification I does not change the symmetry of the system, but shows a preferential occupation of substituting atoms. This indicates that the average-atom model is no longer valid, because the atoms are not randomly distributed throughout the unit cell. However, the properties of the atoms at the two crystallographic sites are treated the same and does not result in differentiation in phase space, as shown in Figure 7.10. Modification II does change the symmetry of the system because of the M-Si interactions. This symmetry is a subgroup of the $CaCu_5$ symmetry, and it is expected that the phase stability region is also a subgroup of $CaCu_5$. Because these deformations are found in Si-containing systems, these compositions are found in a more narrow region in the

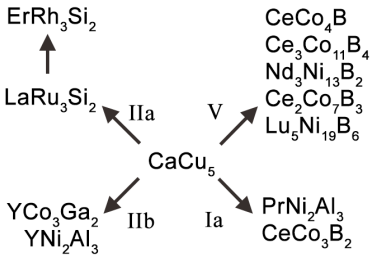

Figure 7.9: Relationships between crystal prototypes (see Table 2.1). Modifications are: Ia ordered substitution, IIa internal deformation with reduction of symmetry, IIb with reduction of symmetry, III redistribution of atoms and V inhomogeneous homologous series (doubling of the unit cell).

stability plot. Modification III has a more profound effect on the unit cell dimensions and is found in another part of the stability region. Apparently, the interactions that give rise to this modification have a smaller tolerance. Modification V is only found in the presence of B, which also confines the stability parameters.

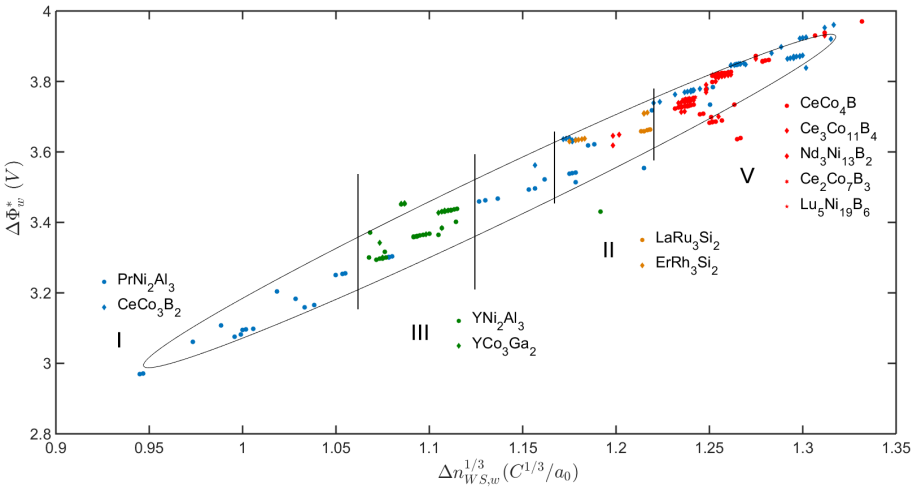

Figure 7.10: The phase stability of $CaCu_5$ (indicated by the ellipse) and crystal modifications. Modification I is an ordered substitution and is found across the stability region. All other modifications (IIa/b internal deformation with/without reduction of symmetry, III redistribution of atoms and V doubling of the unit cell) are found to occupy a distinct part of the phase stability region and are governed by a substitution of d-metals by p-metals.

7.3.5. Fe-based compounds

It was investigated whether by using this model, new stable Fe-based compounds can be synthesized. By linearly interpolating two binary compositions in Figure 7.11, it is possible to cross the stability region. $Y(Fe_{1-x}Ni_x)_5$ for $1 \leq x \leq 5$ was made to test the

validity for substitution of Fe with another element from the d-block. Once nickel is introduced, the metastable phase that was detected earlier for YFe_5 disappears, and the $2:17$ and $1:3$ phases are found. After the stability boundary is crossed, a stable phase is formed.

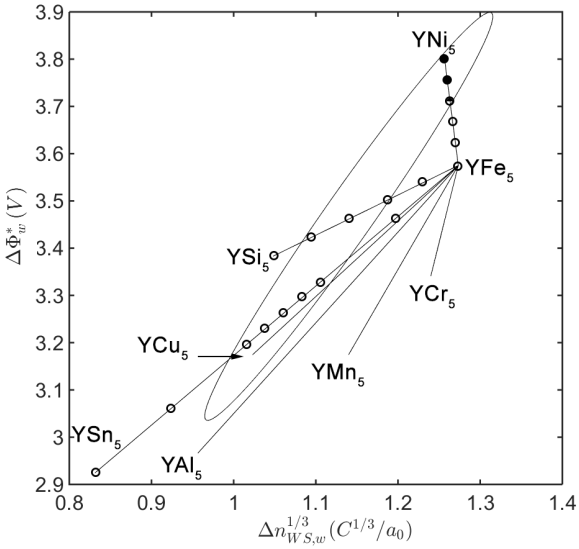

Figure 7.11: The phase stability of YFe_5 compared to a selection of compounds. By linear interpolation, stable compounds can be found by alloying YFe_5 with the selected elements so that the composition falls inside the stability region. The circles correspond to samples that have been made. Full circles indicate the $CaCu_5$ phase, open circles indicate the absence of this phase.

7

Table 7.1: Main phases of $Y(Fe_{1-x}M_x)_5$ for different values of x. Compositions with an asterisk are single phase, the other samples formed multiple phases. Sn-based samples show a $CeNiSi_2$-type crystal structure.

x	Ni	Si	Sn
1	$Y(Fe,Ni)_3$	$Y_2Fe_{15}Si_2$	$YFeSn_2$
2	$Y(Fe,Ni)_3$	YFe_2Si_2	$YFeSn_2$
3	$YFeNi_4$	$Y_2Fe_3Si_5$	$YFeSn_2$
4	$YFeNi_4$*	$Y_3Fe_2Si_7$	$YFeSn_2$
5	YNi_5*	YSi_2	YSn_2

Based on Figure 7.11, two elements from the p-block should also stabilize the phase. Either the $CaCu_5$ phase or a modification can be formed. To this end, $Y(Fe_{1-x}Si_x)_5$ and $Y(Fe_{1-x}Sn_x)_5$ were synthesized. The main phases are shown in Table 7.1. It was found that this did not yield the expected phase and that further investigations are needed. In the paper by Miedema [9], special attention is paid to p-type elements, because of the more localized nature of the electrons in these elements. When these elements are used for substitution in already stable binary compounds, adverse effects are not noticed, but at higher concentrations, for unstable binary compounds, the predictive power is indeed

decreased.

DFT calculations have been performed on the series $Y(Fe_{1-x}Ni_x)_5$ and on YFe_3 as a stable reference. Upon alloying, the free enthalpy of YFe_5 can be compared to YFe_3 + 2 Fe. From Figure 7.12 it is clear that that latter is energetically more favorable, except in the presence of a high Ni concentration. The crossover lies around $x = 0.25$, corresponding to the experimentally determined concentration. The mixing enthalpy and entropy contributions are small, even at 600 K, and hardly affect the linear relationship of the absolute values of H.

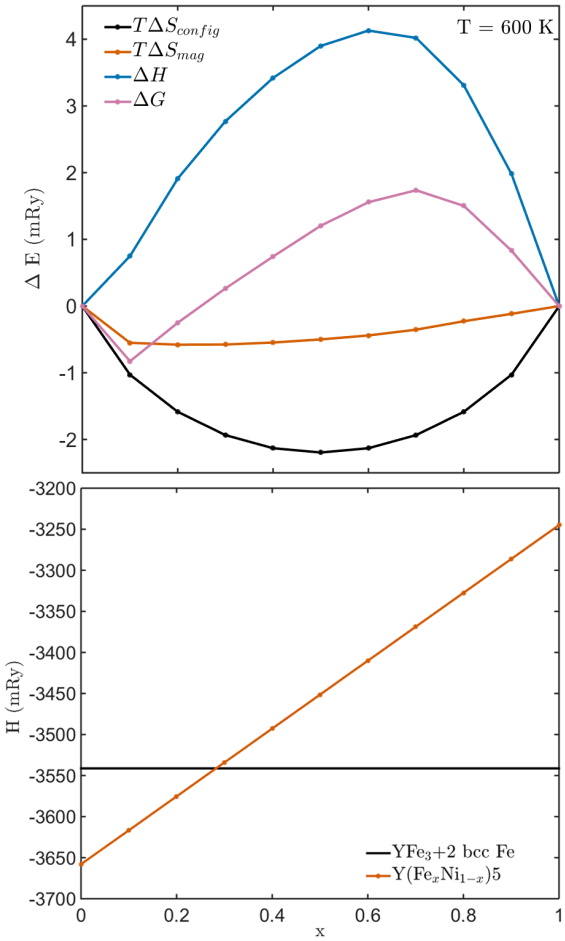

Figure 7.12: The mixing enthalpy and entropy contributions at 600 K of $Y(Fe_xNi_{1-x})_5$ (top) and formation enthalpy (bottom). The total ΔG of mixing hardly affects the absolute formation enthalpy, which shows a crossover with the formation of YFe_3 + 2 bcc Fe around $x = 0.25$.

7.4. Conclusions

It is shown that by using the weighted Miedema parameters, a stability plot can be made, resembling plots used in crystal structure prediction. The plots have in common that they both model the charge transfer and electron density, but instead of using the electronegativity and valence electron number, the work function and electron density at the boundary of the Wigner-Seitz cell are used. By doing so, additional information about the factors that govern crystal structure formation can be obtained. In this case, the linear relationship between all stable compounds show a specific ratio between charge transfer and electron density. This observation is supported by DFT calculations. Not only does the empirical data show the boundary conditions for phase formation, it also allows the prediction of new stable compounds by linearly interpolating two binary compositions of interest. Although the nature of the valence electrons, being of d or p type, must be carefully considered.

References

[1] Y. Zhang, Z. J. Zhou, J. P. Lin et al. 'Solid-Solution Phase Formation Rules for Multi-component Alloys.' Advanced Engineering Materials volume 10, pp. 534–538 (2008).

[2] Y. Hou, Z. Xu, S. Peng et al. 'A Facile Synthesis of $SmCo_5$ Magnets from Core/Shell Co/Sm_2O_3 Nanoparticles.' Advanced Materials volume 19, pp. 3349–3352 (2007).

[3] J. H. N. van Vucht, F. A. Kuijpers and H. C. A. M. Bruning. 'Reversible room-temperature absorption of large quantities of hydrogen by intermetallic compounds.' Philips Res. Rep. volume 25, p. 40 (1970).

[4] P. Villars and K. Cenzual. 'Pearson's Crystal Data: Crystal Structure Database for Inorganic Compounds.' ASM International: Materials Park, Ohio, USA (2016/2017).

[5] A. F. Bialon, T. Hammerschmidt and R. Drautz. 'Three-Parameter Crystal-Structure Prediction for sp-d-Valent Compounds.' Chemistry of Materials volume 28, pp. 2550–2556 (2016).

[6] F. A. Mohammad, S. Yehia and S. H. Aly. 'A first-principle study of the magnetic, electronic and elastic properties of the hypothetical YFe_5 compound.' Physica B: Condensed Matter volume 407, pp. 2486 – 2489 (2012).

[7] Y. Wang, J. Shen, N. X. Chen and J. L. Wang. 'Theoretical investigation on site preference of foreign atoms in rare-earth intermetallics.' Journal of Alloys and Compounds volume 319, pp. 62 – 73 (2001).

[8] F. Maruyama, H. Nagai, Y. Amako et al. 'Magnetic properties of the hypothetical compound YFe_5.' Physica B: Condensed Matter volume 266, pp. 356 – 360 (1999).

[9] A. R. Miedema, P. F. de Châtel and F. R. de Boer. 'Cohesion in alloys — fundamentals of a semi-empirical model.' Physica B+C volume 100, pp. 1–28 (1980).

[10] Q. Guo and O. J. Kleppa. 'The standard enthalpies of formation of the compounds of early transition metals with late transition metals and with noble metals as determined by Kleppa and co-workers at the University of Chicago — A review.' Journal of Alloys and Compounds volume 321, pp. 169–182 (2001).

[11] H. Zhang, S. Shang, J. E. Saal et al. 'Enthalpies of formation of magnesium compounds from first-principles calculations.' Intermetallics volume 17, pp. 878–885 (2009).

[12] B. Zhang and W. A. Jesser. 'Formation energy of ternary alloy systems calculated by an extended Miedema model.' Physica B: Condensed Matter volume 315, pp. 123 – 132 (2002).

[13] P. K. Ray, M. Akinj and M. J. Kramer. 'Applications of an extended Miedema's model for ternary alloys.' Journal of Alloys and Compounds volume 489, pp. 357 – 361 (2010).

[14] A. O. Lyakhov, A. R. Oganov, H. T. Stokes and Q. Zhu. 'New developments in evolutionary structure prediction algorithm USPEX.' Computer Physics Communications volume 184, pp. 1172–1182 (2013).

[15] A. Zunger. 'Systematization of the stable crystal structure of all AB-type binary compounds: A pseudopotential orbital-radii approach.' Phys. Rev. B volume 22, p. 5839 (1980).

[16] P. Villars. 'A three-dimensional structural stability diagram for 998 binary AB intermetallic compounds.' J. Less. Comm. Met. volume 92, pp. 215–238 (1983).

[17] D. Pettifor. 'Bonding and Structure of Intermetallics: A New Bond Order Potential.' Phil. Trans. R. Soc. Lond. A volume 334, pp. 439–449 (1991).

[18] values for precious metals showed an overestimation of the charge transfer, were reduced by 0.2 for group 7-9 and by 0.4 for group 10/11 .

[19] B. Cordero, V. Gomez, A. E. Platero-Prats et al. 'Covalent radii revisited.' Dalton Transactions volume 21, pp. 2832–2838 (2008).

[20] P. Hohenberg and W. Kohn. 'Inhomogeneous electron gas.' Phys. Rev. B volume 136, p. 864 (1964).

[21] W. Kohn and L. J. Sham. 'Self-consistent equations including exchange and correlation effects.' Phys. Rev. A volume 140, p. 1133 (1965).

[22] G. Kresse and J. Furthmüller. 'Efficiency of ab-initio total energy calculations for metals and semiconductors using a plane-wave basis set.' Comput. Mat. Sci. volume 6, p. 15 (1996).

[23] G. Kresse and J. Furthmüller. 'Efficient iterative schemes for ab initio total-energy calculations using a plane-wave basis set.' Phys. Rev. B volume 54, p. 11169 (1996).

[24] P. E. Blöchl. 'Projector augmented-wave method.' Phys. Rev. B volume 50, p. 17953 (1994).

[25] G. Kresse and D. Joubert. 'From ultrasoft pseudopotentials to the projector augmented-wave method.' Phys. Rev. B volume 59, p. 1758 (1999).

[26] J. P. Perdew, K. Burke and M. Ernzerhof. 'Generalized gradient approximation made simple.' Phys. Rev. Lett. volume 77, p. 3865 (1996).

[27] L. Vitos. In 'The EMTO Method and Applications, in Computational Quantum Mechanics for Materials Engineers,' Springer-Verlag (2007).

[28] P. Soven. 'Coherent-Potential Model of Substitutional Disordered Alloys.' Phys. Rev. volume 156, p. 809 (1967).

[29] B. L. Gyorffy. 'Coherent-potential approximation for a nonoverlapping-muffin-tin-potential model of random substitutional alloys.' Phys. Rev. B volume 5, p. 2382 (1972).

[30] P. A. Korzhavyi, A. V. Ruban, I. A. Abrikosov and H. L. Skriver. 'Madelung energy for random metallic alloys in the coherent potential approximation.' Phys. Rev. B volume 51, p. 5773 (1995).

[31] V. L. Moruzzi, J. F. Janak and K. Schwarz. 'Calculated thermal properties of metals.' Phys. Rev. B volume 37, p. 790 (1988).

[32] J. P. Perdew and Y. Wang. 'Pair-distribution function and its coupling-constant average for the spin-polarized electron gas.' Phys. Rev. B volume 45, p. 13244 (1992).

[33] G. Grimvall. In 'Thermophysical properties of materials,' Elsevier (1999).

[34] C. Varvenne, A. Luque, W. G. Nöhring and W. A. Curtin. 'Average-atom interatomic potential for random alloys.' Phys. Rev. B volume 93, p. 104201 (2016).

[35] E. Laube and J. B. Kusma. 'Über einige Y- und Dy-haltige Legierungsphasen.' Monatshefte für Chemie und verwandte Teile anderer Wissenschaften volume 95, pp. 1504–1513 (1964).

[36] M. L. Fornasini. 'Crystal structure of (Ho-, Er-, Tm-, Lu-, Y-)Zn_5 and $ThCd_5$ intermetallic compounds.' Journal of the Less Common Metals volume 25, pp. 329 – 332 (1971).

8

Appendix

In chapter 7, the separation of two phases (stable and unstable) in a 2D plot is demarcated by an ellipse. Stable compounds are preferentially inside the region described by the ellipse and unstable compounds are preferentially outside the region. In this section, a mathematical procedure to determine the best parameters for the ellipse is described. The stable and unstable datapoints can be described by a Boolean function, separating the data into two datasets, where one dataset is assumed to be normally distributed along a line. This dataset D is given in matrix notation

$$\mathbf{D} = \begin{pmatrix} x_1 & x_2 & \cdots & x_i \\ y_1 & y_2 & \cdots & y_i \end{pmatrix}. \tag{8.1}$$

A linear fit can be applied by using a least-squares fitting procedure, yielding a and b in

$$f(x) = ax + b. \tag{8.2}$$

The angle between the fit and the x-axis α is then given by

$$\alpha = \tan^{-1}(a) \tag{8.3}$$

and the intercept of the x-axis is given by

$$x_0 = -\frac{b}{a}. \tag{8.4}$$

The matrix $\mathbf{R}$ rotates the coordinates (x, y) clockwise over the degree α

$$\mathbf{R} = \begin{pmatrix} \cos\alpha & \sin\alpha \\ -\sin\alpha & \cos\alpha \end{pmatrix} \tag{8.5}$$

and the x-intercept that can be used to shift the data to the origin before rotating $\mathbf{s_x} = \begin{pmatrix} x_0 \\ 0 \end{pmatrix} \mathbf{J}$ where $\mathbf{J}$ is a $2 \times i$ matrix consisting of only ones. The dataset can now be rotated by using

$$\mathbf{D_{rot}} = \mathbf{R} \times (\mathbf{D} - \mathbf{s_x}) + \mathbf{s_x} \tag{8.6}$$

around α so that the linear fit is on the x-axis. By calculating the standard deviations along both principal axes σ_x, σ_y and the mean μ, the data can be transformed into a circular symmetric form, around the origin. This is done using matrices $\mathbf{m_y} = \begin{pmatrix} 1 \\ \frac{\sigma_x}{\sigma_y} \end{pmatrix} \mathbf{J}$ and $\mathbf{t_x} = \begin{pmatrix} \mu \\ 0 \end{pmatrix} \mathbf{J}$

$$\mathbf{D_{sym}} = \mathbf{m_y} \circ (\mathbf{D_{rot}} - \mathbf{t_x}). \tag{8.7}$$

By applying this procedure to both datasets, using common transformation matrices, an ellipse can be drawn separating the data of the two datasets. This is easily done after converting $\mathbf{D_{sym}}$ to polar coordinates (r_i, ϕ) and using the criterion $r_i < 2\sigma_x$ and result in 94,4% of datapoints inside the region. The region is then described by a circle that can be transformed back into an ellipse by using the inverse operation

$$\mathbf{e}(t) = \mathbf{R^{-1}} \times \left(\begin{pmatrix} 2\sigma_x \cos(t) \\ 2\sigma_y \sin(t) \end{pmatrix} - \mathbf{s_x} + \mathbf{t_x} \right) + \mathbf{s_x}. \tag{8.8}$$

When the data is not normally distributed or there is no full separation between the two datasets, the values x_0 ($\mathbf{s_x}$), α ($\mathbf{R}$), μ ($\mathbf{s_x}$), σ_x and σ_y can be used as a starting point for a fitting routine. The optimal region can be determined by maximizing the total probability

$$P = \frac{n_e^{in} + n_c^{out}}{n_T}, \tag{8.9}$$

based on the total number of datapoints n_T, the experimentally determined datapoints inside the region n_e^{in} and the calculated datapoints outside the region n_c^{out}.

Periodic table

1 Alkali Metals (IA) | 2 Alkali Earth Metals (IIA) | 3 (IIIB) | 4 (IVB) | 5 (VB) | 6 (VIB) | 7 (VIIB) | 8 (VIIIB) | 9 (VIII) | 10 (VIII) | 11 (IB) | 12 (IIB) | 13 (IIIA) | 14 (IVA) | 15 Pnictides (VA) | 16 Chalcogens (VIA) | 17 Halogens (VIIA) | 18 Noble gases (VIIIA)

paramagnetic
ferromagnetic
antiferromagnetic
at room temperature

mild oxidation | avg oxidation | heavy oxidation
abundant cheap | scarce costly | rare expensive | radioactive

Name		
s	E_Z	MP
p		BP
d	Ox. States	VT
f	Ox. Air	φ*
M	Abundance	$n_{WS}^{1/3}$
CP	Price	EN

Ox. Air = -ΔG° of oxides at 0 K (10² kJ/gr)
Abundance = crust abundance in atomic %
Price per 100 g (june 2013)
MP = melting point in °C
BP = boiling point in °C
VT = temperature in °C to reach a vapor pressure of 1 Pa
φ = work function (V)
$n_{WS}^{1/3}$ = electron density @ boundary of the Wigner-Seitz cell
EN = Pauling electronegativity
M = magnetic moment (μ_B/atom)
CP = Curie/Néel temperature in °C

1	Hydrogen																2	Helium
$1s^1$	H_1	-259° -253°															$1s^2$	He_2 -272° -269°
	±1																	
	3,0%	2.2																
3	Lithium	Beryllium										Boron	Carbon	Nitrogen	Oxygen	Fluorine	Neon	
$2s^1$	Li_3	181° 1342°	$2s^2$	Be_4	1287° 2471°							$2s^2 2p^1$ B_5	2075° 4000°	$2s^2 2p^2$ C_6	4492°t 3642°	$2s^2 2p^3$ N_7	-210° -196°	$2s^2 2p^4$ O_8	-219° -183°	$2s^2 2p^5$ F_9	-259° -253°	$2s^2 2p^6$ Ne_{10}	-249° -246°
	+1	524°		+2	1189°							+3	2075°	+2±4		±1±2±3+4+5		-2		-1			
	11.8	2,85		11.9	5,05							8.37	5,30										
	1,2% E-2	1,50		4,2% E-4	1,67							8,9% E-3	1,75	3,3% E-1		1,2% E-2		57,5%		5,9% E-2			
	€ 78	0.98		€ 636	1.57							€ 748	2.04		2.55		3.04	-238°	3.44		3.98		
11	Sodium	Magnesium										Aluminum	Silicon	Phosphorus	Sulfur	Chlorine	Argon	
$3s^1$	Na_{11}	97,8° 883°	$3s^2$	Mg_{12}	650° 1090°							$3s^2 3p^1$ Al_{13}	660° 2519°	$3s^2 3p^2$ Si_{14}	1414° 3265°	$3s^2 3p^3$ P_{15}	44° 281°	$3s^2 3p^4$ S_{16}	115° 445°	$3s^2 3p^5$ Cl_{17}	-259° -253°	$3s^2 3p^6$ Ar_{18}	-189° -186°
	+1	281°		+2	428°							±1	1208°	+2±4	1635°	±3+5	182°	-2+4+6	102°	±1+5+7			
	8.20	2,70		11.9	3,45							11.1	4,20	9.04	4,70	5.94	5,55	3.64					
	2,0%	0,82		2,4%	1,17							6,1%	1,39	19,2%	1,50	6,5% E-5	1,65	3,9% E-2		2,1% E-2			
	€ 23	0.93		€ 59	1.00							€ 115	1.61	€ 70	1.90	€ 35	2.19	€ 9	2.58		3.16		
19	Potassium	Calcium	Scandium	Titanium	Vanadium	Chromium	Manganese	Iron	Cobalt	Nickel	Copper	Zinc	Gallium	Germanium	Arsenic	Selenium	Bromine	Krypton	
$4s^1$	K_{19}	63,4° 759°	$4s^2$	Ca_{20}	842° 1484°	$4s^2$ Sc_{21}	1541° 2836°	$4s^2$ Ti_{22}	1668° 3407°	$4s^2$ V_{23}	1910° 3407°	$4s^1$ Cr_{24}	1907° 2671°	$4s^2$ Mn_{25}	1246° 2061°	$4s^2$ Fe_{26}	1538° 2861°	$4s^2$ Co_{27}	1495° 2913°	$4s^2$ Ni_{28}	1455° 2913°	$4s^1$ Cu_{29}	1085° 2562°	$4s^2$ Zn_{30}	420° 907°	$4s^2 4p^1$ Ga_{31}	30° 2204°	$4s^2 4p^2$ Ge_{32}	938° 2833°	$4s^2 4p^3$ As_{33}	817°t 614°	$4s^2 4p^4$ Se_{34}	221° 685°	$4s^2 4p^5$ Br_{35}	-259° -253°	$4s^2 4p^6$ Kr_{36}	-157° -153°
	+1	200°		+2	591°	$3d^1$ +3	1372°	$3d^2$ +2+3+4	1709°	$3d^3$ +2+3+4+5	1828°	$3d^5$ +2+3+6	1383°	$3d^5$ +2+3+4+7	955°	$3d^6$ +2+3	1455°	$3d^7$ +2+3	1517°	$3d^8$ +2+3	1510°	$3d^{10}$ +1+2	1236°	$3d^{10}$ +2	337°	$3d^{10}$ ±1	1037°	$3d^{10}$ +2+4	1371°	$3d^{10}$ ±3+5	280°	$3d^{10}$ -2+4+6	227°	$3d^{10}$ ±1+5		$3d^{10}$	
	7.20	2,25		12.8	2,55	12.8	3,25	10.3	3,80	8.28	4,25	7.45	4,65	7.70	4,45	5.94	4,93	4.73	5,10	4.77	5,20	3.34	4,45	7.03	4,10	7.20	4,10	5.40	4,55	4.39	4,80	2.21					
	7,8% E-1	0,65		2,5%	0,91	6,2% E-4	1,27	2,8% E-1	1,52	4,2% E-3	1,64	0,4 μ 2,8% E-3	1,73	4,0% E-2	1,61	2,2 μ 2,3%	1,77	1,7 μ 5,1% E-4	1,75	0,6 μ 1,2% E-3	1,75	8,5% E-4	1,47	2,3% E-3	1,32	5,3% E-4	1,31	3,6% E-5	1,37	1,5% E-4	1,44	2,3% E-6		4,0% E-5			
	€ 235	0.82		€ 29	0.95	€ 16500	1.36	€ 73	1.54	€ 360	1.63	39° € 49	1.66	€ 76	1.55	770° € 13	1.83	1117° € 105	1.88	356° € 49	1.91	€ 61	1.90	€ 15	1.65	€ 291	1.81	€ 1250	2.01	€ 260	2.18	€ 130	2.55		2.96		
37	Rubidium	Strontium	Yttrium	Zirconium	Niobium	Molybdenum	Technetium	Ruthenium	Rhodium	Palladium	Silver	Cadmium	Indium	Tin	Antimony	Tellurium	Iodine	Xenon	
$5s^1$	Rb_{37}	39,3° 688°	$5s^2$	Sr_{38}	777° 1382°	$5s^2$ Y_{39}	1522° 3345°	$5s^2$ Zr_{40}	1855° 4409°	$5s^1$ Nb_{41}	2477° 4744°	$5s^1$ Mo_{42}	2623° 4639°	$5s^2$ Tc_{43}	2157° 4265°	$5s^1$ Ru_{44}	2334° 4150°	$5s^1$ Rh_{45}	1964° 3695°	$4d^{10}$ Pd_{46}	1555° 2963°	$5s^1$ Ag_{47}	962° 2162°	$5s^2$ Cd_{48}	321° 767°	$5s^2 5p^1$ In_{49}	157° 2072°	$5s^2 5p^2$ Sn_{50}	232° 2602°	$5s^2 5p^3$ Sb_{51}	631° 1587°	$5s^2 5p^4$ Te_{52}	450° 988°	$5s^2 5p^5$ I_{53}	-259° -253°	$5s^2 5p^6$ Xe_{54}	-112° -108°
	+1	160		+2	523°	$4d^1$ +3	1610°	$4d^2$ +4	2366°	$4d^4$ +3+5	2669°	$4d^5$ +6	2469°	$4d^5$ +4+6+7		$4d^7$ +3	2315°	$4d^8$ +3	2015°	$4d^{10}$ +2+4	1448°	$4d^{10}$ +1	1010°	$4d^{10}$ +2	257°	$4d^{10}$ ±1	923°	$4d^{10}$ +2+4	1224°	$4d^{10}$ ±3+5	534°	$4d^{10}$ -2+4+6		$4d^{10}$ ±1+5+7		$4d^{10}$	
	6.61	2,10		11.8	2,40	12.7	3,20	11.0	3,45	8.03	4,05	5.02	4,65				5,40	1.76	5,40		5,45	0.544	4,35	5.23	4,05	6.19	3,90	5.77	4,15	4.64	4,40	3.22					
	2,2% E-3	0,60		7,3% E-3	0,84	2,6% E-4	1,21	4,2% E-3	1,41	2,6% E-4	1,64	1,3% E-5	1,77			6,7% E-9	1,76	1,4% E-8	1,76	9,8% E-9	1,67	9,8% E-7	1,36	1,1% E-6	1,24	1.2% E-6	1,17	3,7% E-5	1,24	1,2% E-5	1,26	4,2% E-7		7,7% E-6			
	€ 1900	0.82		€ 417	0.95	€ 238	1.22	€ 211	1.33	€ 95	1.6	€ 56	2.16		1.9	€ 2570	2.2	€ 87350	2.28	€ 6948	2.20	€ 610	1.93	€ 57	1.69	€ 1600	1.78	€ 31	1.96	€ 44	2.05	€ 458	2.1		2.66		
55	Cesium	Barium	Lanthanum	Hafnium	Tantalum	Tungsten	Rhenium	Osmium	Iridium	Platinum	Gold	Mercury	Thallium	Lead	Bismuth	Polonium	Astatine	Radon	
$6s^1$	Cs_{55}	28,4° 671°	$6s^2$	Ba_{56}	727° 1897°	$6s^2$ La_{57}	918° 3464°	$6s^2$ Hf_{72}	2233° 4603°	$6s^2$ Ta_{73}	3017° 5458°	$6s^2$ W_{74}	3422° 5555°	$6s^2$ Re_{75}	3186° 5596°	$6s^2$ Os_{76}	3033° 5012°	$6s^2$ Ir_{77}	2446° 4428°	$6s^1$ Pt_{78}	1768° 3825°	$6s^1$ Au_{79}	1064° 2856°	$6s^2$ Hg_{80}	-39° 357°	$6s^2 6p^1$ Tl_{81}	304° 1473°	$6s^2 6p^2$ Pb_{82}	327° 1749°	$6s^2 6p^3$ Bi_{83}	271° 1564°	$6s^2 6p^4$ Po_{84}	254° 962°	$6s^2 6p^5$ At_{85}	-259° -253°	$6s^2 6p^6$ Rn_{86}	-71° -62°
	+1	145°		+2	638°	$5d^1$ +3	1732°	$5d^2$ +4	2416°	$5d^3$ +5	3024°	$5d^4$ +6	3204°	$5d^5$ +4+6+7	3030°	$5d^6$ +3+4	2887°	$5d^7$ +3+4	2440°	$5d^9$ +2+4	2057°	$5d^{10}$ +1+3	1373°	$5d^{10}$ +1+2	42°	$5d^{10}$ ±1	609°	$5d^{10}$ +2+4	705°	$5d^{10}$ +3+5	668°	$5d^{10}$ +2+4		$5d^{10}$		$5d^{10}$	
	6.40	1,95		11.1	2,32	11.9	3,17	11.1	3,60	8.16	4,05	5.56	4,80		5,20	2.59	5,40	1.80	5,55	1.34	5,65		5.15	1.80	4,20	2.84	3,90	4.31	4,10	4.39	4,15					
	7,4% E-5	0,55		9,1% E-3	0,81	4,5% E-4	1,18	5,9% E-5	1,45	1,0% E-5	1,63	1,5% E-5	1,81	2,1% E-9	1,85	3,3% E-10	1,85	2,3% E-10	1,83	5,1% E-9	1,78	1.5% E-8	1,57	5,5% E-7	1,24	5,4% E-6	1,12	1,6% E-4	1,15	2,2% E-6	1,16					
	€ 1970	0.72		€ 382	0.89	€ 334	1.1	€ 382	1.3	€ 290	1.5	€ 43	2.36	€ 2830	1.9	€ 12300	2.2	€ 9900	2.20	€ 15910	2.28	€ 13600	2.54	€ 24	2.00	€ 590	1.62	€ 14	2.33	€ 44	2.02		2.0		2.2		
87	Francium	Radium	Actinium	Rutherfordium	Dubnium	Seaborgium	Bohrium	Hassium	Meitnerium	Darmstadtium	Röntgium	Copernicium	Nihonium	Flerovium	Moscovium	Livermorium	Tennesine	Oganesson	
$7s^1$	Fr_{87}	27°	$7s^2$	Ra_{88}	700°	$7s^2$ Ac_{89}	1051° 3198°	Rf_{104}		Db_{105}		Sg_{106}		Bh_{107}		Hs_{108}		Mt_{109}		Ds_{110}		Rg_{111}		Cn_{112}		Nh_{113}		Fl_{114}		Mc_{115}		Lv_{116}		Ts_{117}		Og_{118}	
	+1			+2		$6d^1$ +3																													
		0.7			0.9		1.1																												

Lanthanides

57	Cerium	Praseodymium	Neodymium	Promethium	Samarium	Europium	Gadolinium	Terbium	Dysprosium	Holmium	Erbium	Thulium	Ytterbium	Lutetium
$6s^2$	Ce_{58} 798° 3443°	$6s^2$ Pr_{59} 931° 3520°	$6s^2$ Nd_{60} 1021° 3074°	$6s^2$ Pm_{61} 1042° 3000°	$6s^2$ Sm_{62} 1074° 1794°	$6s^2$ Eu_{63} 822° 1596°	$6s^2$ Gd_{64} 1313° 3273°	$6s^2$ Tb_{65} 1356° 3230°	$6s^2$ Dy_{66} 1412° 2567°	$6s^2$ Ho_{67} 1474° 2868°	$6s^2$ Er_{68} 1529° 2868°	$6s^2$ Tm_{69} 1545° 1950°	$6s^2$ Yb_{70} 819° 1196°	$6s^2$ Lu_{71} 1663° 3402°
$5d^1$	+3+4 1719°	+3 1498°	+3 1322°	+3	+2+3 728°	+2+3 590°	$5d^1$ +3 1563°	+3 1516°	+3 1105°	+3 1159°	+3 1231°	+3 844°	+2+3 463°	$5d^1$ +3 1633°
$4f^1$	11.9 3,18	$4f^3$ 12.1 3,19	$4f^4$ 3,19	$4f^5$ 1,13	$4f^6$ 12.0 3,20	$4f^7$ 12.1 2,50	$4f^7$ 12.0 3,20	$4f^9$ 12.3 3,20	$4f^{10}$ 11.7 3,21	$4f^{11}$ 12.5 3,22	$4f^{12}$ 10.9 3,22	$4f^{13}$ 12.5 3,22	$4f^{14}$ 12.0 2,90	$4f^{14}$ 12.5 3,22
0,6 μ	9,0% E-4 1,19	1,0% E-4 1,20	3,6 μ 3,7% E-4 1,20		0,5 μ 6,3% E-5 1,21	5,9 μ 1,3% E-5 0,88	8,0 μ 5,1% E-5 1,21	9,8 μ 8,8% E-6 1,22	11 μ 4,8% E-5 1,22	11 μ 1,0% E-5 1,22	9,9 μ 2,8% E-5 1,23	7,6 μ 4,4% E-6 1,23	2,7% E-5 1,10	4,1% E-6 1,24
-260°	€ 1320 1.12	€ 1170 1.13	-254° € 1044 1.14	1.13	-168° € 906 1.17	-183° € 10700 1.2	19° € 1134 1.2	-44° € 7040 1.1	-94° € 1272 1.22	-141° € 1206 1.23	-188° € 1048 1.24	-217° € 10300 1.25	€ 2584 1.1	€ 22400 1.27

Actinides

89	Thorium	Protactinium	Uranium	Neptunium	Plutonium	Americium	Curium	Berkelium	Californium	Einsteinium	Fermium	Mendelevium	Nobelium	Lawrencium
$7s^2$	Th_{90} 1750° 4788°	$7s^2$ Pa_{91} 1572°	$7s^2$ U_{92} 1135° 4131°	$7s^2$ Np_{93} 644°	$7s^2$ Pu_{94} 640° 3228°	$7s^2$ Am_{95} 1176° 2011°	$7s^2$ Cm_{96} 1345°	$7s^2$ Bk_{97} 1050°	$7s^2$ Cf_{98} 900°	$7s^2$ Es_{99} 860°	$7s^2$ Fm_{100} 1527°	$7s^2$ Md_{101} 827°	$7s^2$ No_{102} 827°	$7s^2 7p^1$ Lr_{103} 1627°
$6d^2$	+4	$6d^1$ +4+5	$6d^1$ +3+4+5+6	$6d^1$ +3+4+5+6	+3+4+5+6	+3+4+5+6	$6d^1$ +3	+3+4	+3	+3	+3	+2+3	+2+3	+3
$5f^1$	12.2	$5f^2$	$5f^3$ 10.8	$5f^4$	$5f^6$ 10.8	$5f^7$	$5f^7$	$5f^9$	$5f^{10}$	$5f^{11}$	$5f^{12}$	$5f^{13}$	$5f^{14}$	$5f^{14}$
	9,1% E-5 1.3	1.5	2.2% E-5 1.38	1.36	1.28									

Summary

In this thesis, the boundary conditions for the development of giant magnetocaloric materials are investigated. The magnetocaloric effect is found in magnetic materials, when they are subjected to an external magnetic field. This leads to abrupt magnetization changes that cause a temperature change in the material. Materials based on Fe_2P show giant temperature changes around room temperature and are especially suited for cooling applications. This is due to the large magnetization change that can be realized with the application of a relatively small magnetic field around the ferro- to paramagnetic phase transition. This transition is of a first order, giving rise to latent heat and rise to "giant" effects.

After earlier studies investigated the relation between microscopic and macroscopic properties of these materials, the focus of this thesis is on the electronic factors that play a role in the stability and phase transitions of these compounds. After all, when the mechanism behind these phase transitions is clear, is it easier to search for new materials that show similar phase transitions. Two strategies are possible: elucidating the mechanism of Fe_2P-based materials or investigating materials that show similar phase transitions. The latter is described in the next paragraph.

The first investigated material is Mn_3Ga, described in chapter 4. A literature study shows that manganese (Mn) possesses a large magnetic moment and the material shows a phase transition around room temperature. Both properties are essential for good magnetocaloric materials. Mn_3Ga crystallizes in a Mg_3Cd-type crystal structure, where the magnetic atoms are arranged in a triangular configuration. The crystal structure is of major importance for the magnetocaloric properties, because the triangular coordination of the magnetic atoms affect the magnetic properties. The phase transition is investigated using two different techniques that can determine the crystal symmetry. X-ray diffraction yields information about the electrons of the atoms, while neutron diffraction yields information about the nuclei and the magnetic properties. By applying X-ray diffraction as a function of temperature, a change in the crystal structure was observed. This is caused by a deformation of the triangular arrangement of the magnetic atoms. By applying neutron diffraction at different temperatures, the changing magnetic structure is also detected. Above room temperature, the magnetic moments of Mn are arranged in such a way that they yield no net magnetization. Below room temperature the magnetic moments rotate, giving rise to a net magnetization. At the same time, the hexagonal symmetry is lifted. Despite the fact that the material shows a magnetoelastic transition around room temperature, the relatively low net magnetization and the second-order phase transition exclude this material as being a candidate for cooling applications.

The second material, covered in chapters 5 and 6, is based on Fe_2P. This material crystallizes in layers that have alternating magnetic properties. This is due to the different coordination that the magnetic atoms have with their neighboring atoms. Earlier electronic calculations indicate that the magnetic properties of the atoms in one layer change in the paramagnetic state, while the properties of the atoms in the other layer hardly change when the material crosses the phase transition. At the same time, the distances between the magnetic and non-magnetic atoms change, causing a deformation in the unit cell but hardly affecting the volume. Because the magnetic properties are difficult to measure in the paramagnetic state, the electronic properties were measured, due to the coupling with the magnetic properties. This can give information about the occupation (and orientation) of atomic orbitals. X-ray absorption experiments can measure the energy of these orbitals in the ferro- and paramagnetic state. From these experiments is it clear that the energies of these occupied orbitals do not significantly change and no valence change takes place. By measuring the electron density in the ferro- and paramagnetic state using X-ray diffraction, a different orientation of the orbitals is detected. The redistribution of the electron density shows a large resemblance with the electron density obtained from calculations and is detected for materials having different compositions of FeMn(P,Si,B). This shows that this redistribution is present in materials with different compositions showing different magnetic behavior.

X-ray diffraction experiments also yield information about the interatomic distances. Given the symmetry in this material, the magnetic atoms have a degree of freedom that the non-magnetic atoms lack. By mapping this behavior, the magnetic atoms in one layer show relatively constant interatomic distances across the transition. This is in indication that the bonds between these atoms are constant. The magnetic atoms in the other layer, showing the redistribution of electron density, show a difference in interatomic distances. The interesting fact about these atom pairs is that they are composed of a magnetic and metalloid atom, like Si, Ge and As. These elements are frequently present in giant magnetocaloric materials, because their bond strengths can vary. This is often the cause of the phase transition. For this material, the redistribution of electron density causes a strengthening of the bond in the paramagnetic phase, at the expense of the magnetic moment. This is shown by studying both the electron density and the interatomic distances.

The study of the underlying mechanism of giant magnetocaloric materials shows that materials with different coordination number of magnetic atoms can lead to functional behavior. Materials that crystallize in the $CaCu_5$-type crystal structure show the same versatility in coordination numbers and are potentially interesting. $Y(Fe,Si)_5$ has a high concentration of magnetic atoms that can lead to large magnetization changes and contain the metalloid silicon. However interesting this material may be, when synthesized it decomposes into two other compounds and no single phase was obtained. By using a crystallographic database, it is possible to map all compositions that are stable. When all unstable binary compositions are added, the difference between these two groups can be investigated. By plotting the electronic properties of the elements, it is possible to observe a separation between these two groups. These properties are based on the electron density and the work function. The plots show that YFe_5 can only be stabilized by replacing the majority of Fe. Adding metalloid elements should increase the stability, but in practice this approach is limited for metalloid elements.

In the quest for new functional materials to use in a magnetic refrigeration cycle, it is important to know the electronic properties of the materials. By predicting these properties, new candidate systems can be found, but hypothetical compounds can only be useful when they are formed experimentally. When the electronic properties and the phase stability are known, large leaps in material science can be achieved.

Samenvatting

In dit proefschrift worden de randvoorwaarden onderzocht voor de ontwikkeling van materialen die een groot magnetocalorisch effect vertonen. Dit effect vindt plaats bij magnetische materialen wanneer zij onderworpen worden aan een extern magneetveld. Dit leidt tot instantane veranderingen in de magnetisatie waardoor er een temperatuursverandering optreedt in het materiaal. Materialen die gebaseerd zijn op Fe_2P laten grote temperatuursveranderingen zien rond kamertemperatuur en zijn uitermate geschikt om gebruikt te worden voor koeltoepassingen. Dit komt door de grote magnetisatieverandering die gerealiseerd kan worden met een relatief klein magnetisch veld rond de overgangstemperatuur tussen de ferro- en paramagnetische toestand, welke rond kamertemperatuur ligt. Deze faseovergang is van een eerste orde, waarbij latente warmte vrijkomt. Dit geeft aanleiding tot "reuze" effecten.

Nadat eerdere onderzoeken het verband tussen microscopische en macroscopische eigenschappen van deze materialen hebben onderzocht, ligt de nadruk bij dit proefschrift meer op de onderliggende elektronische invloeden die een rol spelen bij de stabiliteit en faseovergangen van deze verbindingen. Immers, wanneer het mechanisme achter deze faseovergang duidelijk is, is het ook makkelijker om geschikte nieuwe materialen te vinden. Hierbij zijn twee strategieën mogelijk: het ophelderen van het mechanisme van Fe_2P-gebaseerde materialen of te zoeken naar materialen die soortgelijke faseovergangen vertonen. De laatste strategie is beschreven in de volgende paragraaf.

Het eerste onderzochte materiaal is Mn_3Ga, beschreven in hoofdstuk 4. Een literatuurstudie laat zien dat mangaan (Mn) een groot magnetisch moment heeft en het materiaal een faseovergang laat zien rond kamertemperatuur. Beide eigenschappen zijn essentieel voor goede magnetocalorische materialen. Mn_3Ga kristalliseert in een Mg_3Cd-type kristalstructuur, waarbij de magnetische atomen in een driehoek zijn gerangschikt. De kristalstructuur is van groot belang bij de magnetische eigenschappen, omdat de driehoekige coördinatie van magnetische atomen met buuratomen de magnetische eigenschappen beïnvloeden. De faseovergang is onderzocht met twee verschillende technieken die de kristalsymmetrie kunnen bepalen. Röntgendiffractie geeft informatie over de elektronen van de atomen, neutronendiffractie geeft informatie over de kernen en magnetische eigenschappen. Door röntgendiffractie toe te passen als functie van temperatuur, is een verandering in de kristalstructuur te zien. Dit wordt veroorzaakt door een vervorming van de driehoekige configuratie van de magnetische atomen. Door neutronendiffractie toe te passen op verschillende temperaturen is ook de veranderende magnetische structuur te zien. Boven kamertemperatuur liggen de magnetische momenten van Mn zo, dat er geen netto magnetisatie is, er is sprake van een antiferromagneet. Beneden kamertemperatuur draait het magnetisch moment van een van de atomen waardoor er

een netto magnetisatie optreedt. Tegelijkertijd wordt de hexagonale symmetrie opgeheven. Ondanks dat het materiaal een magnetoelastisch effect laat zien rond kamertemperatuur, zorgen de relatief lage netto magnetisatie en de tweede orde faseovergang ervoor dat dit materiaal geen goede kandidaat is voor koeltoepassingen.

Het tweede materiaal, beschreven in hoofdstukken 5 en 6, is gebaseerd op Fe_2P. Dit materiaal kristalliseert in lagen die alternerend verschillende magnetische eigenschappen hebben. Dit komt door de verschillende coördinatie van de magnetische atomen met buuratomen. Elektronische berekeningen die eerder zijn gedaan, laten zien dat de magnetische eigenschappen van deze atomen in één laag veranderen in de paramagnetische toestand, terwijl de eigenschappen van de atomen in de andere laag amper veranderen als het materiaal ferromagnetisch wordt. Tegelijkertijd veranderen de afstanden tussen magnetische en niet-magnetische atomen, waardoor de eenheidscel vervormt, terwijl het volume nagenoeg gelijk blijft.

Omdat de magnetische eigenschappen in de paramagnetische toestand moeilijk te meten zijn, zijn de elektronische eigenschappen gemeten. De berekeningen laten zien dat deze twee eigenschappen aan elkaar gekoppeld zijn en dat dit samenhangt met de bezetting (en oriëntatie) van de atomaire orbitalen. Röntgenabsorptie experimenten kunnen de energie van deze orbitalen meten in de ferro- en paramagnetische toestand. Uit deze experimenten blijkt dat de energieën van de bezette orbitalen niet significant veranderen en dat er geen valentieverandering plaatsvindt. Door de elektronendichtheid te meten in de ferro- en paramagnetische toestanden met behulp van röntgendiffractie, is er wel een verschil in oriëntatie van de orbitalen te zien. De herverdeling van de elektronendichtheid toont grote gelijkenis met de berekende dichtheid. Dit is aangetoond voor materialen met verschillende composities, bestaande uit FeMn(P,Si,B). Dit laat zien dat deze herverdeling aanwezig is in materialen met verschillende composities die verschillend magnetisch gedrag vertonen.

Röntgendiffractie experimenten geven ook informatie over de onderlinge afstand tussen de atomen. Gegeven de aanwezige symmetrie in dit materiaal, hebben de magnetische atomen een vrijheidsgraad die de niet-magnetische atomen niet hebben. Door dit gedrag in kaart te brengen, is te zien dat de magnetische atomen in de ene laag stabiele interatomaire afstanden hebben rond de overgang. Dit is een indicatie dat de binding tussen deze atomen niet verandert. De magnetische atomen in de andere laag, waar de herverdeling van de elektronendichtheid optreedt, laat een verschil in interatomaire afstanden zien. Het interessante is dat de atoomparen bestaan uit een magnetisch atoom en een metalloïde atoom, zoals Si, Ge en As. Deze elementen zijn veel voorkomend bij magnetocalorische materialen die reuze effecten laten zien, omdat de bindingen die ze vormen kunnen variëren in sterkte. Dit is vaak de oorzaak van de faseovergang. Bij dit materiaal zorgt de herverdeling van de elektronendichtheid voor een versterking van de binding in de paramagnetische fase, ten koste van het magnetische moment. Zowel de studie naar de elektronendichtheid als de inspectie van de bindingsafstanden duiden dit aan.

Het onderzoek naar het achterliggende mechanisme van reuze magnetocalorische materialen, laat zien dat materialen met verschillende coördinaties rond magnetische atomen tot functioneel gedrag kan leiden. Materialen die kristalliseren in de $CaCu_5$ kristalstructuur laten dezelfde verscheidenheid aan coördinatiegetallen zien en kunnen potentieel interessant zijn. $Y(Fe,Si)_5$ heeft een hoge concentratie aan magnetische atomen, wat kan leiden tot een grote magnetisatieverandering en bevat bovendien het metalloïde silicium. Hoe interessant dit materiaal ook is, wanneer het gemaakt wordt zijn twee andere kristalstructuren stabieler en is het niet mogelijk om dit materiaal in de juiste fase te produceren. Door gebruik te maken van een kristallografische database is het mogelijk om alle composities in kaart te brengen die wel deze kristalstructuur vormen. Als hier nu alle binaire composities aan toe worden gevoegd die niet stabiel zijn, is het verschil is tussen deze twee groepen te zien. Door figuren te maken waarbij twee elektronische eigenschappen van de elementen gebruikt worden, is een scheiding van deze twee groepen te zien. Deze eigenschappen zijn gebaseerd op de elektronendichtheid en de werkfunctie. Deze plots laten zien dat YFe_5 alleen maar gestabiliseerd kan worden als het meeste ijzer wordt vervangen. Het toevoegen van metalloïde elementen lijkt de stabiliteit van de fase op papier wel te bevorderen, maar in de praktijk blijkt dat deze aanpak maar beperkt toepasbaar is voor metalloïde elementen.

In de zoektocht naar nieuwe functionele materialen om te gebruiken in magnetische koelcycli, is het belangrijk om de electronische eigenschappen van materialen te kennen. Door deze te voorspellen kunnen nieuwe modelsystemen gevonden worden, maar hypothetische materialen kunnen alleen maar nuttig zijn wanneer ze in de praktijk ook stabiel zijn. Alleen wanneer de elektronische eigenschappen en de fasestabiliteit bekend zijn, kunnen grote stappen gemaakt worden in materiaalonderzoek.

Acknowledgements

In this chapter I would like to thank all the people why supported me during my time in Delft. Because of the personal nature of these messages, it is appropriate to read them in Dutch when it concerns Dutch speaking people.

Allereerst wil ik Ekkes Brück bedanken voor zijn begeleiding tijdens mijn promotietraject. Men zegt dat je leert van je fouten, en ik heb veel geleerd tijdens deze vier jaar. Vaak heb je me op deze fouten gewezen en kreeg ik de kans om te verbeteren. Dit proces werd bevorderd door de directe manier van communiceren, die ik als prettig heb ervaren. Ik vond het mooi om te zien hoe iemand die enorme passie heeft voor zijn werk, ook tijd kan nemen voor andere zaken die belangrijk zijn in het leven. Ook ben ik erg dankbaar dat ik vaak de vrije hand kreeg om mijn onderzoek zelf in te richten.

Verder wil ik Niels van Dijk bedanken, je vormt samen met Ekkes een goed team. Vooral je oog voor details en sterke theoretische achtergrond heeft me veel geholpen. Ik ben onder de indruk van je kwaliteiten in het schrijven van onderzoeksvoorstellen en je tomeloze inzet als het gaat om het verbeteren van artikelen. Verder heb ik gemerkt dat je je goed kan inleven in promovendi, dit zorgt voor een prettige werksfeer.
Dan wil ik graag Bert Zwart bedanken. Ja Bert, je staat op de derde plaats in deze lijst. Zonder je expertise op het gebied van glas, en vooral kwartsglas, hadden wij geen samples, geen resultaten en geen artikelen. Je positieve instelling is voor iedereen zichtbaar en het is leuk om de verhalen over je verre reizen te horen. Ik wil Rob Boom, Frank de Boer, Rob de Groot en Gilles de Wijs bedanken voor de interessante discussies. Rob de Groot, je brengt de beste facetten van de scheikunde en natuurkunde bij elkaar en ik hoop dat ik dit ook heb kunnen doen in dit proefschrift.

Ik wil de wetenschappelijke staf uit Delft bedanken voor de zeer prettige samenwerking, vooral Stefan Eijt en Erik Kelder. Ook wil ik de ondersteunende staf bedanken. Kees Goubitz heeft altijd interesse getoond in mijn onderzoek en het was goed om met je van gedachten te wisselen. Ik wil Ben Harrison bedanken. Je hebt me veel geholpen bij de voorbereiding en de elektronica van de boogsmelt oven. Ook ben ik dank verschuldigd aan alle mensen van DEMO, onder andere aan René Gommers die me geholpen heeft bij het ontwerp van de smeltkroes. In het bijzonder wil ik Rien Waaijer bedanken, ondanks je hoge werkdruk was je altijd bereid helpen. Verder wil ik Jouke Heringa bedanken voor zijn hulp op het gebied van ICT. Ik denk dat veel mensen je expertise op dit gebied onderschatten. Ook de secretaresses en Anton zijn een grote drijvende kracht die het onderzoek mogelijk maken. Ik wil Nicole, Trudy en vooral Ilse van harte bedanken voor de mooie tijd.

Ook FOM wil ik van harte bedanken voor het financieren van dit onderzoek. Dit instituut staat al jarenlang goed aangeschreven en ik ben nog altijd onder de indruk hoeveel ze in hun medewerkers investeren. In de toekomst zal ik nog lang profijt hebben van mijn opleiding en netwerk.

Now I would like to thank all my fellow PhD students. Dear Xue-Fei, your inquisitive and adaptive nature will get you anywhere you want. I'm sure you'll get there with Fengjiao, who has shown a lot of perseverance during her PhD. Dear Thang, we shared our PhD together, starting on the same day. I hope your life will be as colorful as the pictures you take. Dear Yibole, you were nice to work with, I hope that you and François can stay together for a long time. Dear Swapna, you now have a long term perspective in Delft and I am sure that you'll continue to be an indispensable asset to the battery group. I hope that you'll soon teach some courses in Dutch. Dear Prasenjit, we had a nice cooperation together and it was fruitful for both of us. Although I must admit, sometimes I would have rather have had your job. Dear Bowei, I enjoyed your company and got to know you as an enterprising and open person. I would like to thank all other collegues: Jaiwei, Dimitris, Michael, Xinmin, Casper, Zhou Zhou, Haixing and Lian.

During my PhD, I got to work with some wonderful people. Dipanjan Banerjee, Dmitry Chernyshow and Philip Pattison kindly helped with all the experiments performed at the ESRF. I had good discussions with Denis Bykov from the NERA group. Alexander Barcza was so kind to provide samples that will be part of a new study, not included in this thesis. Erna Delczeg helped with DFT calculations and was very supportive for my work. It was truly a pleasure to work with you.

The TU Delft is a nice place, and it is run by the scientists, at least in the view of many (PhD) students. But in fact, a lot of other people help shape policy and make sure we have buildings to work in. The works council (OdC) checks to see if the decisions that are being made are for the good of the university and the employees and I am proud to have helped them as a member. It is in the OdC where the most involved people are found and it was nice to work with them.

To finish this chapter, I would like to thank all the metaphorical shoulders that I stand on. First of all, my parents, who have always supported me morally. They have truly been a driving force in my career. I would like to thank all my teachers, from the brave teacher in the 5^{th} grade who first showed me some chemistry, to middle school where I was taught about electrons and finally to university where I was taught about the solid state.
I would like to conclude with the most important person in my life, my wife, Eline. You have also taught me a lot about people and you are the best person I can imagine. When I think about you, a quote from Linus Pauling always comes to mind: "Do unto others 25% more than they do unto you, to correct for subjective error". You have supported me during my PhD and I hope we will support each other for many years to come.

Curriculum Vitæ

Maurits Boeije

Maurits was born on 23 Jan. 1987 in Oostburg. He attended the Gaspar van der Heijdenschool in Axel. Later he went to the Reynaertcollege in Hulst, where he graduated from VWO in 2006. After a brief attempt to be enlisted in the navy, he moved to Nijmegen to study chemistry. He finished his bachelor degree in 2010 and continued his master degree at the department of Solid State Chemistry, where he used computational methods to characterize and predict crystal structures of amino acids.

His interests in computer science is reflected in the fact that he ran a computer store during the weekends in Axel. Not only did he enjoy learning, he also enjoys teaching and was a part-time math teacher at Helicon in Velp. After his master project, he focused on industry and did an internship at Océ in Venlo, where he studied crystallization behavior of hot melt ink. In 2013 he started his PhD in physics at the Reactor Institute Delft under supervision of Niels van Dijk and Ekkes Brück, where he was able to use his knowledge on crystal structure determination and modeling to successfully finish within 4 years.

His approach to doing science is to boldly go where no man has gone before, to find new materials or properties of materials. In his thesis, he combined this with his love for teaching, by including a theoretical chapter.
In his free time, he enjoys to practice budo, the Japanese martial arts. He started with Judo at the age of 6 and got his ikkyu degree at the age of 16. He later started iaido, the way of drawing the sword. In 2012 he got his ikkyu degree in iaido and two years later acquired the shodan (black belt) degree when training at Kendo Kai Den Haag under the supervision of Aad van de Wijngaart sensei. In 2017 he got the nidan (2nd dan) degree.

List of Publications

7. X. You, M.F.J. Boeije, A. Barcza, N.H. van Dijk and E. Brück, A crystallographic study on the softening of the first-order phase transition in MnFe(P,Si,B), in preparation.

6. M. Maschek, M.F.J. Boeije, A. Barcza, N.H. van Dijk and E. Brück, Electronic redistribution in magnetocaloric La(Fe,Co,Si)$_{13}$-based compounds, in preparation.

5. M.F.J. Boeije, E.K. Delczeg-Czirjak, N.H. van Dijk, O. Eriksson and E. Brück, On the phase stability of $CaCu_5$-type compounds, J. Alloys. Compd. accepted.

4. M.F.J. Boeije, L. van Eijck, N.H. van Dijk and E. Brück, Structural and magnetic properties of hexagonal (Mn,Fe)$_{3-\delta}$Ga, J. Magn. Magn. Mater. 433, 297-302 (2017).

3. M.F.J. Boeije, M. Maschek, X.F. Miao, N.V. Thang, N.H. van Dijk and E. Brück, Mixed magnetism in magnetocaloric materials with first-order and second-order magnetoelastic transitions, J. Phys. D: Appl. Phys. 50, 174002 (2017).

2. M.F.J. Boeije, P. Roy, F. Guillou, H. Yibole, X.F. Miao, L. Caron, D. Banerjee, N.H. van Dijk, R.A. de Groot and E. Brück, Efficient Room-Temperature Cooling with Magnets, Chem. Mater. 28, 4901-4905 (2016).

1. G.K. Tirumalasetty, C.M. Fang, J. Jansen, T. Yokosawa, M.F.J. Boeije, J. Sietsma, M.A. van Huis and H.W. Zandbergen, Structural tale of two novel (Cr,Mn)C carbides in steel, Acta Materialia 78, 161-172 (2014).